

Ferrofluid enabled micro actuators for endoscopic bio-imaging and analysis

by

Sayed Mohammad Hashem Jayhooni

B.Sc., Shiraz University, Iran, 2010

M.A.Sc., Shiraz University, Iran, 2013

A THESIS SUBMITTED IN PARTIAL FULFILLMENT OF
THE REQUIREMENTS FOR THE DEGREE OF

DOCTOR OF PHILOSOPHY

in

THE FACULTY OF GRADUATE AND POSTDOCTORAL STUDIES
(Biomedical Engineering)

THE UNIVERSITY OF BRITISH COLUMBIA
(Vancouver)

March 2020

© Sayed Mohammad Hashem Jayhooni, 2020

The following individuals certify that they have read, and recommend to the Faculty of Graduate and Postdoctoral Studies for acceptance, the dissertation entitled:

Ferrofluid enabled micro actuators for endoscopic bio-imaging and analysis

submitted by Sayed Mohammad Hashem Jayhooni in partial fulfillment of the
requirements for the
degree of Doctor of Philosophy
in Biomedical Engineering

Examining committee:

Kenichi Takahata, Professor, Electrical and Computer Engineering, UBC

Supervisor

Edmond Cretu, Professor, Electrical and Computer Engineering, UBC

Supervisory Committee Member

Haishan Zeng, Professor, Dermatology and Skin Science, UBC

Supervisory Committee Member

Mu Chiao, Professor, Mechanical Engineering, UBC

University Examiner

Ryozo Nagamune, Associate Professor, Mechanical Engineering, UBC

University Examiner

Abstract

The range of potential applications that micro rotary motors offer is extremely wide and one of the promising categories of applications is for medical devices. Along this direction, micro motors are being used for endoscopic applications to perform a full 360° circumferential scan in order to detect cancer located at the inner surface of the internal organs of humans. Flexibility and maneuverability are two of the most important mechanical characteristics that an endoscopic device is expected to provide. This allows the catheter to pass through curved and confined internal body channels, achieving repeatable and precise positioning of the device without damaging tissue. Early detection and diagnosis is the most effective way to tackle different diseases. This, however, remains a challenge due to the lack of accurate detection technology. The problem is further exacerbated in cases of peripheral lung cancer, in which the tumor grows on narrow bronchi that are difficult to probe.

The present thesis targets designing and developing novel electromagnetic micro actuators based on a ferrofluid levitation mechanism for side-viewing endoscopic applications with Raman spectroscopy and potentially with other modalities, including ultrasound and optical coherence tomography. A tubular micro rotary stepping actuator, custom-designed with a ferrofluid levitation mechanism, is integrated with a Raman probe, for the first time, to scan a probing laser beam sideways for angle-resolved Raman excitation and signal collection, towards enabling the detection of lesion-induced biochemical changes *in vivo* and in real-time.

The side-viewing scanning resolution is enhanced by developing stepping actuation of the micromotor with higher rotational performance. A microfabricated prototype is evaluated using test chemicals, harvested animal lung tissue *ex vivo*, as well as a murine colon model *in situ* and human skin *in vivo*. All the test results show excellent agreement with reported reference data

while revealing a wavenumber accuracy greater than 99%. This thesis indicates that micro actuator-assisted endoscopic Raman spectroscopy is a promising technology for luminal tissue analysis.

Lay summary

The present thesis targets designing and developing novel electromagnetic micro actuators based on a ferrofluid levitation mechanism for side-viewing endoscopic applications with Raman spectroscopy and potentially with other techniques, particularly for full 360° circumferential scans to detect cancer located at the inner surface of the internal organs of humans. A tubular micro rotary stepping actuator, custom-designed with a ferrofluid levitation mechanism, is integrated with a Raman probe, for the first time, to scan a probing laser beam sideways for angle-resolved Raman excitation and signal collection, towards enabling the detection of lesion-induced biochemical changes *in vivo* and in real-time. A microfabricated prototype is evaluated using test chemicals, harvested animal lung tissue, a murine colon model and human skin. All test results show excellent agreement with reported reference data. This thesis indicates that microactuator-assisted endoscopic Raman spectroscopy is a promising technology for luminal tissue analysis.

Preface

Part of this thesis is based on the contributions that have been reported in the following papers:

Peer-reviewed journal papers:

- **S.M.H. Jayhooni**, B. Assadsangabi, K. Takahata, “**A stepping micromotor based on ferrofluid bearing for side-viewing microendoscope applications**”, *Sensors and Actuators A: Physical*, Volume 269, 2018, Pages. 258-268 (Published).
- **S.M.H. Jayhooni**, M. Short, B. Assadsangabi, G. Hohert, C. Du, H. Zeng, K. Takahata, “**Side-view Raman microendoscopy for angle-resolved screening of intraluminal cancers**”, *Advanced Materials Technologies*, Volume 4, 2019, 1900364 (9pp) (Published).
- B. Assadsangabi, **S.M.H. Jayhooni**, M. Short, H. Zeng, K. Takahata, “**Ferrofluid Assisted Micro Rotary-Linear Actuator and Application to Side-Viewing Raman Spectroscopy Endoscope**”, *Smart Materials and Structures*, Volume 29, 2019, 015025 (10pp) (Published).

Conference papers and presentation (abstract peer reviewed):

- **S.M.H. Jayhooni**, M. Short, H. Zeng, K. Takahata, “**Using a stepper motor to enhance the accuracy of endoscopic Raman spectroscopy for improved characterization of peripheral lung cancers**”, SPIE Medical Imaging conference 2018, San Francisco, USA (oral presentation).
- **S.M.H. Jayhooni**, M. Short, B. Assadsangabi, H. Zeng, K. Takahata, “**Side-view Raman microendoscope with Micro stepping motor and its ex-vivo test for real-time cancer detection.**”, IEEE MEMS conference 2019, Seoul, South Korea, Pages. 14-17 (oral presentation, outstanding student paper award finalist).
- B. Assadsangabi, **S.M.H. Jayhooni**, T. Stack, K. Takahata, “**High-aspect-ratio needle-shaped mold fabrication using rosensweig instability in ferrofluids.**”, Transducer conference 2019, Berlin, Germany, Pages. 394-397 (oral presentation).
- **S.M.H. Jayhooni**, B. Assadsangabi, Geoffrey Hohert, P. Lane, H. Zeng, K. Takahata, “**High-speed and stepping MEMS rotary actuator for multimodal 360° side-viewing endoscopic probes.**”, IEEE MEMS conference 2020, Vancouver, Canada (poster).

Furthermore, exact quotations from journal-published papers appear in this dissertation. I have obtained any necessary permission in order to reflect the published results in this dissertation.

Regarding the first and second publications, I have done literature survey, simulations, design, developing and characterization of the actuators. In addition, I have prepared and calibrated the experimental set-ups and conducted Raman tests, including chemical, animal and human measurements. Regarding the third above-mentioned journal paper, I have performed all axial movement experiments as well as rotational experiments (e.g., rotational speed and temperature characterization), including making the experimental set-ups. I have also worked on Raman spectroscopy experiment set-up and obtaining data from chemicals, healthy tissues and cancerous mouse tissues with high and low frequency Raman systems. Regarding the contribution of all collaborators, Dr. Haishan Zeng developed study frameworks as well as assisted with experimental set-ups and device designs (in second and third publications). Babak Assadsangabi assisted me in designing prototypes in all above-mentioned publications and also contributed to prototyping, obtaining results and analyzing part of them in the third publication. Michael Short assisted in training me for Raman spectroscopy system, data analysis and discussing results (in second and third publications). He also assisted in performing some experimental tests in the third publication. In the second publication, Dr. Caigan Du assisted with animal tests and Geoffrey Hohert helped me in designing devices. Finally, all mentioned manuscripts were performed under the supervision of Dr. Kenichi Takahata. He provided me the general ideas and assisted me in following the research path successfully by providing thorough feedback in each and every stage of my research. Dr. Takahata assisted me in writing and improving the manuscripts as well.

Animal tests involving rats in this study are performed under the protocol (A17-0023) approved by the Animal Use Committee at the University of British Columbia (Vancouver, B.C., Canada) according to the guidelines of the Canadian Council on Animal Care. Human tests are conducted under the protocol approved by the BC Cancer Agency Research Ethics Board at the University of British Columbia.

In Appendix section, I have placed the research that I have done related to “High-Aspect-Ratio Needle-Shaped Mold Fabricated using Rosensweig Instability in Ferrofluids”. This research is not directly related to the main focus of the thesis at this stage, though nevertheless, it is related to another medical application of ferrofluids. It will be used for actuating and driving microfluids into targeted areas and drug delivery applications.

Table of contents

Abstract.....	iii
Lay summary.....	v
Preface.....	vi
Table of contents	ix
List of tables.....	xiii
List of figures.....	xiv
List of abbreviations	xxiii
Acknowledgements	xxiv
Dedication	xxv
Chapter 1: Introduction	1
1.1 Medical application of microactuators.....	1
1.2 Side-viewing endoscopes.....	2
1.3 Endoscopic modality	5
1.4 Raman spectroscopy for diagnosis of cancer	6
1.5 Three-dimensional imaging.....	8
1.6 Ferrofluids and their microactuator applications.....	9
1.7 Research objectives	10
1.8 Potential impact of the research	13
1.9 Research methodology	14
1.10 Thesis overview.....	22
Chapter 2: Ferrofluid-enabled micro rotary-linear actuator for endoscopic three-dimensional imaging and spectroscopy	23

2.1	Introduction	23
2.2	Materials and methods.....	25
2.2.1	Working principle and design.....	25
2.2.2	Prototyping	28
2.2.3	Measurement methods and set-ups.....	30
2.2.4	Animal tissue preparation for ex-vivo Raman test	32
2.3	Results and discussions	34
2.3.1	Individual operation for rotational and linear actuations.....	34
2.3.2	Simultaneous operation of rotational and linear actuations.....	36
2.3.3	Thermal characterization	37
2.3.4	Angle-resolved side-viewing Raman spectroscopy	38
	Chapter 3: A stepping micromotor based on ferrofluid bearing for side-viewing microendoscope applications.....	43
3.1	Introduction	43
3.2	Principle and design	44
3.3	Finite element analysis of tubular stator.....	49
3.4	Prototyping	53
3.5	Experimental results and discussions.....	54
3.5.1	Single-coil mode operation.....	54
3.5.2	Thermal characterization	56
3.5.3	Dual-coil mode for fine stepping operation.....	59
	Chapter 4: Side-viewing endoscopic Raman spectroscopy for angle-resolved analysis of luminal organs	63

4.1	Introduction	63
4.2	Working principle and design	66
4.3	Prototyping	69
4.4	Results and discussion	71
	4.4.1 Chemical detection tests	71
	4.4.2 <i>Ex-vivo</i> test with animal lung	74
	4.4.3 <i>In-situ</i> test with rat colon and <i>in-vivo</i> test with human skin	77
	Chapter 5: Miniaturized MEMS rotary actuator for high-speed operation of side-viewing endoscopy	83
	5.1 Introduction	83
	5.2 Principle and design of the miniaturized MEMS rotary stepping actuator 84	
	5.3 Finite element analysis of tubular stator	87
	5.4 Prototyping	91
	5.5 MEMS separator	94
	5.5.1 Fabrication method	94
	5.5.2 Evaluation	97
	5.6 Experimental results and discussions	102
	5.6.1 Speed characterization	102
	5.6.2 Thermal characterization	104
	Chapter 6: Conclusion	109
	6.1 Contributions	109
	6.2 Future work	113

Bibliography	117
Appendix: High-aspect-ratio needle-shaped mold fabrication using Rosensweig instability in ferrofluids	125
A.1 Introduction.....	125
A.2 Fabrication	128
A.3 Experimental results.....	130
A.4 Conclusion	135

List of tables

Table 1.1: Side-viewing catheter used in different endoscopic modalities. 3

Table 5.1: the overall comparison of the features and performance of those three devices
(I, II, III), data are rounded. 108

Table A.1: Physical properties of the two ferrofluids used..... 130

List of figures

Figure 1.1: Schematic arrangement of the Raman system adopted for the study of the side-viewing endoscopic RS device (adapted from references [92], [93] with permission). The tip of the probe is integrated and packaged with the circumferential laser scanner module based on the ferrofluid-assisted custom microactuator (not shown). 18

Figure 1.2: Conceptual schematic of a side-viewing microendoscopic Raman catheter enabled by the developed micro rotary motor embedded in the catheter including micromotor driver module and RS system showing a potential application to peripheral lung diagnosis. . 20

Figure 2.1: Conceptual schematic of the micro rotary-linear actuator. The microactuator is coupled with an optical fiber for its application to microendoscopes, offering the side-viewing function with circumferential and axial scanning of a probing energy beam enabled by the microactuator. 25

Figure 2.2: Device configuration: a) A side view of the rotor/slider-mirror assembly (top), and axial views of the disc magnet with ferrofluid sealant/bearing (section A-A') and the cubic magnet with ferrofluid bearing (section B-B') for hydraulic/pneumatic and electromagnetic actuations, respectively. b) Tubular stator coils (in its planar form before assembly) and their connections with a current controller. 28

Figure 2.3: Fabrication results: a) Rotor/slider assembly with two differently shaped permanent magnets and prism mirror, and b) completed device with photo-patterned stator tube. Reprinted with permission from [94], © 2015 IEEE..... 30

Figure 2.4: Experimental set-ups used for measurements: a) Characterization of rotational and linear actuations, and *in-vitro* RS testing using b) acetaminophen and c) murine tissue samples (figure 2.3a is adapted from reference [94] with permission). 33

Figure 2.5: Characterization of fabricated prototype: a) Rotational speed vs. driving current measured at two different locations of the rotor magnet. b) Linear displacements and their deviation from expected theoretical values as a function of syringe displacement. c) Signals from photodiode array induced by a laser beam continuously rotated at 60 rpm and laterally positioned (at three selected locations) using the developed prototype. d) Measured axial positions (pixel number of the photodiode array) of a rotating laser beam positioned at three different locations with the device..... 36

Figure 2.6: The maximum temperature measured on an outer stator surface of the activated device. The device with and without the rotor assembly was characterized, showing nearly identical characteristic for the two cases. The inset images are IR temperature maps of the device (and a scale of the maps) at indicated current levels. 38

Figure 2.7: Raman test using the chemical sample: a) Raman signals collected with the device showing the spectrum from acetaminophen placed over the plastic (acrylic) tube and that from the tube itself. b) Corresponding Raman signals at the wavenumber of 1645.8 cm^{-1} (acquired over 96 spectra) showing strong peaks upon passage of rotating laser over the location of acetaminophen..... 41

Figure 2.8: Ex-vivo test results. The Raman spectra were acquired at the three stopping angles without tissue sample (at 0°) showing the noise floor, with tumor tissue (at 90°), and with normal tissue (at 270°) (the spectra shifted on the intensity scale for clarity). 42

Figure 3.1: Design of the ferrofluid-assisted micromotor device for circumferential beam scan: a) Axial cross-sectional view; radial cross-sectional views at the cubic magnet rotor (A-A'), showing b) single-coil and c) dual-coil activation modes, and d) at the disc magnet (B-B'). 47

Figure 3.2: Stator circuit assembly and its connection to the driver module developed for the micromotor operation, stator tube is made of polyimide with thinner wall thickness (250 μm) in comparison with previous design (thickness = 1mm). 48

Figure 3.3: The schematic overview of the micro rotary stepping actuator custom developed for the side-viewing endoscopic RS device, showing stepping rotation of the prism mirror coupled with the actuator’s rotor. 48

Figure 3.4: Activation logic of 8-step clockwise rotation of the developed micromotor with the directions of driving currents in the stator coil lines used (the figure only shows a half of the full rotation). 49

Figure 3.5: The magnetic flux density at the location of rotor’s surface beneath the stator carrying 1.0-A current as a function of the wall thickness of the stator tube. 51

Figure 3.6: The distributions of magnetic flux density along a radial cross section of stator tube for three stator lead widths a) 200 μm , b) 800 μm , and c) 2000 μm with 1.0-A current, and resultant flux densities along d) the diametral axis bridging the two active leads and e) the circumferential path at 550- μm inward from the tube’s inside wall for the three lead widths. 52

Figure 3.7: Fabricated samples of a) the rotor component with the prism mirror and b) the completed prototype. 54

Figure 3.8: Rotational speed vs. driving current measured with Device II and Device I. 56

Figure 3.9: Temperature increase vs. rotational speed measured with Device II and Device I. 58

Figure 3.10: Characterization of operating temperature of the micromotor with varying driving current: a) Measured maximum temperature vs. current; IR images of the micromotor driven with the currents of b) 0.8 A, c) 1.0 A, and d) 1.3 A. 59

Figure 3.11: Angular positions measured with the dual-coil activation mode for 8-step rotation..... 60

Figure 3.12: Angular positions measured with the dual-coil activation mode for 16-step rotation..... 62

Figure 4.1: Conceptual schematics of the side-viewing Raman device developed with intended application in peripheral lung cancer detection. A probing laser beam emitted from the Raman probe is circumferentially scanned by rotating the prism mirror stepwise at controlled angles, to collect local spectroscopic data for real-time diagnosis within narrow bronchus.... 65

Figure 4.2: Schematic diagram of the construction of the side-view mechanism enabled with the micro rotary actuator integrated at the tip of a Raman probe. The rotor is electromagnetically driven with an aid of ferrofluid levitation mechanism..... 67

Figure 4.3: A prototype example of the integrated side-viewing RS device functionalized with custom-designed micro rotary stepping actuator and a prototype example. 67

Figure 4.4: The circumferentially scanning a probing laser beam by the prism mirror of the integrated side-viewing RS device. 68

Figure 4.5: The pre-assembly stator tube with the rotor-mirror component showing the ferrofluid bearing inside. 68

Figure 4.6: Micro motor cross section based on a) preceding design of Device II (1.0 mm cubic magnet) b) modified design of Device II (1.3 mm cubic magnet), green circle is the inside of the stator, orange circle (circle with $2r$ diameter) is the maximum areas that the middle of prism connecting to the shaft of the rotor can reach based on theoretical calculation, the experimental measurements are shown with blue dots and they are repeatedly located in the yellow circle. 71

Figure 4.7: Angle-resolved chemical detection test. a) Tubular test set-up with acetaminophen and ibuprofen samples alternately loaded in the open slots (one of ibuprofen samples removed to show the device positioned inside the tube - left), and an axial internal view of the set-up with the two test chemicals (right). b) Raman signals of acetaminophen and ibuprofen samples obtained stepwise, and comparison of the former case with reported data [108] showing high accuracy of the measured peak positions (maximum wavenumber deviations: 0.5%).

Figure 4.8: Ex-vivo test results with bovine lung. a) The side-view probe before inserting the probe to a bronchus (left), the side-viewing probe inserted into a bronchus (right). b) Obtained Raman spectrum with major peak wavenumbers showing good agreements with reported data [73] with low wavenumber deviations ($\leq 0.8\%$).

Figure 4.9: The raw data with fluorescence signals acquired from the *ex-vivo* bovine's lung test.

Figure 4.10: Results from in situ test using a rat model. a) The side-view Raman probe inserted into the colon of the euthanized rat showing emissions of probing laser. b) The side-viewing probe inserted to colon through anus and rectum. c) Raman spectrum obtained from the raw data showing major peak wavenumbers which are matched well with reported peaks of murine model [111] (wavenumber deviations $\leq 0.5\%$).

Figure 4.11: Results from in-situ test using a rat model. Raman raw data and fluorescence signals acquired from the 1-s sampling window at a single step angle. The intensities of the signals are plotted with amplified scales ($1.5\times$ and $3\times$) for higher wavenumber regions ($1900-2400\text{ cm}^{-1}$ and $2400-3100\text{ cm}^{-1}$, respectively) to show that fluorescence curve followed the raw data well (supporting the reliability of the Raman data) in a clearer manner.

Figure 4.12: Results from the test using live human skin tissue. a) The average of 35 data sets of extracted Raman spectrum from different human skin sites acquired while scanning the laser on the skin tissue stepwise exhibiting four major peaks as labeled (blue), the single Raman spectrum obtained from the raw data (red), showing the major peak wavenumbers (with their corresponding signal sources) and results match well with reference data [113], [115], [116] (wavenumber deviations $\leq 0.3\%$). b) Trends of the major peak wavenumbers tracked through the acquired 35 sets of Raman data. The standard deviations of these characteristic wavenumbers were within 2.7 cm^{-1} as shown. 81

Figure 4.13: The raw Raman data and fluorescence signals acquired from the *in-vivo* human skin test. The intensities of the signals are plotted with amplified scaled ($1.5\times$ and $3\times$) for higher wavenumber regions ($1900\text{-}2400 \text{ cm}^{-1}$ and $2400\text{-}3100 \text{ cm}^{-1}$, respectively). 82

Figure 5.1: Design of the novel MEMS rotary stepping actuator circumferential beam scan 85

Figure 5.2: Stator circuit assembly and its connection to the driver module developed for Device III operation as well as placing the flexible stator circuit inside the shrinkable polymer tube 86

Figure 5.3: 2D cross-sectional maps of simulated electromagnetic fields inside the single-layer stator for four different active stator lead widths: a) $200 \mu\text{m}$, b) $400 \mu\text{m}$, c) $600 \mu\text{m}$ and d) $800 \mu\text{m}$ with 1.0-A current feed. 88

Figure 5.4: Simulated maps of electromagnetic fields created by the stator lead width of $200 \mu\text{m}$ in the stator tubes of the Device III (left) and Device II (right), verifying enhanced field strength in the tube stator. 88

Figure 5.5: The distributions of magnetic flux density along the diametric axis bridging the two active leads of Devices II & III with 1.0-A current feed passing the same stator line width (800 μm). 90

Figure 5.6: The distributions of magnetic flux density along the circumferential path at 325- μm inward from the stator circuit's inside wall the diametric axis bridging the two active leads of Devices II & III with 1.0-A current feed passing the same stator line width (800 μm). This circumferential path is the path where the rotor magnet poles passes during each actuator rotation..... 90

Figure 5.7: Rotor component of the actuator including rectangular cubic magnet, the separator and prism mirror. 92

Figure 5.8: Device III stator a) before removing the rod, b) after removing the rod and its inner view of the stator including the polymer tube and flexible circuit showing the inner wall is round enough for the rotor to revolve in it..... 93

Figure 5.9: Completed endoscopic prototype including its packaging tube prior to injecting ferrofluids. 94

Figure 5.10: Process flow steps of the separator patterning and fabrication. 96

Figure 5.11: Two different types of MEMS separator fabricated on the one end of the rotor magnet. 97

Figure 5.12: Ferrofluid is applied to the rotor magnet without the MEMS separator showing the cases of..... 98

Figure 5.13: $\sim 4\mu\text{L}$ ferrofluid is applied to the rotor magnet before locating the rotor in its stator, ferrofluid reaches to the prism mirror..... 99

Figure 5.14: Ferrofluid is applied to the rotor magnet with 8 different amounts from zero to $\sim 4\mu\text{L}$, showing the effectiveness of the separator in making a gap between the two parts of the rotor and preventing ferrofluids leakage from the magnet to the prism mirror..... 100

Figure 5.15: Rotor magnet is subjected to the maximum amount of ferrofluids ($\sim 4\mu\text{L}$) used in the actuator, the two inset figures show two different views of the separator and illustrate the effectiveness of the separator in preventing the ferrofluid to spread to the prism mirror. 101

Figure 5.16: The rotor magnet after being inserted into the stator and run with the rotational speed of 300 rpm, two different perspectives of the rotor after revolving are shown in this figure, the separator successfully blocked ferrofluid to cover the prism mirror components..... 102

Figure 5.17: Measured rotational speed vs. driving current for the developed actuator (Device III) and comparison with those of preceding devices: Device I, explained Chapter 2 and Device II described in Chapter 3. 103

Figure 5.18: Temperature map result with the IR camera around the MEMS actuator after completing the stator prototype. 105

Figure 5.19: Measured maximum actuator temperature vs. driving current for the developed actuator and comparison with those of the preceding designs (Devices I & II). . 106

Figure 5.20: Characterization of operating temperature of the presented MEMS actuator with varying driving current and its IR thermal images. 107

Figure A.1: Schematic view of the fabrication process for ferrofluid-based solid mold of microneedle array with individual needle's coordinate and geometric adjustability..... 127

Figure A.2: Developed fabrication process..... 129

Figure A.3: Measured magnetic thresholds (as a function of magnet distance) for Rosensweig instability of the two ferrofluids used. 132

Figure A.4: Location and height control of ferrofluid spikes (before drying) on the substrate, achieved using EMG 901 ferrofluid with higher saturation magnetization (66 mT) and lower viscosity (8 mPa·s): a) 3×1 array with a uniform height; b) 3×1 array with varying heights..... 133

Figure A.5: Scanning electron microscope (SEM) image of the Parylene-coated mold fabricated using APG 513A ferrofluid with lower saturation magnetization (40 mT) and higher viscosity (150 mPa·s) showing relatively low aspect ratio and large tip radius..... 134

Figure A.6: SEM image of the Parylene-coated mold fabricated using EMG 901 ferrofluid showing high-aspect- ratio structures with sharper tips. 135

List of abbreviations

Abbreviation	Description
A	Ampere
B	Magnetic flux density
EUS	Endoscopic ultrasound
FEM	Finite element method
GI	Gastrointestinal
I	Driving current
ID	Inner diameter
IR	Infrared
MEMS	Micro-electro-mechanical systems
OCT	Optical coherence tomography
OD	Outer diameter
PI	Polyimide
PWM	Pulse width modulation
rpm	Revolutions per minute
RS	Raman spectroscopy
S/N	Signal-to-noise ratio
SEM	Scanning electron microscope
μ_0	Permeability of free space
2D	2-dimensional
3D	3-dimensional

Acknowledgements

I would like to take this opportunity to express my great appreciation and gratitude towards my supervisor, Dr. Takahata who provided me the chance to work under his supervision in this spectacular research. It is my truly honor to be his Ph.D. student and absorb knowledge from this brilliant researcher. He encouraged me to try different ideas and motivated me to put determined efforts to do the research in different circumstances to achieve goals of this research and he patiently helped me to pass this journey successfully.

Also, I would like to thank Dr. Haishan Zeng for his continuous support and providing this opportunity to do some parts of my research in his group at BC Cancer Research Centre. He patiently guided me in my research. I do greatly appreciate all of my supervisory and exam committee members including Professors Edmond Cretu, Mu Chiao, Ryoza Nagamune and Guangrui Xia for their continuous advice, help and time during doing my research.

Finally, I would like to give my regards and extend my appreciation to my friends and colleagues in different research group such as Dr. Takahata's Lab, Dr. Zeng's lab, Dr. Cretu's lab: Babak Assadsangabi, Michael Short, Jianhua Zhao, Geoffrey Hohert, Anthony Lee, Madeshwaran Selvaraj, Carlos Gerardo, Meisam Farajollahi. I do thank each and every one of them for sharing their ideas with me and supporting me in this period of time.

Dedication

To My Lovely Family

Chapter 1: Introduction

One of the most effective devices for imaging and analysing tissue for cancer detection is the miniaturized endoscope. Recently, many research studies have been performed on forward-viewing probes which are appropriate for visualizing tumor growing at the terminal of respiratory system, particularly airway bronchus. This type of probe, however, is not suitable to detect cancers and tumors that are growing on the sidewalls of bronchi particularly in small lumens such as peripheral lung. A side-viewing endoscopic catheter would address the shortcomings of the common forward-viewing probes and provide the opportunity to improve the endoscopic ability in detecting cancers. This capability can be achieved by integrating a micro-electrical mechanical system (MEMS) actuator within the endoscopic catheter for screening and diagnostic purposes in small diameter human luminal organs. In this chapter, the application of micro motors in endoscopic catheters including their advantages and disadvantages are discussed. Also, some examples of micro rotary motors in common endoscopic modalities such as optical coherence tomography (OCT), ultrasound, and Raman spectroscopy (RS) will be illustrated. Then, the significant application of a smart fluid known as ferrofluid in micro rotary motors is briefly reviewed. Furthermore, cancers are categorized briefly based on the tumor growing location, and then, the role of micro motors in RS modality for detecting cancers and particularly lung cancers is discussed. Finally the research overview and objective of this thesis are provided at the end of this chapter.

1.1 Medical application of microactuators

The range of potential applications that micro rotary motors offer is extremely wide, extending from consumer electronics [1]–[3], micro precision systems [4] and robotics [5], [6] and

to microfluidics [7] and medical devices [8]. Medical applications are one of the most promising areas, where the use of MEMS actuators could improve diagnostic and surgical tools and procedures [9]. They are finding a wide range of applications from medical imaging [10], [11] and disease detection [12] to drug delivery [13], [14] and surgery applications [13], [15]. This trend is facilitated through the use of MEMS and their manufacturing technologies [16]. For instance, MEMS techniques are utilized to fabricate robotic actuators for surgically removing tissue from beating hearts [17], flexible surgical robots [18] and other applications in surgery [19]. Also, an OCT scanner has been developed by exploiting MEMS actuator systems for a number of applications including skin cancer diagnosis [20]. Along this direction, micromotors are being used for various endoscopic applications that are enabled through different optical imaging/sensing techniques for lesion diagnosis.

1.2 Side-viewing endoscopes

Endoscopic catheters are a promising application of using micro actuators [21]–[23]. Microendoscopic catheters that are integrated with micro rotary motors together with prism mirrors have been reported to perform the circumferential scan of probing energy beams, in order to detect cancerous tissue inside certain organs of animals [22]–[24] and also the devices have the potential for use in clinical applications [22], [23]. There are various optical imaging/sensing techniques applied for endoscopic diagnosis [25] and MEMS actuators can have a significant influence on enhancing their application particularly in side-viewing endoscopic catheters (Table 1.1). For instance, micromotors have been used to enable side-viewing catheters for OCT [26]–[28] as well as for photoacoustic and ultrasonic dual-mode endoscopy [22]. In the light of this application, Tsai et al. reported ultra-high-speed endoscopic OCT catheters that utilized a

vertical cavity surface-emitting laser (VCSEL) with the built-in scanner and a three-phase brushless micromotor [26]. The flexibility and manoeuvrability are two of the most important mechanical characteristics that an endoscopic device needs to achieve. These features allow the catheter to pass through curvy and confined internal body channels, enabling repeatable and precise positioning of the device without damaging tissue. Moreover, the outer diameter (OD) of the catheter device should be small enough to safely reach a target *in-vivo* location through narrow channels. Therefore, the micromotors' rigid components that are embedded in flexible microendoscopes are required to have a small form, not only in the radial size but also in the axial length. The micromotors that have been adopted in reported side-viewing catheter devices, however, pose critical issues in light of the above needs, limiting functionality and performance of the microendoscopes (e.g., the catheter device reported in [26] had an OD of 3.2 mm and a rigid length of nearly 2 cm). The motor size is largely associated with their bearings, which increase the overall size of the motor, often due to the need for a gear box to compensate for the bearing's large friction [22]–[24].

Table 1.1: Side-viewing catheter used in different endoscopic modalities.

Reference No.	Actuator size, OD (mm)	Rotational speed (rpm)	Endoscopic modality	Catheter rigid tip length size (mm)	Imaging zone (degree)
[22]	2.5	240	photo- acoustic and EUS	35	310
[24]	4.2	156	photo- acoustic	48	250
[23]	3.8	240	photo- acoustic and EUS	38	250
[26]	3.2	1200-72000	OCT	10	250
[29]	1.35		OCT	16	310

[30]	13	1200	OCT	30	355
[31]	12	180	OCT	33	Not provided
[32]	5.3	60	RS	17.8	360
[33]	1.5	Stationary	RS		Not provided
[34]	2.5	600-1200	OCT		350
[35]–[37]	4.7	6000	OCT	28	Not provided
[38]	12	19800	OCT	35	355
[39]	1.2	16500	EUS	3.7	Not provided
[40]	2.6	14400	OCT	16	Not provided
[41]	1	24000 - 192000	EUS	6	Not provided
[42]	1.4	2520	EUS	1 (only motor)	Not provided
[43]	1.6	2700	EUS	6 (only motor)	Not provided
[44]	2.2	3840	EUS	5.9 (only motor)	Not provided
[45]	1.65	3000-12500	OCT	9	Not provided
[46]	2.4	60000	OCT	~ 30 (estimation from a figure)	Not provided
[47]	5	60 - 6000	OCT	~ 40 (estimation from a figure)	Not provided

1.3 Endoscopic modality

MEMS actuators offer a significant opportunity for miniature endoscopic probes to raise their imaging/diagnostic functions within tight spaces *in vivo*. Miniature endoscopic devices serve as a highly effective means for tissue analysis in different luminal organs such as the lung and the gastrointestinal (GI) tract, and there are a variety of ongoing studies for cancer detection in the respiratory tract and urinary system [48]–[51]. Three different modalities in these diagnostic areas include OCT, ultrasound and RS.

OCT offers good resolution in real time for imaging of luminal organs such as respiratory tract [52]–[54], coronary arteries[55], [56] and GI tract [57], [58]. The endoscopic catheters that combined small motors and prism mirrors with the OCT principle were reported to perform circumferential scanning [26]–[28]. However, this technique has limitations in detecting early-stage cancer [59] and in distinguishing tumor beyond 1-2 mm depths due to strong scattering properties with tissues [23]. Endoscopic ultrasound (EUS) offers attractive features such as rapid large-field imaging [60], [61] and broad application areas including gastroenterology [60], [62]–[65] and pulmonology [60], [66], [67]. Yang et al. used dual-mode endoscopy with ultrasonic and photo-acoustic modalities to show its potential clinical application for soft tissue imaging [23], in which a motor was combined to perform circumferential scanning for *in-vivo* imaging. However, characterization of *in-vivo* tissues and detecting early-stage cancer are still challenging with EUS [23].

RS is an appealing optical spectroscopy modality for not only *ex-vivo* assessment but also *in-vivo* diagnosis [68]. For example, RS is utilized in cardiovascular, oncology, neurology, dermatology, and pulmonology areas, including in early-stage cancer detection [68] that is challenging with the other endoscopic techniques outlined above. The principle of RS is based on

detecting molecular vibrations of the tissue that is excited by monochromatic light, usually a laser, in a wide range of wavelengths from near infrared to ultraviolet [69]. The change in the photon energy of the scattered light, as a result of optical interaction with tissue, provides unique information about the chemical constitution of the tissue and diverse energy bond between its molecules (tissue characteristics). Consequently, the technique can be used to distinguish healthy tissues from cancerous tissue [70], [71] for effective depths similar to those of OCT [72]. In particular, RS only collects inelastically scattered light back from the illuminated tissue site and filters out the rest of the light, and the acquired data can be interpreted to detect tumors/cancers at their early stage. The screening throughput achievable with a single endoscopic RS probe is inherently limited. One approach to compensating for this drawback while exploiting its benefit in targeted analysis of localized tissue is to prescreen the luminal organ of interest via x-ray imaging (e.g., low-dose computed tomography) to identify a suspicious site [73], and then perform Raman probing for in-depth analysis of the detected site to determine whether there is a cancer and its exact location.

1.4 Raman spectroscopy for diagnosis of cancer

Lung cancer is the most deadly cancer with a high worldwide mortality rate [74], [75]. The severity of lung cancer is clearly seen in the patient survival rate, which is only 17% five years after diagnosis [74]. One of the main reasons for the significantly low survival rate and poor prognosis for lung cancer is that patients tend to be undiagnosed until the cancer progresses to an advanced stage [74]. Fortunately, statistics also indicate that the five-year survival rate is raised to >70% when the treatment starts with early stage carcinoma *in situ* or when the tumor size is <20 mm in the absence of spreading metastatic cancer (stage 1A) [76]. This clearly shows how finding

lung cancer at an early stage is crucial to save patients' lives. The endoscopic RS method offers a significant opportunity to reach this goal. The common type of RS probe developed by various groups is forward-viewing. Forward-viewing probes are suitable for detecting central airway lung cancers [77] and peripheral lung tumors [73] growing in the peripheral lung close to or on the alveoli (type I tumor-bronchus relationship [78]). The reported studies of forward-viewing RS probes have confirmed the efficacy of the endoscopic Raman technique in distinguishing between tumorous and healthy tissues for cancer diagnosis applications. In particular, cancer detection using forward-viewing RS probe has been reported for a wide range of cancers, including those in the gastrointestinal tract, oral cavity, cervix, brain, breast, skin, bladder, and lung including peripheral lung [68], [73], [77]. They are, however, not particularly effective for finding tumors growing on the sidewalls of bronchi (type II relationship [78]). The emergence of side-viewing RS probes is expected to address this obstacle, thereby broadening the application range of the technology. However, study of side-viewing RS has been limited. For example, one approach that used a stationary prism for atherosclerosis analysis was apparently limited in the angular/circumferential viewing and detection range [33]. A Raman probe that combined a commercial brushless motor for imaging of surface-enhanced Raman scattering was reported for gastrointestinal tract application [32]. The motor used in that study was, however, not only bulky but also limited to continuous rotation with a relatively high speed. This poses fundamental issues for RS data collection and analysis, as tissue should be illuminated by laser for at least ~ 1 s in order to collect sufficient inelastic Raman scattering from a local luminal wall tissue site, and in turn obtain a good signal-to-noise ratio (S/N) Raman spectrum for detecting the probability of lesion locally. The abovementioned work [32] used biomarkers being injected to tissue in order to collect local signals with its limitation of continuous/high-speed rotation. Therefore, side-viewing

RS probes require stepping (or low-speed) scanning of the laser beam. Otherwise, Raman signals that could include those from diseased tissue are averaged out with the signals from normal tissues, which consequently diminishes the chance of finding lesions.

1.5 Three-dimensional imaging

Precise control over the linear and rotational movements of a distally placed microactuator opens up a broad range of capabilities for minimally invasive medical applications in both therapies and diagnoses procedures. Endoscopic imaging and spectroscopic catheters are one of the fields that can significantly benefit from the above-mentioned technology, realizing 3-dimensional (3D) and 4D (i.e., real time) imaging or angle-resolved side-viewing spectroscopy for internal organ diagnosis [23]. These catheters integrate prism-shaped mirrors onto rotary motors to achieve 360° circumferential scanning capability. In order to perform 3D scanning/imaging using these catheters, a common method is to connect the proximal end of the catheter outside to a precision linear stage and then displace the entire catheter while recording 360° circumferential scans [79]. However, repeatable and accurate positioning of the catheter with such actuation configuration is quite difficult, especially when the catheter passes through curvy and/or confined conduits inside the body. Precisely registered linear motion is a critical factor for a reliable and high-resolution scanning/imaging for, e.g., precancerous lesions detection in OCT [26] and therapeutic procedures that utilize laser ablation, which requires high-precision beam positioning/steering for safe and effective lesions ablation [80].

1.6 Ferrofluids and their microactuator applications

Ferrofluids are comprised of magnetic nanoparticles in carrier fluids. These nanoparticles experience rotational and transitional Brownian motion, and can be controlled by external magnetic fields as they are suspended in their carrier fluids.. Ferrofluids have a unique properties with various potential applications in biomedical and mechanical industries [81]. For example, their application have been expanded from optical lens actuator [82], rotary blood pump [83], and electromagnetic energy harvester [84] to driving micro machines [85], microfluidic systems [86] and electromagnetic actuator [87], and high precision machine tools [88].

Micro electromagnetic motors based on a ferrofluid levitation mechanism have been developed to address bearing issues mentioned before [81], [89], [90]. Ferrofluid bearings in micromotors are simple, passive, and cost effective mechanical components with respect to traditional bearing techniques [81]. This novel approach to constructing micromotors was applied to enable micromotors for both linear [89] and rotary actuations [90]. In their designs, the rotary motors were comprised of the permanent-magnet rotor that was electromagnetically driven using stator coils created around the outer walls of the tubular substrate that housed the rotor component, and its magnets were surrounded by ferrofluid layers. The ferrofluid bearing layer of the rotary motor provided the following two significant benefits: 1) The pressure magnetically developed within the fluid lifts the rotor against the inner walls of the stator tube to maintain its radial position at the center of the tube's cross section, allowing for very low friction, and 2) ferrofluid is self-sustained on the poles of the magnetic rotor to levitate the rotor without requiring any external pressurizing means or guiding mechanism, enabling an extremely simplified bearing configuration. Towards microendoscopic applications, Assadsangabi et al. demonstrated a

ferrofluid-assisted micro rotary motor coupled with a prism mirror while eliminating the need for a long cylindrical magnet or a gear box used in/with the motor for its operation [90], [91].

1.7 Research objectives

The main targets of this research are: 1) to design and develop MEMS-based stepping rotary and linear actuator uniquely enabled by ferrofluid components, 2) to design new control methods for the stepping actuation of the micromotor for angular resolution enhancement, and finally 3) to demonstrate the functionality of the side-viewing probe for endoscopic analysis through chemical, animal and human tests. This actuator has a significant potential to be applied to side-viewing probes with different modalities. For instance, as noted previously, the study of side-viewing RS has been limited. According to the best of our knowledge, the only reported motorized side-viewing Raman probe [32] used a conventional DC motor that only allows for continuous rotation with relatively high speed (60 rpm), which will not work for the abovementioned Raman signal collection from unlabeled/raw tissues. In this thesis, for the first time, a MEMS-based stepping micromotor with a ferrofluid levitation mechanism is integrated with a Raman probe. However, the applications of this MEMS actuator are not limited to RS and may expand into other modalities (e.g. OCT). Toward achieving this main objective, this effort focuses on two major aspects of the device. First, the design of the micromotor is configured to raise its electromagnetic actuation performance in continuous rotation including angular speed rate per driving current and low-temperature operation. This design includes the stator tube with significantly smaller wall thickness that is revealed to be a highly effective path to achieving the above both theoretically and experimentally. The second focus is placed on the new control method for the stepping actuation of the micromotor. The angular resolution enhancement is an important step towards the

application to endoscopic catheter. This fine stepping ability is critically important for the RS applications. This is because the RS modality requires a stepping or low-speed motion, instead of continuous high-speed rotation like the OCT case in [26], to properly collect reflected response from the specific part of the tissue (otherwise it only shows the averaged spectrum of heterogeneous tissue with low resolution). This in turn means that finer stepping motion of the probing beam will enable RS mapping with good resolutions. This goal is approached and demonstrated by a driving method that controls the amount and direction of the currents fed to the stator coils, without physically changing of stator coil arrangement on its tube substrate, so that arbitrarily fine stepping can be achieved in a precise manner. Then, this novel MEMS actuator is used to scan a probing laser beam over 360° circumferential coverage, with a programmable stepping profile.

The micro actuator is integrated with a RS probe along with biocompatible packaging that achieves both electrical insulation of the device and the passage of both the laser light and the Raman light without causing substantial spectral noise in the acquired optical signals. One target of this research is to decrease the final diameter of the probe including endoscopic probe, micromotor and its packaging to ~ 2mm facilitating the probes use in small lumen, such as lung bronchi. Toward achieving this final size, the target radial sizes (diameters) of the actuators including their packaging are set to ~ 6mm, ~ 4mm and finally ~ 2mm which are defined in this thesis as Device I, Device II and Device III, respectively. Device I is the first tubular microactuator functionalized by ferrofluid that enables both rotational and axial motions in simultaneous or discrete operation for endoscopic imaging and spectroscopy catheter applications. Device II is a newly designed catheter-based micro rotary motor targeted at enabling side-viewing microendoscopes designed for Raman spectroscopy. This device is configured to raise its

electromagnetic actuation performance in continuous rotation motion and low-temperature operation. It is also the first iteration with stepping actuation enabled for RS applications. Finally, Device III is a novel miniaturized MEMS rotary stepping actuator with lower diameter (~ 2mm) and significantly higher rotational speed and lower power consumption with respect to Devices I & II. This device can be integrated and packaged with various small-diameter catheters used in different endoscopic modalities (e.g. RS, OCT, EUS and photo-acoustic).

Given the reported ability of endoscopic Raman techniques in distinguishing cancers from healthy tissues proven with forward-viewing probes as noted earlier [68], [73], [77], the current work hypothesizes that a side-viewing Raman probe, enabled by integrating additional components including the prism mirror and necessary packaging (through which the probing/collected laser lights pass) with forward-viewing Raman probe, will be similarly effective in tissue analysis and lesion detection via Raman spectrum analyses if the key characteristics (spectrum pattern and peak frequencies) of the signals collected by the side-viewing components are comparable with those reported using the forward-viewing Raman probe for a certain sample being probed.

Another objective is to demonstrate the functionality of the novel probe for angle-resolved side-viewing Raman analysis through chemical, animal and human tests. Toward this, the performance of the integrated side-viewing endoscopic Raman device prototype using test chemicals is first shown and its targeted function for circumferentially localized RS analysis and detection with high accuracy is verified. The side-viewing device is then assessed, for the first time, through an *ex-vivo* test that uses harvested bovine lung by analyzing the Raman signals from its bronchi. Following promising results from this test, we further evaluate and demonstrate *in-situ* RS analysis using rat colon as well as *in-vivo* human skin measurements.

1.8 Potential impact of the research

The target contribution of this research is to develop side-viewing catheter enabled with MEMS-based stepping rotary actuator with different endoscopic modalities in order to distinguish between tumorous and healthy tissues for cancer diagnostic applications particularly, tumors growing on the sidewalls of bronchi (type II relationship [78]). The emergence of side-viewing endoscopic probes is expected to address this obstacle, thereby broadening the application range of the technology. Therefore, in this thesis, a MEMS-based stepping micromotor with the ferrofluid levitation mechanism has been designed, fabricated and integrated with an endoscopic probe, and its functionality for angle-resolved side-viewing Raman analysis is shown through ex-vivo animal lung tissue, in-situ murine colon model, and in-vivo human skin tests for the first time in order to demonstrate the functionality of the MEMS actuator with RS technique. These tests reveals that this developed actuator can be used in other modalities such as OCT and EUS as well.

In addition to the above mentioned target contribution of this research, other resultant impacts are listed below:

- The novel miniaturized motor is custom developed using MEMS technology and uniquely enables arbitrary numbers of steppings per rotation with a programmable scanning angle, key for reliable collection of localized signals from *unlabeled/raw* tissue, and will be essential for successful local lesion detection *in-vivo*.
- This device is the first motorized side-viewing Raman probe that has been fully packaged with a biocompatible polymer that is nearly transparent in Raman spectral wavelength range, which prevents any Raman signal distortions or significant noise creation. In other words, the fibers,

the prism, and the packaging materials are wisely selected and optimized to avoid distortion of collected Raman signals and enhance the signal to noise ratio of the data, eliminating the need of using biomarkers.

- A novel self-aligned assembly method is developed in order to uniquely enable high-precision integration of the micro rotary motor with a selected endoscopic probe with different modalities and accurate optical alignment between them. This integration method, which could be used for probes with wide range of sizes, applications and endoscopic technique, is a key to the successful operation of the developed probe.

1.9 Research methodology

Consequent to the discussion mentioned in the previous sections, first, Device I (OD = 6 mm, including its potential packaging) is designed and developed for side-viewing micro endoscope application, then it is improved and enabled with an axial motion system for 3D scanning. Ex-vivo Raman tests with cancerous and healthy murine tissues have been performed to demonstrate its functionality. For the next actuator design, a catheter-based electromagnetic micro rotary stepping motor based on MEMS technology is designed and developed to enable side-viewing microendoscopes. To investigate the efficacy of the MEMS actuator, it is integrated with RS catheter and fully packaged with biocompatible material in order to be exploited for chemical, animal and human tests. Finally, another novel design and fabrication method is used to enhance the performance of the MEMS actuator and reduce its overall size to broaden its application for scanning smaller lumens. The following methods have been performed to achieve the above mentioned objectives:

A. Microstepping method for controlling of MEMS rotary stepping actuator

To drive the stator coils, a microcontroller is used to program the timings, the directions, and the amount of current so that the rotor makes full rotational motions. As discussed earlier, it is important to increase the number of steps or the resolution in the rotational motion. However, because of areal limitation on the outer surfaces of microendoscopic catheters, physically increasing the number of stator coils is not a practical approach to the need. To circumvent this issue, this study incorporates the microstepping method for the developed micromotor control, to enable precision intermediate stops between two adjacent coil lines, via programmed distribution of driving currents to stator coils, while keeping the original four coil lines on the stator tube.

B. Design, fabrication and characterization of MEMS rotary actuator

Three different designs have been developed in this research, each with different capabilities. Device I is built on the previous research performed with the same actuator dimensions [90]. This design has the potential to simultaneously scan with radial and axial motion. Device II, the next generation of the MEMS rotary, is smaller (~ 4 mm) with higher rotational performance and enabled with a micro stepping controller system for higher scanning resolution. The last generation of the actuator, Device III, is further miniaturized, significantly enhancing the rotational speed, suitable for different modalities required high speed rotational motion, decreasing power consumption and practically operational for endoscopic scanning of small lumens.

The rotors of the developed MEMS rotary actuators are comprised of one or two permanent magnets with either cubic or disc shape, a micro prism mirror, and a linkage shaft or a separator that connects the mirror with these magnets. This rotor component is enclosed in the stator tube and the main driver magnet is magnetized along the radial direction of the catheter device. The

stator coils are arranged on the tube substrate to create electromagnetic fields inside the tube and cause the permanent magnet to rotate. Thin layers of ferrofluid formed between the outer walls of all types of the magnets and the inner walls of the stator tube serve as the self-sustained bearings, in addition to other purposes that will be discussed further onward. To enable the circumferential scanning of the laser beam provided from an RS probe, a 45°-angled prism mirror is attached to the actuator's rotor. The tubular stator component is comprised of two meander-type coils established on the tube substrate. This component is created by first printing the two coils on thin flexible polymer film, each on a different side of the film aligned from each other, and then wrapping and bonding it around the substrate tube as well as inside the tube based on the design. The aligned coils are designed to have four magnetic poles with a 90° phase difference around the tube when passing the driving currents through them in opposite directions. Activating the coils in an alternating manner electromagnetically drives the rotor with a 90° step as defined by the above poles. Experimental characterizations are also performed to compare the performance of each design.

The electromagnetic fields created with the tubular stator with varying design parameters are analyzed using the finite element method (FEM) for evaluation of their effects on the rotor's behavior. This analysis is conducted using a FEM simulation software, COMSOL Multiphysics® (version 5.2 with the Electromagnetics module) and assisted in investigating the effect of the stator tube's wall thickness on the fields provided to the rotor space. For this, the 2D map of simulated fields with a given wall thickness is probed at the central (pole) location of the rotor (cubic magnet) surface when positioned right below an active lead, which is away from the inner surface of the stator tube. Next, the effects of the width of stator leads on the field distribution in the rotor space are assessed using the previous model and operation mode with a fixed wall thickness.

C. Design of Raman probe and its spectrometer system

The forward-viewing Raman probe is comprised of one 200- μm -diameter excitation fiber and six 300 μm diameter collection fibers (Figure 1.1), with the overall length and diameter of 1.6 m and 2.6 mm, respectively [92], [93]. The probe is comprised of ultra-low hydroxyl excitation and collection fibers (2.6-mm overall OD). The excitation fiber is covered with an aluminum coated jacket to prevent optical cross talk between the fibers. The stabilized laser diode with its wavelength of 785 nm (BRM-785, B&W Tek, Inc., USA) serves as the excitation source. The laser power is limited to 120 mW (lower than the level (150 mW) used for clinical human bronchoscopy [77]) to remove any chance of causing damage to tissue under test. A back-illuminated, deep-depletion, near-infrared-optimized charge-coupled-device camera with 400 \times 1340 pixels (20- μm pixel size) (Spec-10:400BR/LN, Princeton Instruments, Inc., USA) is used to measure the light intensity of collected signals dispersed from a sample under test. The band pass filter (SemRock LL01-785, IDEX Health & Science LLC, USA) is used to block the Raman emissions, fluorescence, and laser noises from the excitation fiber, and a long pass filter (a combination of 5-mm-thick Schott RG 715, Schott North America, Inc., USA and a SemRock LP02-785RU, IDEX Health & Science LLC, USA) is used to block all the wavelengths less than 790 nm from the tissue (Figure 1.1). The obtained spectra are calibrated using a standard lamp (RS-10, Gamma Scientific Co., USA) to correct the non-uniform spectral sensitivity of the system. All background fluorescence signals are separated from the raw Raman data using the six-order polynomial curve fit method developed for rapid Raman signal processing [92] that enabled the real-time stepping mode of data collection and analysis as performed in the current study.

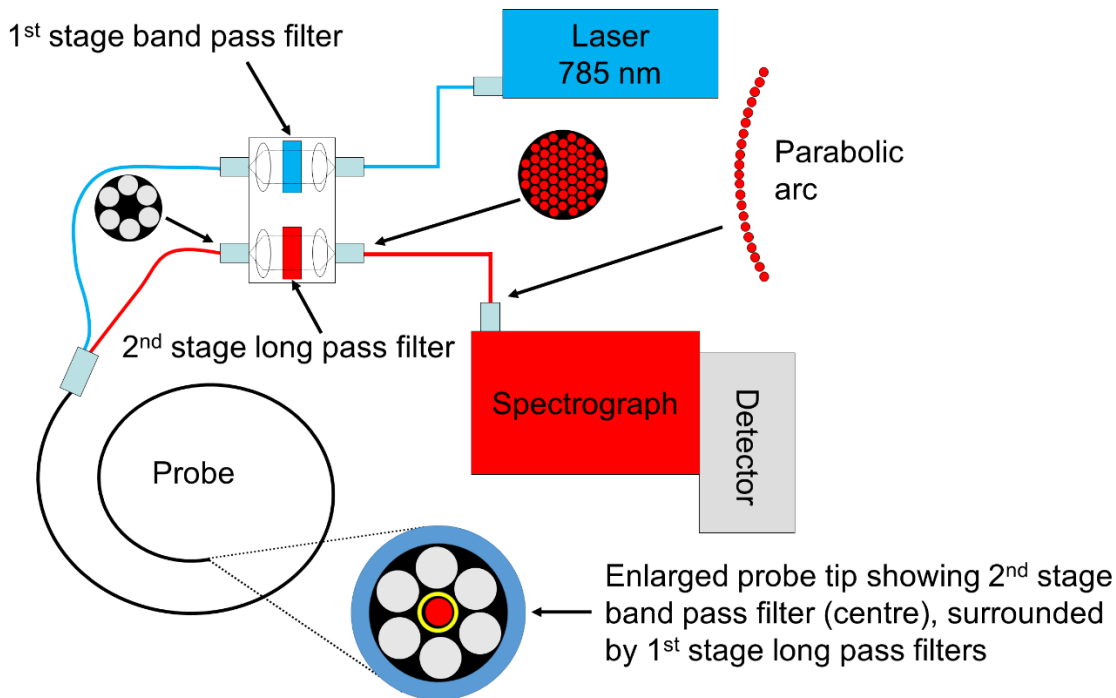


Figure 1.1: Schematic arrangement of the Raman system adopted for the study of the side-viewing endoscopic RS device (adapted from references [92], [93] with permission). The tip of the probe is integrated and packaged with the circumferential laser scanner module based on the ferrofluid-assisted custom microactuator (not shown).

D. Integration and packaging of micromotor with Raman spectroscopy probe

In order to use the micromotor in an endoscopic catheter, it is crucial to integrate and package it with an RS probe. Therefore, for the first time, the side-viewing Raman probe has been fully packaged with a biocompatible polymer that is nearly transparent in Raman spectral range, which prevents any Raman signal distortions or significant noise creation. Toward finding packaging material, extensive research has been conducted as well as different tubular materials have been obtained and tested. The human in-vivo skin tests with the Raman system including its endoscopic catheter have been performed on human fingers covered with those tubular packaging polymers and the results are compared with reported data to achieve appropriate polymers for packaging

purposes. In other words, the fibers, the prism, and the packaging materials are selected and optimized in a way to avoid the distortion of collected Raman signals. Furthermore, a novel self-aligned assembly method has uniquely enabled high-precision integration of the micro rotary motor with a Raman probe and accurate optical alignment between them. This integration method, which could be used for probes with other modalities as well, was a key to successful operation of the developed probe. It is worth mentioning this is the first MEMS-based stepwise micromotor with the ferrofluid levitation mechanism that has been designed, fabricated and integrated with a Raman probe. The conceptual schematic of a side-viewing microendoscopic Raman catheter enabled by the micro rotary motor embedded in the catheter including micromotor driver module and RS system is shown in .

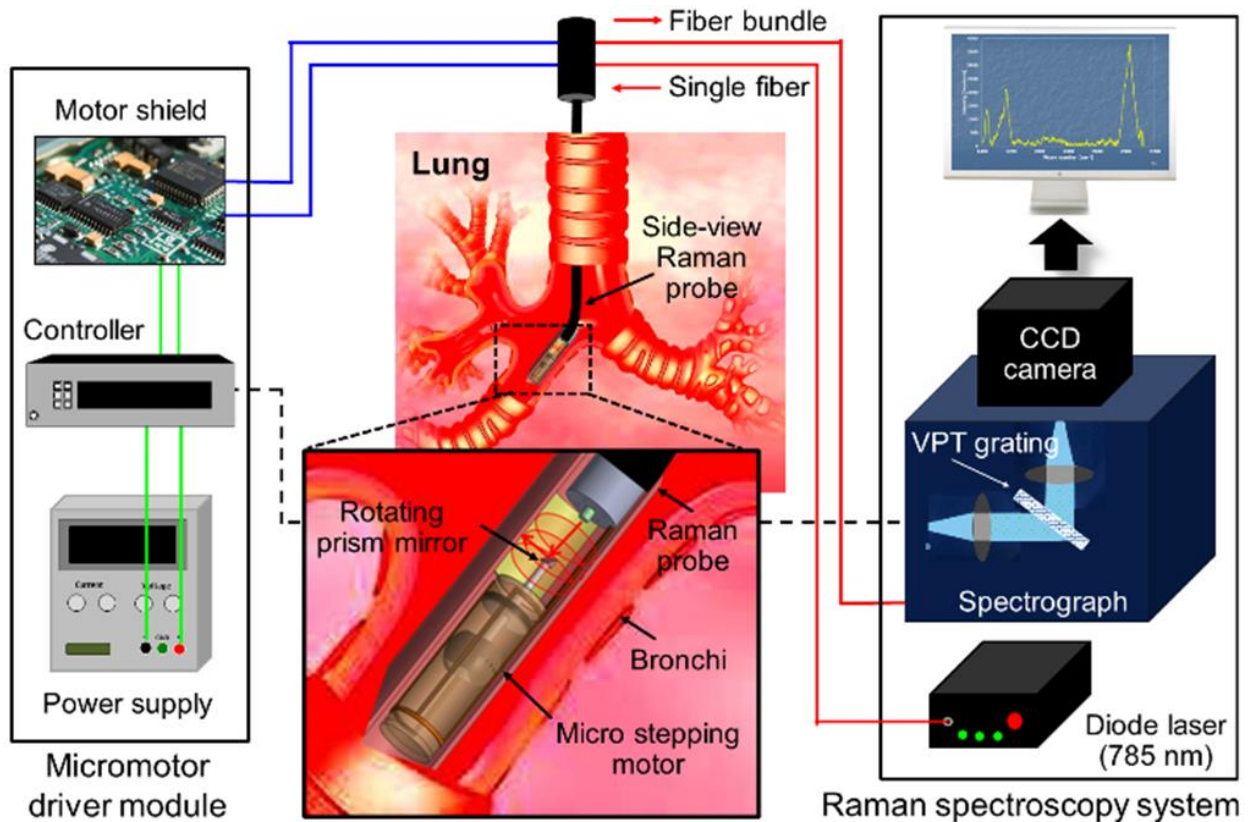


Figure 1.2: Conceptual schematic of a side-viewing microendoscopic Raman catheter enabled by the developed micro rotary motor embedded in the catheter including micromotor driver module and RS system showing a potential application to peripheral lung diagnosis.

E. Investigation of side-viewing Raman probe prototype with *ex-vivo*, *in-situ* and *in-vivo* tests

Given the promising developed side-viewing endoscopic catheter, for the first time, the MEMS-based stepwise micromotor is exploited to demonstrate its functionality for angular resolved side-viewing Raman analysis through *ex vivo* animal lung tissue, *in situ* murine colon model, and *in vivo* human skin tests.

For the *ex vivo* animal experiments, a harvested healthy bovine lung (obtained from a slaughterhouse) that contained many bronchi with various sizes (with luminal diameters from ~10

mm down to ~1 mm or less) is used. The probe integrated with the MEMS actuator is inserted into different bronchi (including right main bronchus as well as upper and middle lobar bronchi) of the right lung and signals are achieved with RS system. The animal in situ test of the developed side-viewing Raman probe is conducted using the colon of a rat model. Raman scanning of mucosal tissue layers of the colon (ID = ~4 mm) is performed over ~30 minutes after sacrificing the rat with carbon dioxide through a standard procedure. The Raman probe is inserted enough through the anus and rectum of the rat to reach the rat's colon. All the work involving rats in this study is performed under the protocol (A17-0023) approved by the Animal Use committee at the University of British Columbia (Vancouver, B.C., Canada) according to the guidelines of the Canadian Council on Animal Care. Male Wistar rats are euthanized following the standard operating procedure (ACC CCM 2012-03 Euthanasia of Adult Rodents). In brief, rats are first anesthetized by isoflurane, followed by euthanasia with CO₂ until no breathing was observed. The death of animals is further confirmed by no heartbeat and respiration. Regarding the human skin tests, the active tip portion of the probe was all surrounded by healthy human skin (of the fingers), while rotating the mirror/laser stepwise. This test is conducted under the protocol approved by the BC Cancer Agency Research Ethics Board at the University of British Columbia. Tissue data (including the fluorescence and Raman signals) are achieved by the RS system and the Raman signals are extracted by the Raman signal processing technique [92]. All the Raman tests have been performed in collaboration with Dr. Zeng's research group at BC Cancer Research Centre.

1.10 Thesis overview

This dissertation is comprised of 6 chapters plus appendix. The research background related to MEMS micromotors and endoscopic catheters (utilized in OCT, RS and EUS), research objectives and the general methodology are explained in Chapter 1.

The main focus of Chapter 2 is the design, development and characterization of a micro rotary-linear actuator for 3D scanning. Then, the actuator's efficacy is investigated with Raman tests in chemicals as well as healthy and cancerous animal tissues. A novel MEMS rotary stepping motor is designed and developed for the use in RS catheters for high resolution lumen scanning in Chapter 3. The actuator is then characterized and compared with the preceding actuator described in the previous chapter (Chapter 2) in order to show the advantages and performance of the new actuator. In Chapter 4, the integration and packaging of the micromotor and RS probe is described. Also, it shows the importance of selected materials such as polymer tubes and prisms in obtaining real tissue Raman signals without any significant signal distortion. Toward this, the performance of the novel fully packaged side-viewing Raman probe enabled with the MEMS-based stepwise micromotor in angular resolved side-viewing Raman analysis through *ex-vivo* animal lung tissue, *in-situ* murine colon model, and *in-vivo* human skin tests is investigated thoroughly. Chapter 5 proposes a novel design which is promising in terms of reducing power consumption, enhancing rotational speeds and also decreasing the overall size of the MEMS rotary actuators, broadening its potential use to smaller lumens, particularly the peripheral lung. Finally, Chapter 6 expresses the contribution of this research to the broader medical and engineering research fields and provides an outline of future work and direction. Appendix A demonstrates the additional applications of ferrofluids in creating micro needles for actuating microfluidics for medical applications such as drug delivery.

Chapter 2: Ferrofluid-enabled micro rotary-linear actuator for endoscopic three-dimensional imaging and spectroscopy*

2.1 Introduction

In this chapter, this work develops the first tubular microactuator (Device I) functionalized by ferrofluid that enables both rotational and axial motions in a simultaneous or selective manner for endoscopic imaging and spectroscopy catheter applications. A layer of ferrofluid attracted on the magnetic rotor/slider lifts it off the inner walls of the catheter tube, offering a near friction-less electromagnetic revolution of the rotor and/or its sliding motion along the catheter's axis controlled by a fluidic pressure. A device prototype coupled with a prism mirror is microfabricated and evaluated to verify the effectiveness of the device design for 3D scanning of a probing laser beam. In light of the device performance, the development of the new microactuator which can produce simultaneous linear and rotary motions is investigated, with the goal of performing a full 3D endoscopic scanning/imaging and diagnosis without the need for external catheter displacement. To achieve this functionality, lateral/axial actuation of the ferrofluid-levitated magnet rotor is designed to be controlled fluidically, while the angular actuation is electromagnetically implemented (Figure 2.1). The current work particularly focuses on design, developing and

* Part of this chapter appeared in the following publication:

B. Assadsangabi, S.M.H. Jayhooni, M. Short, H. Zeng, K. Takahata, "Ferrofluid Assisted Micro Rotary-Linear Actuator and Application to Side-Viewing Raman Spectroscopy Endoscope", Smart Materials and Structures (Published).

characterization of the micro rotary and linear prototype based on a preliminary design [94] and experimental demonstration of the device including its *ex-vivo* test for its endoscopic applications.

To this end, the current study in this chapter adopts RS modality as the platform for the targeted application. In this chapter, two preliminary tests are performed to evaluate the rotary actuation of the prototype using *in-vitro* set-ups coupled with a common (forward-viewing) Raman probe. The first test is conducted to show the detection of a sample chemical through circumferential laser scan by the rotating device. The second test is arranged to probe healthy and tumor mouse tissues located at different angular positions around the device, and demonstrate collection of RS signals from the tissue samples *ex vivo* for their spectrum analyses in a manner similar to the first test.

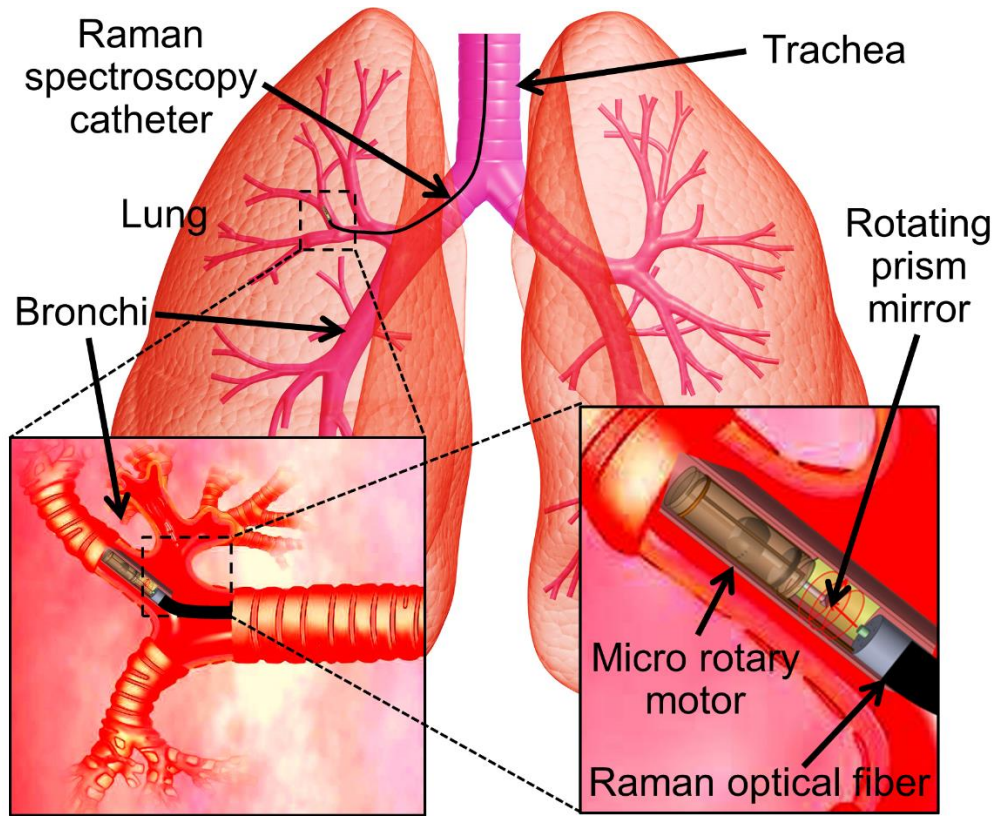


Figure 2.1: Conceptual schematic of the micro rotary-linear actuator. The microactuator is coupled with an optical fiber for its application to microendoscopes, offering the side-viewing function with circumferential and axial scanning of a probing energy beam enabled by the microactuator.

2.2 Materials and methods

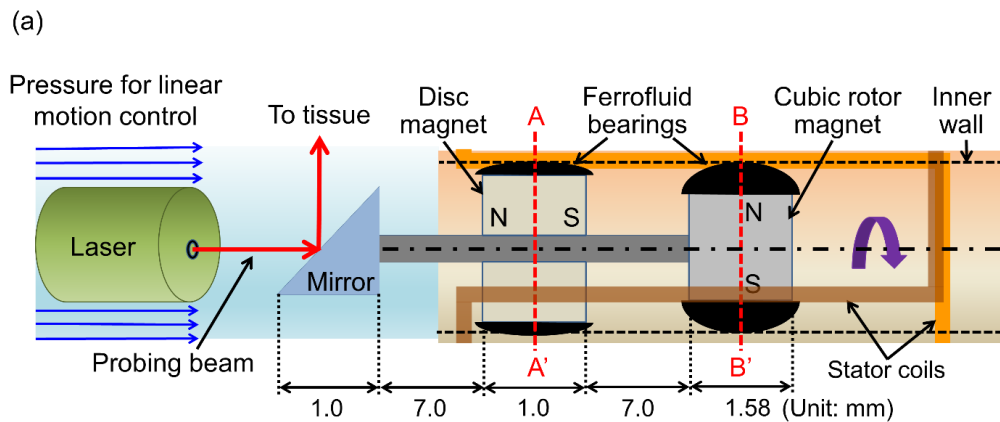
2.2.1 Working principle and design

By applying ferrofluid onto a magnet, which is the rotor/slider of the developed microactuator, ferrofluid flows towards the two poles of the magnet with the highest magnetic field gradient and accumulates on those areas. The magnet with the accumulated ferrofluid layer is lifted up above its substrate due to the magnetic pressure developed in the fluid. Therefore, ferrofluid not only provides lubrication for the rotor/slider and lower the friction forces during actuation/motion, but also acts as a physical support that levitates the component above the inner surfaces of the stator

tube without external pressurizing means. This in turn means that ferrofluid works as the bearing for the tubular actuator. Furthermore, this fluidic bearing is sustained on the magnet poles due to the magnetic attraction force and follows the magnet as it rotates and/or slides without the need for any special assembly and/or alignment of the bearing in the motor construction, which could result in lower manufacturing cost for the device.

The developed microactuator design includes two magnets that are lifted and supported by the ferrofluid bearing inside the tube (Figure 2.2a). The first magnet is cubical with 1.58-mm side length, and has radial magnetization with respect to the catheter's radial axis. This magnet is electromagnetically actuated/rotated using the stator coils that are arranged circumferentially on the outer surface of the tube. The stator circuit is comprised of two meander-type coils. Each coil is microfabricated on each side of a flexible polymer film. The circuit on the film is then wrapped and bonded around the catheter tube to set the stator for the rotational magnet. Figure 2.2b depicts the stator circuitry design and its connection with the power supply and the switching controller. The particular coil design creates four magnetic poles with 90°-phase difference around the tube as the actuation current is applied to the coils (Figure 2.2a; Section B-B'). In order to create continuous rotation, the stator coils are energized sequentially with specific current directions, so that the magnet rotates 90° at each step and align its poles with the magnetic field direction created by the stator coils. The second magnet has a disc shape (2-mm diameter with 1-mm thickness, magnetized in its axial direction) that is physically linked to the cubic magnet. The disc magnet is axially magnetized, i.e., the magnetic field gradient is highest around the disc's perimeter, therefore ferrofluid forms a uniform ring on those areas and lift the magnet inside the tube (Figure 2.2a; Section A-A'). The ring-shaped ferrofluid layer on the disc magnet also serves as a sealant for the rotor/slider. When a fluidic pressure is applied on one side of the ferrofluid-sealed

disc magnet, the whole rotor/slider assembly is forced to move along the axial direction of the tube (just like a piston). This axial motion can be bidirectional depending on the polarity of applied gauge pressure (i.e., positive/negative pressure for forward/backward motion) with respect to the atmospheric pressure on the other side of the disc magnet. In order to reflect an incoming energy beam to the radial direction of the catheter, a prism mirror is bonded on the end of a linkage shaft that passes through the disc magnet and connects it to the cubic magnet on the other side. The entire rotor/slider assembly can then be linearly displaced by applying pneumatic or hydraulic forces while the assembly is electromagnetically rotated inside the catheter tube. The axial length of the stator coils is designed to be 14 mm (Figure 2.2b), which allows for the lateral scanning range of the rotating mirror along the catheter's axis to be ~13 mm. Since the two (electromagnetic and pneumatic/hydraulic) actuation mechanisms are decoupled physically, the simultaneous and precise control of the rotational and lateral actuations can be achieved with no cross talk between them.



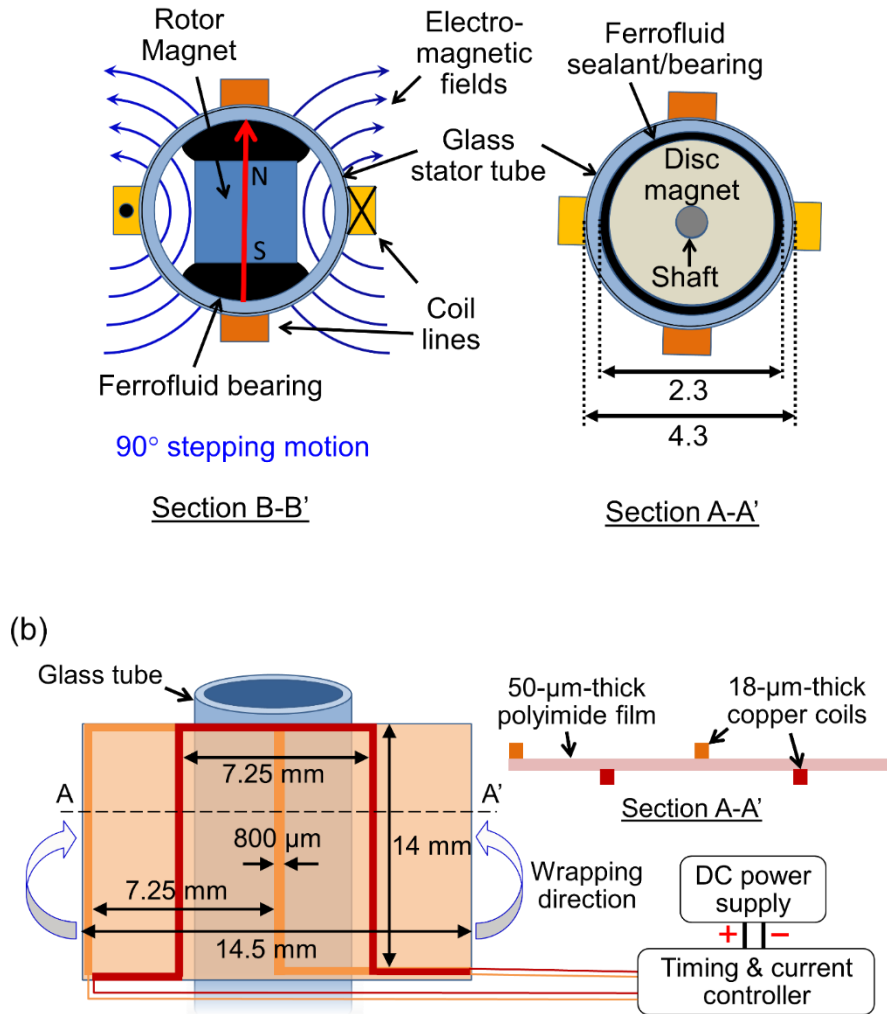


Figure 2.2: Device configuration: a) A side view of the rotor/slider-mirror assembly (top), and axial views of the disc magnet with ferrofluid sealant/bearing (section A-A') and the cubic magnet with ferrofluid bearing (section B-B') for hydraulic/pneumatic and electromagnetic actuations, respectively. b) Tubular stator coils (in its planar form before assembly) and their connections with a current controller.

2.2.2 Prototyping

The fabrication of the stator circuit component is performed using a flexible double-sided copper-clad polyimide film (Pyrlux AP8525R, DuPont, NC, USA), in which the polyimide layer has a thickness of 50 μm and the copper-clad layer on each side of the film has a thickness of 18 μm. A photolithographic process is used to fabricate meander-shaped copper coils on both sides

of the film. For this, dry-film photoresist (PM240, DuPont, NC, USA) is first laminated and photo-patterned on both sides of the film substrate, followed by wet etching of the copper layers to create the desired coil patterns. The fabricated flexible stator is then bonded around a supporting (stator) tube using epoxy. For this proof-of-concept work, a glass tube with 2.3-mm inner diameter (ID) and 1-mm wall thickness is utilized as the tubular substrate for the flexible stator. To assemble the rotor/slider component, two NdFeB permanent magnets (K&J Magnetics Inc., PA, USA; surface magnetic flux density ~ 500 mT) with the shapes of 1.58-mm cube and 2.0-mm-diameter disc are connected together with a 0.8-mm-diameter steel shaft. Finally, a 45° -angled prism mirror (Tower Optical Co., FL, USA) with 1-mm size is bonded at the free end of the shaft to complete the assembly (Figure 2.3a). A commercial oil-based ferrofluid (EFH1, Ferrotec Co., NH, USA; relative permeability ~ 2.6) is applied onto both magnets, and then the entire assembly is inserted into the glass tube. The ferrofluid on the magnets forms a layer between each magnet and the inner wall of the glass tube (i.e., given the magnets and tube inner wall dimension differences, the ferrofluid layer thickness was approximately between $70\ \mu\text{m}$ (on the cubic magnet vertices) to $360\ \mu\text{m}$ for both cubic and circular magnets) to serve as the self-sustained fluidic bearing as described earlier. Figure 2.3b shows a completed prototype device.

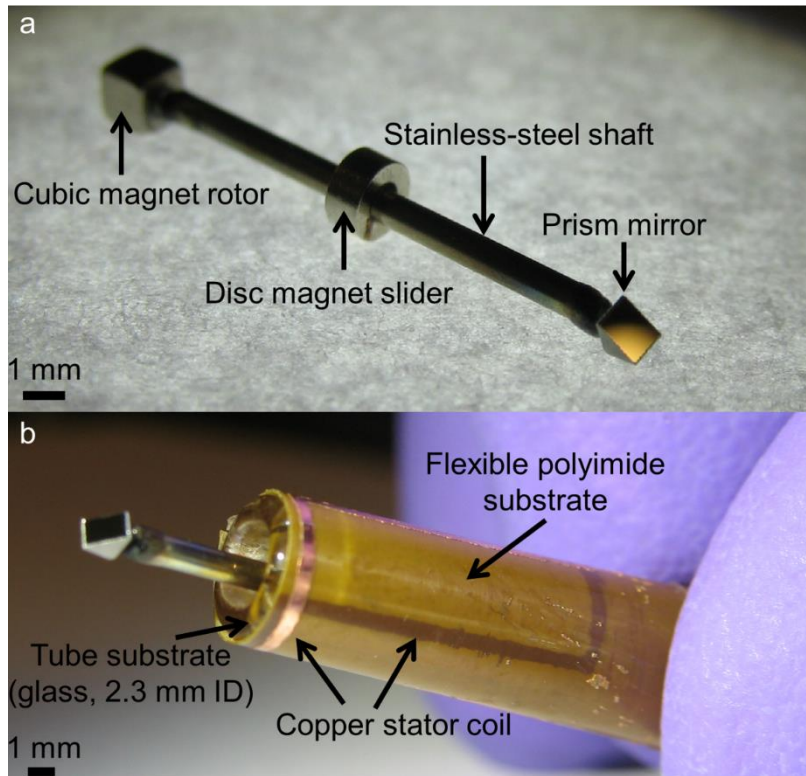


Figure 2.3: Fabrication results: a) Rotor/slider assembly with two differently shaped permanent magnets and prism mirror, and b) completed device with photo-patterned stator tube. Reprinted with permission from [94], © 2015 IEEE.

2.2.3 Measurement methods and set-ups

The fabricated device prototypes are characterized for both rotational and linear modes individually and simultaneously. These tests are implemented using the set-ups based on the configuration shown in Figure 2.4a. For linear actuation, a precision syringe pump (Model 997, Sono-Tek Co., NY, USA) is used to feed control amounts of air or water to the device. For this, a syringe (ID = 4.6 mm) filled with the fluid is connected to one end of the stator glass tube using flexible tubing, and resultant displacement of the rotor/slider assembly is measured using a laser displacement sensor (LK-G32, Keyence Co., ON, Canada) by aligning it on the tubular axis of the device (for this measurement purpose, the prism mirror at the end of shaft is replaced with a flat

29- μm thick piece of Metglas (Metglas®2826MB Magnetic Alloy) foil to enable reflection of laser beam back to the displacement sensor). To characterize rotational actuation, a laser beam is directed to the mirror and the reflected beam bent at the prism mirror is captured by a linear photodiode array (TSL1402R, AMS-TAOS Inc., TX, USA; axial pixel size = 63.5 μm) positioned ~ 5 mm away from the mirror. The photodiode array is connected to an oscilloscope to display photo-induced voltages caused by the incident beam. The displacement sensor was used as the laser source for this test.

To characterize the thermal response of the developed prototype due to Joule heating effects, an infrared (IR) camera (VarioCam HiRes 1.2M, Jenoptik AG, Germany) is utilized to map temperature over the stator surface during the operation. The temperature read with IR signals is known to be affected by the emissivity of the material to be measured. In particular, measurement of metals often leads to unreliable readings given their low emissivity properties[95]. Thus, to circumvent this issue while recording device temperature more accurately, temperature reading is performed on the polyimide substrate, at a location adjacent to the coil's copper wire (at which temperature should be close to that of the copper wire that is hottest on the stator) in the tests.

For the Raman-based measurement tests, the developed prototype is first used to detect acetaminophen as a reference standard in the experimental set-up shown in Figure 2.4b. Acetaminophen is chosen due to strong Raman signal and temporal stability as well as its easy handling requirements. In this set-up, the device is inserted inside an acrylic transparent tube (ID = 8 mm, wall thickness = 1 mm) and then a pressed acetaminophen sample is placed on the outer surface of the tube, emulating the presence of anomaly (e.g., cancerous tissue) on a wall of a conduit organ. After aligning the Raman probe device with the test tube, the mirror is rotated with 4 steps of 90° motion for 1.5-s switching time (i.e., 360° in 6 s) while continually acquiring the

Raman spectral data with a 1-s exposure time (resulting in six data sets acquired in one rotation). As shown in Figure 2.4b, the acetaminophen sample is placed away from the mirror's stopping angles to assess whether enough data can be collected during the transitional scan between the stopping angles to detect the sample. Another Raman test uses *ex-vivo* tissues harvested from a mouse (refer to section 2.4), in which healthy and tumor tissues are evaluated through Raman spectra collected from them. Given low levels of Raman signals from these tissues, this test is implemented with another set-up shown in Figure 2.4c, which utilizes a 3D printed plastic, cylindrical fixture (ID = 20 mm) with through holes where the sample tissues are placed to be probed by laser directly. The Raman test for Acetaminophen detection uses a custom-designed probe coupled with a commercial spectrometer system covering a frequency range of 1500–3400 cm^{-1} (Holospec, Kaiser Optical Systems, Inc., MI, USA). For the *ex-vivo* test, another spectrometer with a lower frequency range (200–2000 cm^{-1} ; Verisante Core, Verisante Technology Inc., BC, Canada) is selected from a preliminary test that showed a richer density of Raman emissions with the corresponding frequency range and system for the particular tissue samples used.

2.2.4 Animal tissue preparation for ex-vivo Raman test

A popular murine model C₃H/HeN was used to prepare tissue samples. All animal experiments were performed according to a protocol approved by the University of British Columbia Committee on Animal Care (certificate number: A10-0338). The mice were housed under specific pathogen-free conditions, with a 12-hour light-dark cycle at the animal facility. Squamous cell carcinoma (SCCVII) tumors were generated by subcutaneous injection of 3.6×10^6 cells in 50 μL phosphate buffered saline into the back of a female mouse. When the estimated tumor volume reached 90-120 mm^3 (~10 days after tumor inoculation), the mouse was sacrificed by CO₂ following the standard operation procedure. All mice were shaved before the excision of

tumor tissue and normal skin each consisting of a sample piece with approximately $5 \times 5 \times 3 \text{ mm}^3$ in size (selected to be slightly larger than the size of the through hole made in the cylinder fixture). These tissue samples were squeezed in the fixture's through holes (as shown in Figure 2.4c) to hold them in place. No additional processing of the tissue was performed. The Raman measurements were completed within 10 min. The total time from sacrificing the mouse to completing the measurements was ~ 60 min.

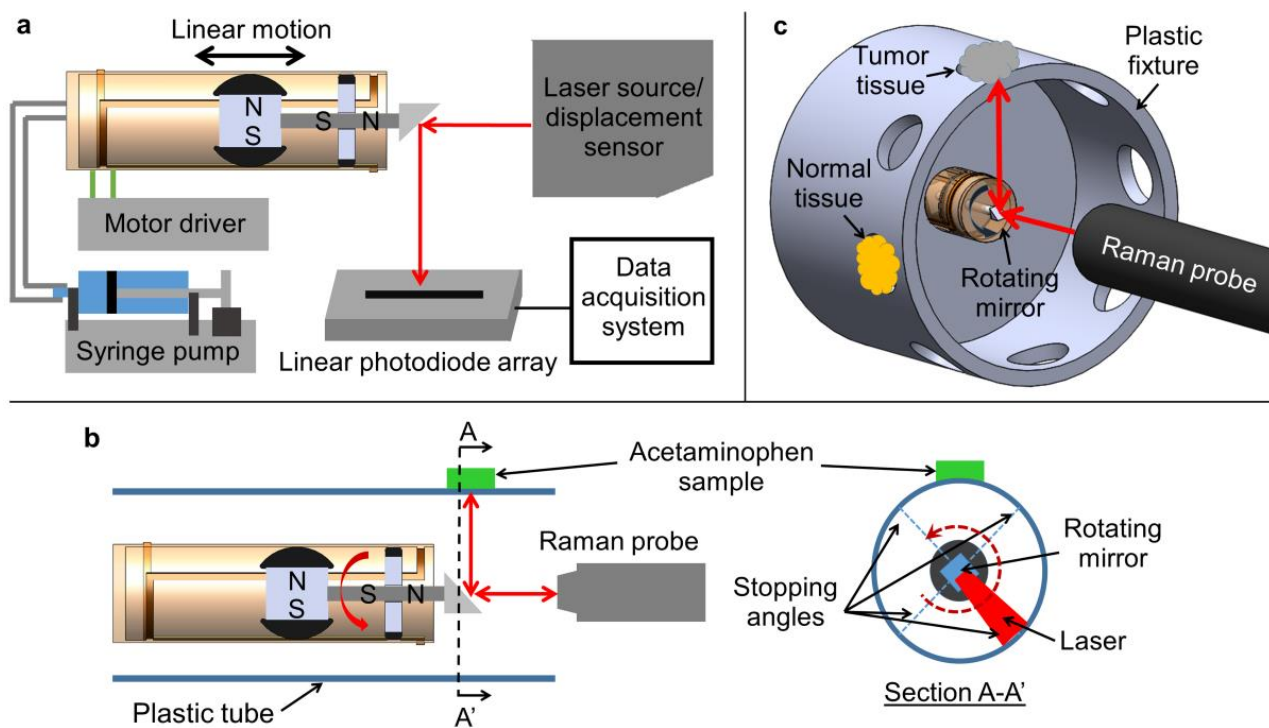


Figure 2.4: Experimental set-ups used for measurements: a) Characterization of rotational and linear actuations, and *in-vitro* RS testing using b) acetaminophen and c) murine tissue samples (figure 2.3a is adapted from reference [94] with permission).

2.3 Results and discussions

2.3.1 Individual operation for rotational and linear actuations

The fabricated prototype was verified (using the experimental set-up shown in Figure 2.4a) to produce stable rotation at different speeds by varying the switching time of the actuating current, which resulted in circumferential scanning/rotation of the reflected laser beam. In order to characterize the rotation speed of the fabricated device, the switching time was shortened from the initial value of 500 ms (i.e., 30 rpm) to raise the speed. As the revolving rate was increased, higher driving currents were required to maintain stable rotations. The need for higher currents was due to the fact that as switching time intervals were shortened at higher rates, larger torque/acceleration values were required for the revolving rotor to catch up with the higher speeds of the switching current and maintain stable rotation. Therefore, the minimum current that could sustain a stable rotation of the rotor was characterized while raising the switching speed. Figure 2.5a illustrates the measurement results from this characterization, displaying the relationship between the revolution speed and the driving current up to 2.1 A. This largest amount of current is estimated to provide a magnetic flux density (B) of ~ 0.03 mT at a distance of 1.36 mm, the largest distance to the side surfaces of the rotating cubic magnet, based on Ampere's law for a straight current-carrying wire, i.e., $B = \mu_0 I / (2\pi d)$, where μ_0 is the permeability of free space, I is the driving current, and d is the radial distance from the stator wire. As shown, the tests were performed with two different positions of the magnet rotor with respect to the axial length (14 mm) of the stator coil, i.e., at the midpoint and at an edge of the stator, to assess the rotor's positional effect on its rotational speed. The results show that the required actuating current was slightly higher for the case that the magnet was located at the edge of the stator compared the case in the center of the stator. This outcome is likely related to the fact that, when the rotor magnet was at the edge of stator, a part of the magnet

was off from the current carrying lines of the stator, causing a certain reduction in the torque exerted on the magnet.

The axial displacement of the rotor/slider was measured as a function of syringe's displacement. For this, the syringe pump was programmed to displace water with a total volume of 20 mm^3 in five equal steps. The experiment was repeated three times and the average output displacement was plotted in Figure 2.5b. As can be seen, there was 3-4% deviation from the theoretical displacement values (calculated presuming fully incompressible medium injected from the syringe). This minor error might have been caused by the following two potential factors; 1) small amount of air bubbles trapped in the hydraulic system, and 2) water leakage on the cubic magnet side of the rotor that was in direct contact with water. This leakage can be avoided if the actuating medium (i.e. water) is applied from the disc magnet side that provides a uniform sealing around the inner walls of the stator tube.

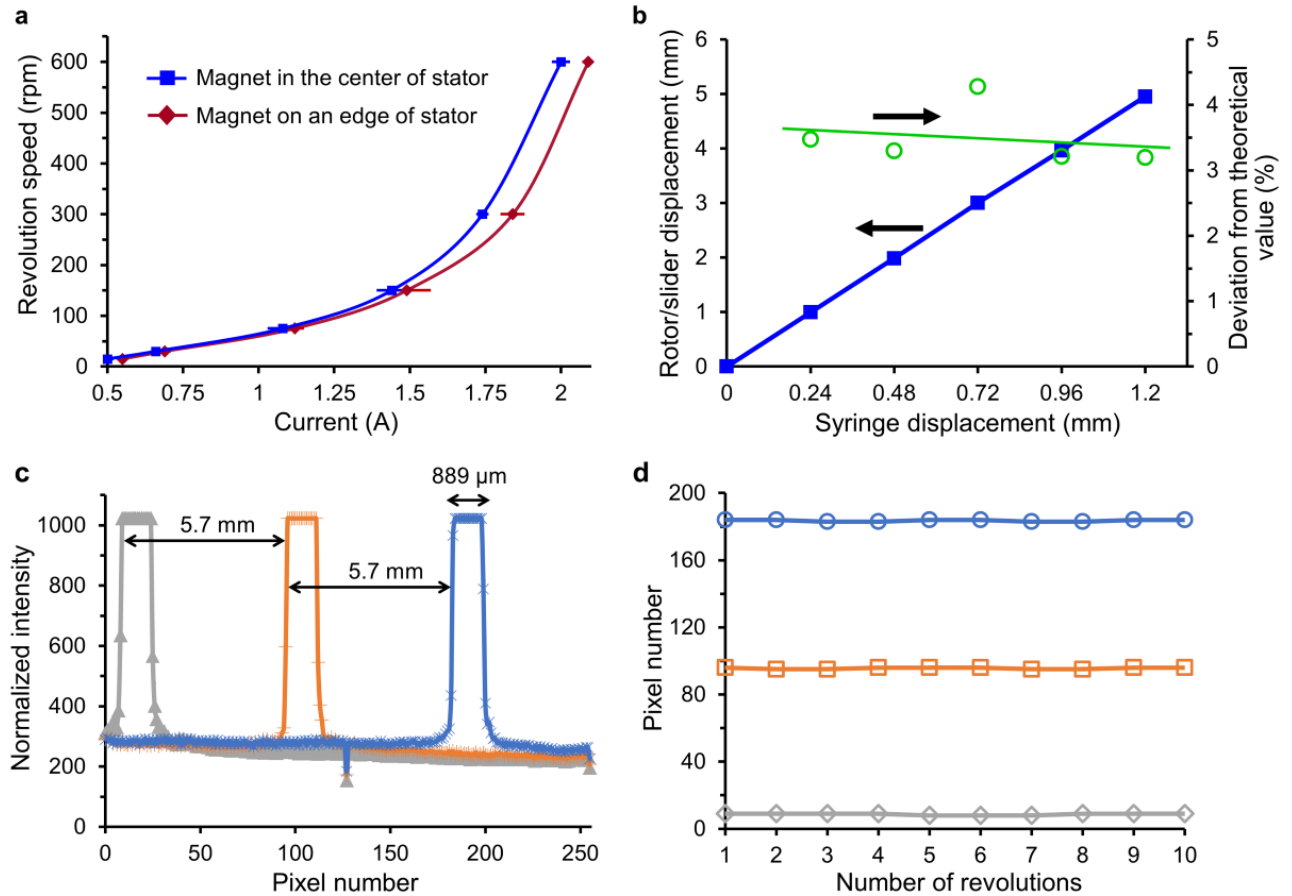


Figure 2.5: Characterization of fabricated prototype: a) Rotational speed vs. driving current measured at two different locations of the rotor magnet. b) Linear displacements and their deviation from expected theoretical values as a function of syringe displacement. c) Signals from photodiode array induced by a laser beam continuously rotated at 60 rpm and laterally positioned (at three selected locations) using the developed prototype. d) Measured axial positions (pixel number of the photodiode array) of a rotating laser beam positioned at three different locations with the device.

2.3.2 Simultaneous operation of rotational and linear actuations

The intensity signals from the photodiode array were recorded while simultaneously rotating and sliding the rotor (thus axially scanning a rotating laser beam) and positioning the rotor at three different axial locations (at around both ends and at the midpoint of the full axial stroke (~13 mm) of the actuator) (Figure 2.5c); the spatial pulse width at each location corresponds to the size of

laser spot on the photodiode array. The lateral actuation was pneumatically driven in this test. To characterize the axial rotational stability (position variation along the axial direction) of the actuator rotor, ten full 360° scans were performed at each measurement location. The measurement results are shown in Figure 2.5d, which indicates that the position variation (at an edge of each pulse signal – refer to Figure 2.5c) was within two pixels of the linear photodiode (i.e., less than 127 μm) at all the three locations. This result signifies a significant improvement in terms of axial rotational stability compared with the preceding device only with a rotational functionality [91]. This improvement is likely led by the use of air pressure applied on the disc magnet, which should constraint random/unintended axial motions of the rotor unlike the previous device without the axial pressure. These characterization results confirm the fundamental capability of the developed microactuator for simultaneous precision control of 360° rotation and full linear scan of a prism mirror within a catheter tube.

2.3.3 Thermal characterization

The thermal effects of the ferrofluid bearing and its dynamics (e.g., frictional losses) on the temperature rise in the device were characterized by powering the device under two conditions, with and without the rotor assembly in the device. In each set of tests, the actuation current was held constant for 5 min to ensure that the device temperature was stabilized, and then thermal images of the device were captured. Once the device cooled down to room temperature (~27 °C), the next current level was applied. The device temperatures with varying currents applied in the abovementioned manner were plotted through the analysis of the recorded IR images (Figure 2.6). These results clearly indicate that the actuation of the device did not cause the bearing to produce any heating effect large enough to raise the stator's temperature, given that the two sets of acquired results (i.e., with and without rotor) are almost completely overlapped as seen in Figure 2.6,

presumably owing to the low-friction ferrofluid bearing used in the device. The results also suggest that in order to use the developed micromotor for endoscopic applications, the actuation current may have to be limited up to ~ 1.3 A so that the maximum device temperature becomes no more than 40 °C [96].

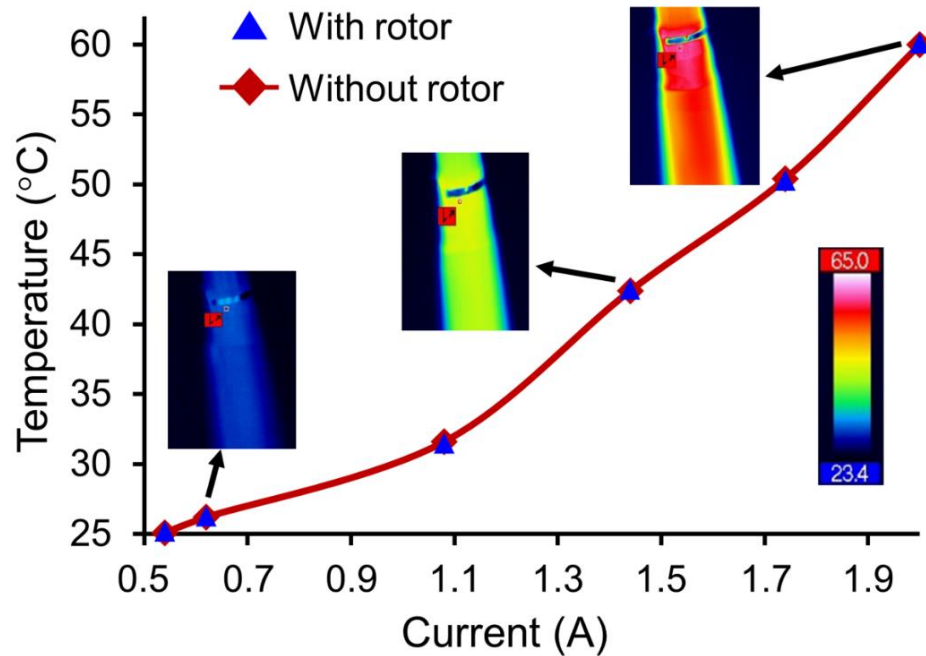


Figure 2.6: The maximum temperature measured on an outer stator surface of the activated device. The device with and without the rotor assembly was characterized, showing nearly identical characteristic for the two cases. The inset images are IR temperature maps of the device (and a scale of the maps) at indicated current levels.

2.3.4 Angle-resolved side-viewing Raman spectroscopy

As noted previously, for conducting this Raman experiment, Raman system is comprised of laser diode with its wavelength of 785 nm is used as the excitation source, spectrometer systems covering two different frequency range, CCD camera with 400×1340 pixels ($20\text{-}\mu\text{m}$ pixel size), long and band passed filters and finally excitation and collection optical fibers in order to obtain Raman data. The Raman spectra were acquired when the Raman excitation light passed over two

angular sections, a) the section containing the Acetaminophen sample, and b) a section containing only the plastic tube through the set-up as illustrated in Figure 2.4b. It can be clearly seen in the obtained results (Figure 2.7a) that the presence of the Acetaminophen sample could be detected (at a wavenumber of 1645.8 cm^{-1}) in distinction from the plastic tube material. In order to further investigate the detection performance of the system, the mirror was rotated while 96 spectra were recorded with the Acetaminophen sample in a fixed position (refer to Figure 2.4b). The signal intensity at the specific wavenumber was recorded over the measurement of 96 spectra. It can be seen that the signal intensity dramatically rose approximately every 6 s (as a result of 1.5-s switching time for the motor actuation), which coincides with the timing that the rotating Raman laser passed over the Acetaminophen sample. The other five data points obtained in one rotation are the intensities at 1645.8 cm^{-1} mainly from the plastic tube only. It can also be seen in Figure 2.7b, that the intensity of the Acetaminophen sample displays a wave-like profile. This is most likely because the onset of Raman data acquisition (with a 1-s exposure time) was not in phase with the time that the laser reached the Acetaminophen sample in every rotation, and hence the signal intensity varied in a consistent pattern depending on how much Raman signal was acquired from the Acetaminophen sample during the mirror stopping time over the sample. Despite the fact that Raman data acquisition was not synchronized with the rotation of the mirror, the obtained result confirms that the rotation of the mirror was stable enough to be used for the target application for angle-resolved side-viewing spectroscopy. The observed intensity variation is expected to be effectively minimized via improvement of the set-up so as to trigger Raman acquisition upon the actuation switching signal for motor operation.

For the Raman measurements with *ex-vivo* tissue samples, their positions on the cylinder fixture (refer to Figure 2.4c) were first aligned with the four stopping angles of the rotating mirror

in order to increase the sampling time and hence signal level during the measurements. The motor was driven with a 2-s switching time (i.e., 7.5 rpm) and Raman signals were acquired through 5 rotations of the mirror. The laser beam reflected from the mirror was first aligned with a hole where there was no sample tissue, and this angle was defined as 0° . The samples of tumor and healthy tissues were placed around the plastic fixture at the angles of 90° and 180° , respectively. The Raman signals were effectively collected with intensities sufficient for data processing from each of the three locations via rotating device. As can be seen in Figure 2.8, the acquired spectra from both healthy and tumor tissues consisted of a series of Raman peaks with somewhat varying amplitude ratios between them. Moreover, the Raman shift values of these spectrum peaks from normal tissue were consistent with those previously reported for normal murine skin [97].

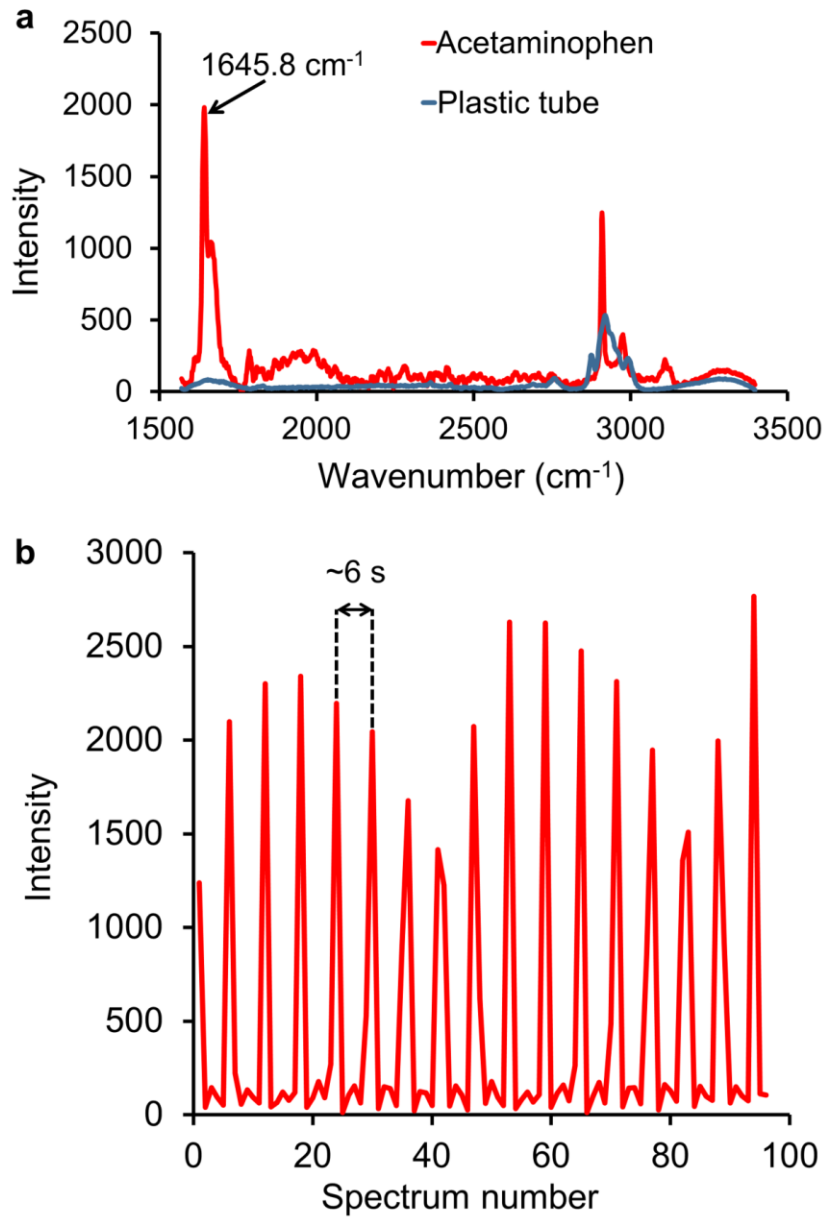


Figure 2.7: Raman test using the chemical sample: a) Raman signals collected with the device showing the spectrum from acetaminophen placed over the plastic (acrylic) tube and that from the tube itself. b) Corresponding Raman signals at the wavenumber of 1645.8 cm⁻¹ (acquired over 96 spectra) showing strong peaks upon passage of rotating laser over the location of acetaminophen.

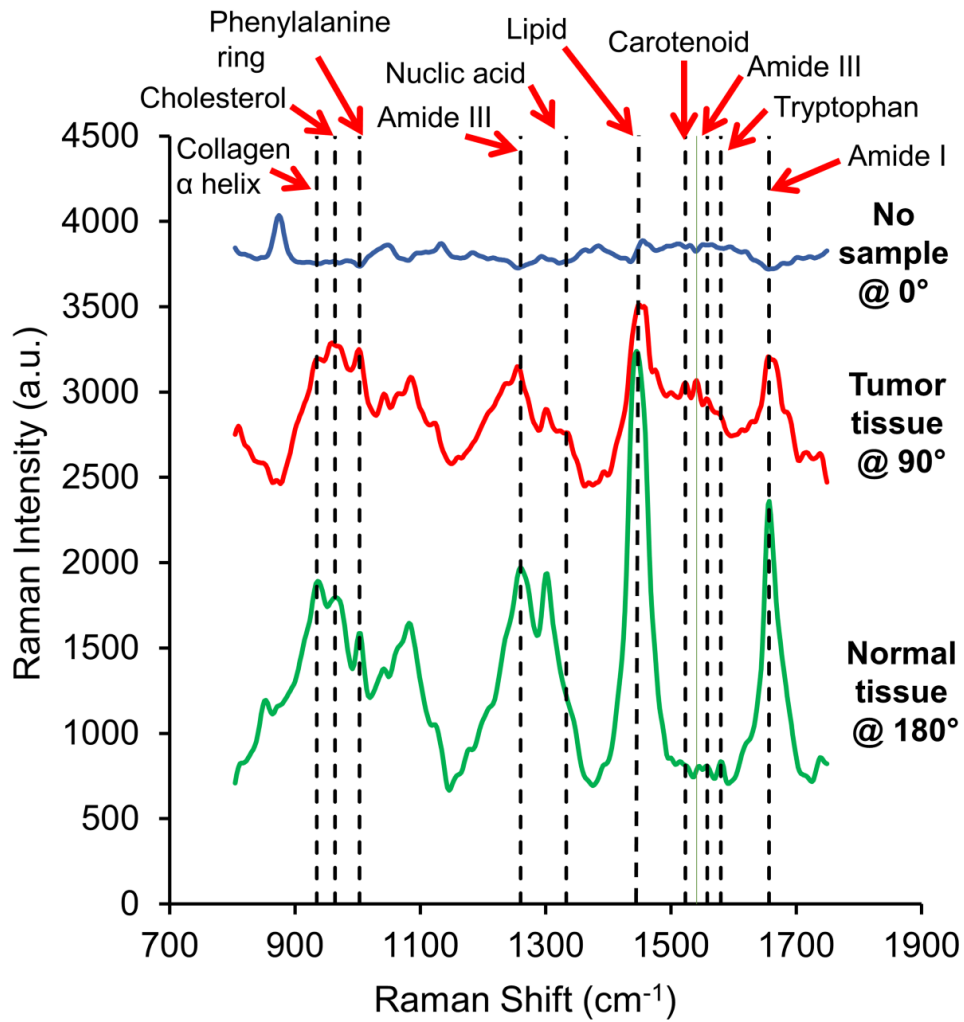


Figure 2.8: Ex-vivo test results. The Raman spectra were acquired at the three stopping angles without tissue sample (at 0°) showing the noise floor, with tumor tissue (at 90°), and with normal tissue (at 270°) (the spectra shifted on the intensity scale for clarity).

Chapter 3: A stepping micromotor based on ferrofluid bearing for side-viewing microendoscope applications*

3.1 Introduction

In this chapter, Device II is designed and developed to target at enabling side-viewing microendoscopes designed for the Raman spectroscopic modality. This is because Device I is not small enough (OD = 6 mm) to use for endoscopic in-vivo tests. Therefore, The present study targets at advancing the ferrofluid-based micro rotary motor technology, toward its application to side-viewing endoscopic catheter devices with an emphasis on the RS modality. This effort focuses on two major aspects of the device. First, the design of the micromotor is configured to raise its electromagnetic actuation performance in continuous rotation including angular rate per driving current and low-temperature operation. This design includes the stator tube with significantly smaller wall thickness (250 μm) that is revealed to be a highly effective path to achieving the above both theoretically and experimentally. The second focus is placed on the new control method for the stepping actuation of the micromotor. The angular resolution enhancement is an important step towards the application to RS catheter. This is because the RS modality requires a stepping or low-speed motion, instead of continuous high-speed rotation like the OCT case in [26], to properly collect reflected response from the specific part of the tissue (otherwise it only shows the averaged results of different parts of the tissue with lower resolution). This in turn means that finer stepping

*Part of this chapter appeared in the following publication:

S.M.H. Jayhooni, B. Assadsangabi, K. Takahata, "A stepping micromotor based on ferrofluid bearing for side-viewing microendoscope applications", *Sensors and Actuators A: Physical*, Volume 269, 2018, Pages. 258-268 (Published).

motion of the probing beam will enable RS mapping with higher resolutions. This goal is approached and demonstrated by a driving method that controls the amount and direction of the currents fed to the stator coils, without physically changing of stator coil arrangement on its tube substrate, so that arbitrary fine stepping can be achieved in a precise and efficient manner.

3.2 Principle and design

The rotor of the developed micromotor is comprised of two different permanent magnets with cubic and circular shapes, a micro prism mirror, and a linkage shaft that connects the mirror with these magnets. This rotor component is enclosed in the stator tube as illustrated in Figure 3.1a. This tube is made of polymeric material, with ID and OD of 2.1 mm and 2.6 mm, respectively. The cubic magnet has a side length of 1.0 mm and is magnetized along the radial direction of the catheter device. The stator coils are arranged on the tube substrate to create electromagnetic fields inside the tube and cause the cubic magnet to rotate. The circular magnet is linked with the cubic magnet mechanically using the linkage shaft with the diameter of 500 μm . This magnet has a ring shape with a 1.0-mm thickness, 1.8-mm OD, and 500- μm ID, that is magnetized along the axial direction of the catheter. The use of the circular magnet in the rotor assembly is to provide the radial stability of the rotor's motion. Thin layers of ferrofluid formed between the outer walls of the two types of the magnets and the inner walls of the stator tube serve as the self-sustained bearings as described earlier. The resultant thicknesses of the ferrofluid layers on the cubic and circuit magnets are approximately 350-550 μm and 150 μm , respectively. To enable circumferential scan of the laser beam provided from a RS probe, a 45°-angled prism mirror with the size of 1.0 mm is attached at the tip of the linkage shaft (Figure 3.1a).

The tubular stator component is comprised of two meander-type coils established on the tube

substrate. This component is created by first printing the two coils on thin flexible polymer film, each on a different side of the film aligned from each other, and then wrapping and bonding it around the substrate tube. Figure 3.2 shows the schematic of the stator tube with the coil circuit prior to the wrapping step. The aligned coils are designed to have four magnetic poles with 90° phase difference around the tube when passing the driving currents through them in the opposite directions. Activating the coils in an alternating manner electromagnetically drives the rotor with a 90° step as defined by the above poles. This operation, illustrated in Figure 3.1b, is referred to as the single-coil mode that allows four steps per rotation in the design discussed above. The stator circuit is connected to the current timing module to control the direction and amount of driving current passing through the two coils in different time sequence (Figure 3.2).

The substrate thickness of the stator circuit is an important parameter that directly impacts on the actuation performance of the motor, i.e., the closer the stator coils to the magnet rotor, the higher the magnetic field provided to the rotor to drive its rotation. The radial stator-rotor distance is largely determined by the thickness of the substrate tube, which was glass tube with a wall thickness of ~1 mm in the previously reported device [91], [94]. Polyimide (PI) is a thermoset plastic with high chemical resistance, high tensile strength, and biocompatibility, and its tube materials are widely available at low cost and are easily machinable. Due to these favorable characteristics, PI tubes have been used for a variety of medical/surgical applications including medical imaging [98]–[100]. This study adopts the PI tube noted earlier with a 4× smaller wall thickness (~250 μm) to increase the electromagnetic field inside the tube and around the rotor, consequently augmenting the electromagnetic driving force. For the same ID, the use of the PI tube also contributes to decreasing the OD of the micromotor by 35% [94].

To drive the stator coils, a microcontroller is used to program the timings, the directions, and

the amount of current so that the rotor makes full rotational motions. As discussed earlier, it is important to increase the number of steps or the resolution in the rotational motion. However, because of areal limitation on the outer surfaces of microendoscopic catheters, physically increasing the number of stator coils is not a practical approach to the need. To circumvent this issue, this study incorporates the microstepping method [101] for the developed micromotor control, to enable precision intermediate stops between two adjacent coil lines, via programmed distribution of driving currents to stator coils, while keeping the original four coil lines on the stator tube. The current amount control is implemented by the pulse width modulation (PWM) [101], [102] in this study. The synchronized control of the currents to two stator coils via PWM is expected to allow fine stepping of the rotor, with an angular resolution determined by the resolutions in the current amount and frequency in theory [101]. This operation scheme is defined as the dual-coil mode (Figure 3.1c). In this mode of operation, the angular position of the rotor is defined by the balance of the electromagnetic fields generated by the two adjacent coil lines, in which the field intensities are proportional to the amount of the driving currents fed to these lines. Thus, the exact stop position of the rotor between the two coil lines can be controlled by changing the amounts of the currents (i.e., by modulating the duty cycles in PWM) flown in these lines, allowing arbitrary stepping motions. Figure 3.1c shows an example when the current amounts are equal (by setting the duty cycles on the two lines to be symmetric, i.e., 50%), leading the equilibrium rotor position at the middle (45°) of the two lines. By switching the current directions with the logic illustrated in Figure 3.3 and Figure 3.4, this particular setting produces the 8-step rotation. The rotor position between the two lines shifts when the current on one line is increased/decreased relative to that on the other line (Figure 3.1c), which is implemented by setting the duty cycle on the two lines to be asymmetric (e.g., the rotor shifts away from the line with a

larger current amount or a higher duty cycle). The codes to control the current distribution are developed and applied to the microcontroller to achieve arbitrary step numbers. This first effort experiments two cases, i.e., 8 steps and 16 steps per rotation as will be discussed.

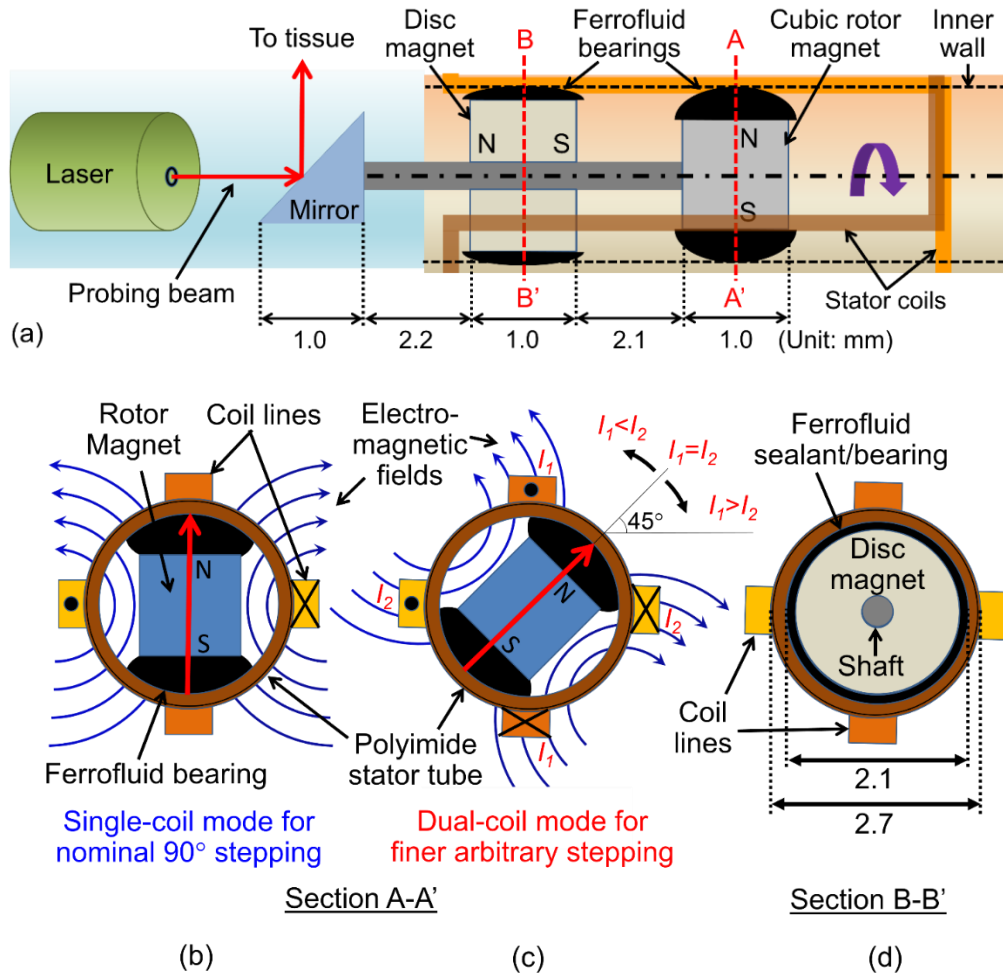


Figure 3.1: Design of the ferrofluid-assisted micromotor device for circumferential beam scan: a) Axial cross-sectional view; radial cross-sectional views at the cubic magnet rotor (A-A'), showing b) single-coil and c) dual-coil activation modes, and d) at the disc magnet (B-B').

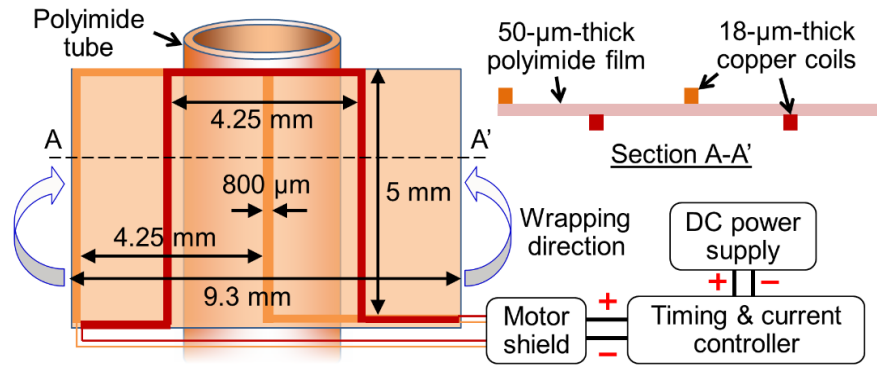


Figure 3.2: Stator circuit assembly and its connection to the driver module developed for the micromotor operation, stator tube is made of polyimide with thinner wall thickness (250 μm) in comparison with previous design (thickness = 1mm).

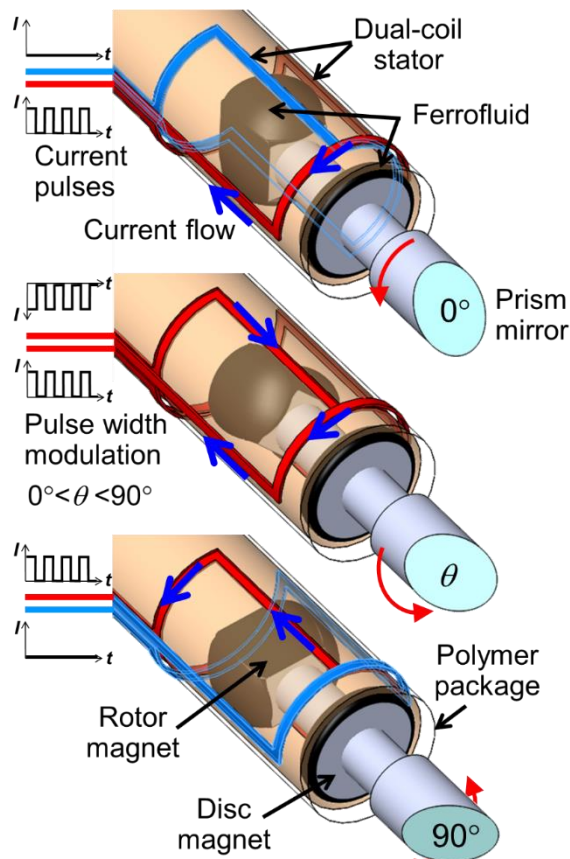


Figure 3.3: The schematic overview of the micro rotary stepping actuator custom developed for the side-viewing endoscopic RS device, showing stepping rotation of the prism mirror coupled with the actuator's rotor.

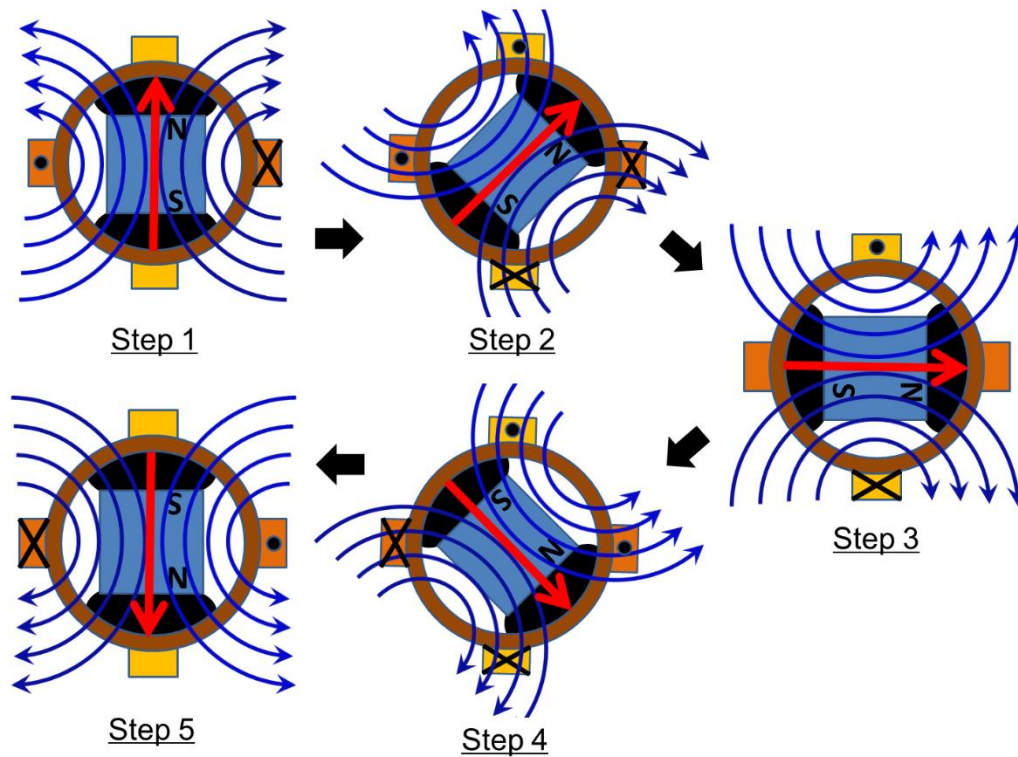


Figure 3.4: Activation logic of 8-step clockwise rotation of the developed micromotor with the directions of driving currents in the stator coil lines used (the figure only shows a half of the full rotation).

3.3 Finite element analysis of tubular stator

FEM method is used to analyze the electromagnetic fields created with the tubular stator and also to evaluate the effect of varying design parameters on rotor's behavior. The electromagnetic field around a current-carrying lead follows the Ampere's law as $B = \mu_0 I / (2\pi r)$, where B , I , r and μ_0 are the magnetic flux density, the current, the distance from the wire, and the permeability, respectively. Assuming a relatively long lead (i.e., the pattern of B is uniform along the lead), 2-dimensional (2D) models of the stator's cross section are created to evaluate the field distribution within the rotor space. These models define, same as the actual stator design, four copper lines (18- μm thickness and 800- μm width) arranged with a 90° spacing on the outer surface of the PI

tube with a fixed ID of 2.1 mm. The single-coil mode operation (current flows through one coil, i.e., a pair of two opposing lines at a time) is assumed for simplicity in this analysis.

Using the above model, the effect of the stator tube's wall thickness on the fields provided to the rotor space is first evaluated by varying the wall thickness (from 100 μm to 1.45 mm). For this, the 2D map of simulated fields with a given wall thickness is probed at the central (pole) location of the rotor (cubic magnet) surface when positioned right below an active lead, which is 550 μm away from the inner surface of the stator tube assuming that the rotor is radially centered in the tube from its design. Figure 3.5 plots the magnetic flux density at an inward radial distance of 550 μm from the tube's inner wall (or an outward distance of 1.0 mm from the radial center of the tube) beneath an active lead location as a function of the wall thicknesses. The active lead is assumed to carry a current of 1.0 A. The result shows a consistent decreasing trend with wall thickness as anticipated. In particular, the comparison between the flux densities with the two wall thicknesses, 250 μm and 1000 μm , corresponding to the PI tube in the current device (Device II) and the glass tube in Device I, respectively, suggests that the former case provides ~57 % field enhancement in comparison with the latter case.

Next, the effects of the width of stator leads on the field distribution in the rotor space are assessed using the previous 2D model and operation mode with a fixed wall thickness of 250 μm . For this analysis, three different lead widths, i.e., 200 μm , 800 μm (the value adopted in the design), and 2000 μm , are selected to simulate the magnetic flux densities (with the same 1.0 A driving current). The obtained cross-sectional maps of the flux density for these three cases are displayed in Figure 3.6a-Figure 3.6c. Figure 3.6d and Figure 3.6e plot the simulated results along the radial direction (crossing the two active leads) and those along the circumferential path 550 μm away from the inner tube surface (where the poles on the cubic magnet surface passes when

the rotor revolves), respectively. The results illustrate that there is no significant difference in the flux density between the cases of 800 μm and 200 μm , unlike the 2000- μm case. For example, at the center location of cubic magnet surface, the difference of the flux densities between the 800- μm and 200- μm cases is only 3.65% at a maximum. In contrast, the former case provides a significant merit in lowering the current density per cross-sectional area and thus suppressing Joule heating for a given stator current. The lead width adopted in the stator design originates in these factors.

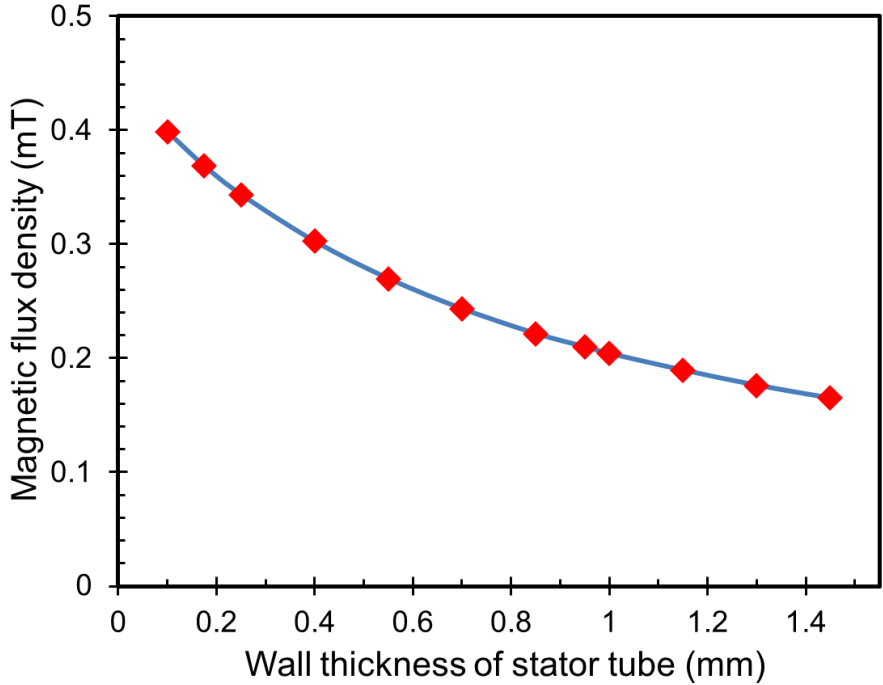


Figure 3.5: The magnetic flux density at the location of rotor’s surface beneath the stator carrying 1.0-A current as a function of the wall thickness of the stator tube.

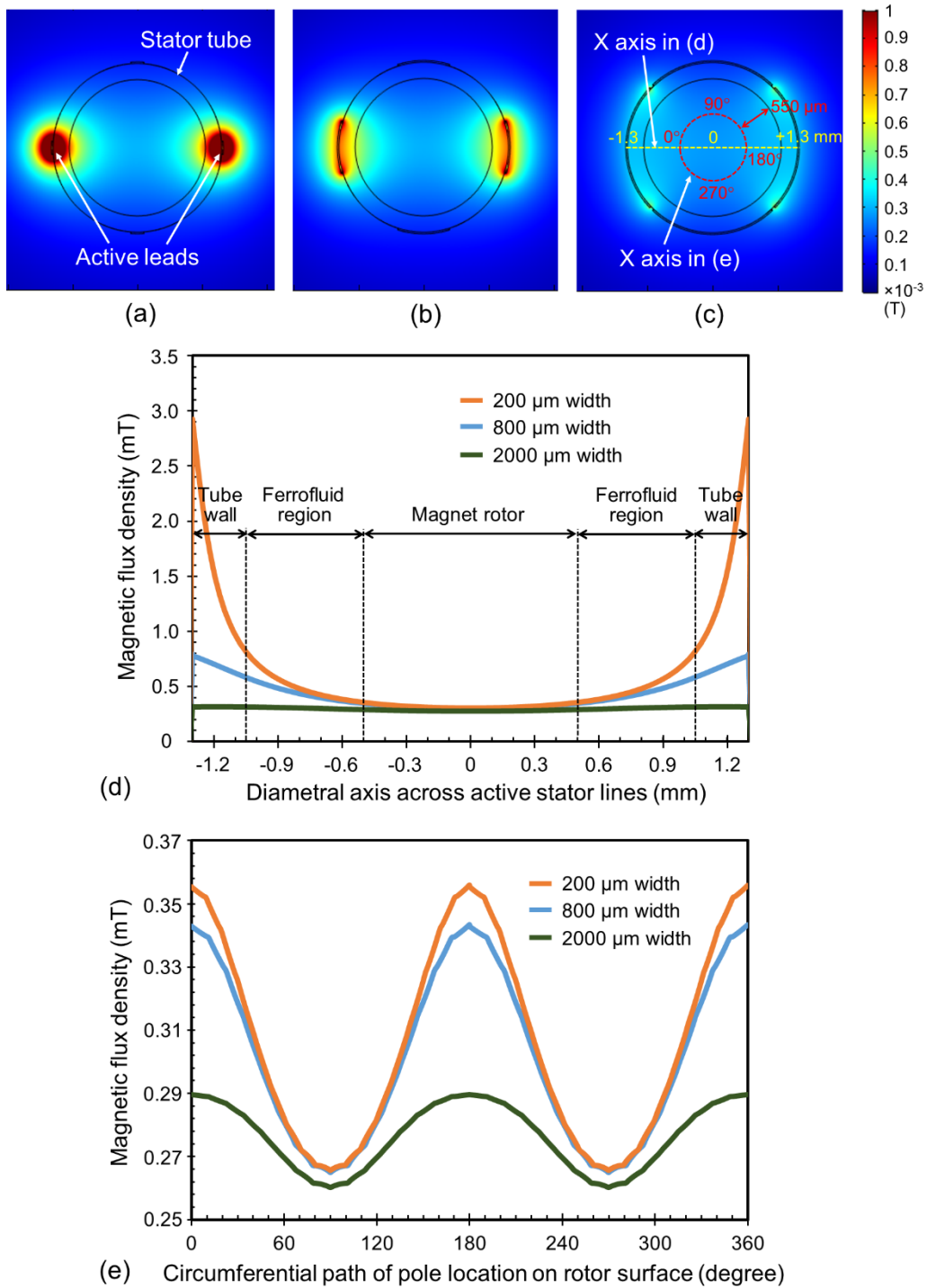


Figure 3.6: The distributions of magnetic flux density along a radial cross section of stator tube for three stator lead widths a) 200 μm, b) 800 μm, and c) 2000 μm with 1.0-A current, and resultant flux densities along d) the diametral axis bridging the two active leads and e) the circumferential path at 550-μm inward from the tube's inside wall for the three lead widths.

3.4 Prototyping

The fabrication of the stator circuit is performed through the photolithographic process explained for Device I. The fabricated stator-circuit film is wrapped and bonded around medical-grade PI tube (830-VIII, Microlumen Inc., Olsmar, FL, USA; with the ID and OD described earlier) using an adhesive (LePage[®] Gel Control Super Glue, Henkel Co., ON, Canada). For the rotor assembly, a 500- μm -diameter stainless-steel shaft cut using a laser micromachining system (A Series Compact Laser Micromachining System, Oxford Lasers Inc., MA, USA). The cubic and circular NdFeB magnets (Grade N52 with Zing coating, Ningbo Xinfeng Magnet Industry Co., China) are respectively bonded on one end of the shaft and threaded by the shaft with a tight fit while precisely aligning these components together using a motorized micromanipulator (SM 3.25, Märzhäuser Wetzlar GMBH & Co., Germany). Next, the similar 45°-angled, 1-mm prism mirror used for Device I is aligned and bonded to the other end of the shaft to complete the rotor component (Figure 3.7). Similar to Device I, prior to assembling it with the stator tube, a controlled amount of the oil-based ferrofluid is carefully applied onto each of the two magnets so that the gap between the magnets and the tube's inner walls are filled with the fluid when assembled together. It is worth noting that when the ferrofluid applied, for the cubic permanent magnet, the ferrofluid equally accumulates on the north- and south-pole sides of the magnet surfaces, whereas for the circular magnet, the fluid covers its cylindrical surfaces uniformly due to their magnetized orientations as illustrated in Figure 3.1. The ferrofluid layer that fills the clearance between the circular magnet and the tube's inner wall can serve as a sealant that prevents external medium from entering the inner space of the micromotor. The ferrofluid used in this study was observed to be stable in the completed device for a long term. For instance, the fabricated micromotor did not exhibit significant change in its operation for over two months since the completion of assembly.

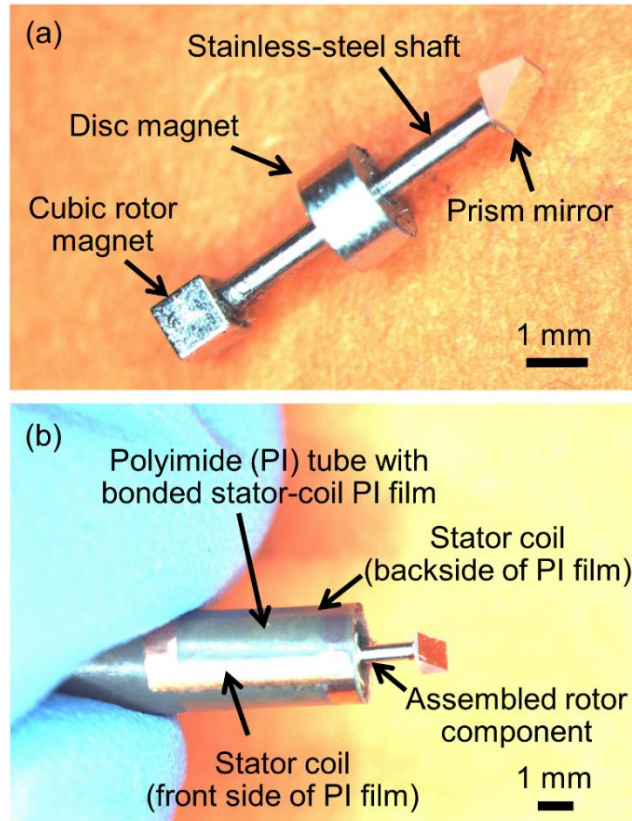


Figure 3.7: Fabricated samples of a) the rotor component with the prism mirror and b) the completed prototype.

3.5 Experimental results and discussions

3.5.1 Single-coil mode operation

The fabricated prototype was first operated in the single-coil mode to characterize the relationship between the rotational speed and the driving current in the mode. To experimentally find the effect of stator substrate thickness on this relationship, another micromotor with 1.0-mm wall thickness (of glass) equivalent to the previously reported device [94] was prepared and tested for comparison. To evaluate the rotor's angular motions, the micromotor was held horizontally, and a small 360° protractor sheet was secured around the micromotor so that the motor positioned exactly at the center point of the protractor. The angular position of the rotor (whose tip was

attached with a tiny pointer instead of the prism mirror) was recorded and measured through a stereoscope aligned with the motor axis. A commercial microcontroller with motor controller (Uno R3 SMD and A000079 Motor Shield R3, Arduino, PA, USA) was used as the current timing module (Figure 3.2) for the stepping operation.

Figure 3.8 displays the measured results obtained under the rotational speeds ranging from 1 rpm to 600 rpm as a function of the driving current. By applying the currents to the stator coils and switching the currents from one coil to another with selected directions, the rotor initiated its revolving; however, there was a minimum level of current that provided an electromagnetic force large enough to maintain a specific rotational speed. This minimum current can depend on different factors such as rotational speeds, magnetic torque and friction force [91]. clearly illustrates that, as predicted from the simulation result from Section 3, the wall thickness of the stator tube has a significant influence on the rotational speed, indicating that the developed device exhibited approximately 4× higher speeds compared with the reported device [94] over a range of the driving currents tested. This also means that the developed device offers an advantage on the required current (or resultant power consumption) to sustain a certain rotational speed. In particular, the results show that the developed device provided a tested range of rotational speeds with up to ~54% smaller currents (or ~79% smaller power consumption) compared with the case of the Device I. It should be noted that both the scaling factor (~4×) of rotational speed and the reduction rate (~54%) of the required driving current are well consistent with the stator's substrate design that used 4× smaller tube wall thickness and the simulated rate (~57%) of the magnetic field enhancement enabled with the particular design, respectively.

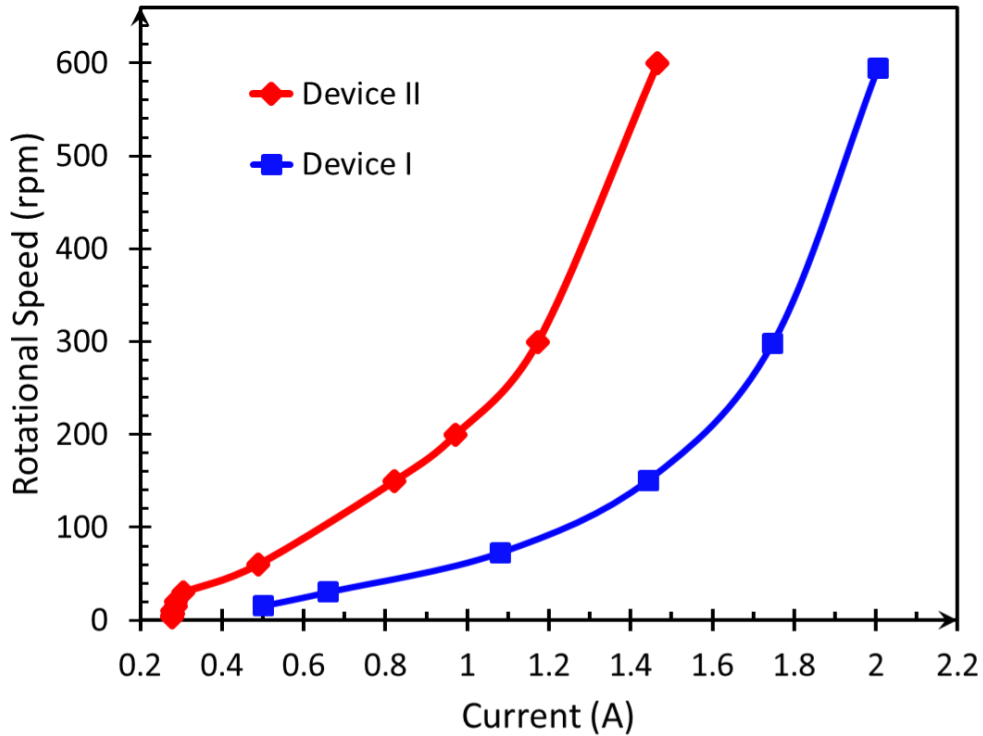


Figure 3.8: Rotational speed vs. driving current measured with Device II and Device I.

3.5.2 Thermal characterization

For electrically powered endoscopic catheters, their operating temperature raised by Joule heating effects is one of the important factors in light of biocompatibility of the catheters. This is especially true for those with micromotors, including the present device, that are electromagnetically driven. This is mainly because temperatures exceeding around 43 °C [103], [104] can damage surrounding tissue in contact with the device. In case of the operation within a blood vessel, it could lead to thrombus and occlusion. Although operating temperature of the developed device for a certain rotation speed is expected to be lower than the case of the previous device given the less power consumption in the current device as discussed with Figure 3.8, proper packaging may still be necessary to suppress temperature of the outmost surfaces of the motor-embedded catheter device so that it is within the safe threshold temperature. In addition, given that

the dual-coil mode essentially distributes the current of single-coil mode to two coils, the peak temperature developed in the single-coil mode represents the worst case of heating in the dual-coil mode. In light of these, the thermal behaviors of the developed micromotor were experimentally characterized under the single-coil operation mode. The measurement was conducted using the same two devices (operated with varying rotational speeds; the relationship between the rotational speed and the current is given in Figure 3.8 while recording temperature distribution on the active device using an infrared (IR) camera (VarioCam HiRes 1.2M, Jenoptik AG, Germany). It is important to note that temperature measurement with infrared signals significantly depends on the emissivity of the materials. Due to relatively low emissivity coefficients of metals, temperature readings on metals are not sufficiently reliable [95]. Hence, to acquire accurate temperature results with the IR camera, temperatures were read on the PI substrate, at a location in close proximity to a copper line of the coils (whose temperature should be close to that of the current-carrying copper line, the hottest location on the stator) in this measurement.

Figure 3.9 shows the maximum temperature increases from room temperature (26.4 °C) measured on the two types of the devices as a function of their rotational speeds (up to 600 rpm). The results clearly indicate the merit of the developed device compared with the counterpart in suppressing temperature increase when operated at identical rotational speeds. For example, at 300 rpm, the current device exhibited 40.7 °C, which is still lower than the threshold temperature, whereas the counterpart reached 51.6 °C exceeding the threshold. The temperature increments seen on the present device significantly decreased from those of the previous device, with approximate reduction rates from 24.8% (at ~600 rpm) up to 96.3% (at ~30 rpm) over the measured range of rotational speed. This is a significant outcome especially for the targeted RS application as its laser scanning will be implemented at low-speed rotations.

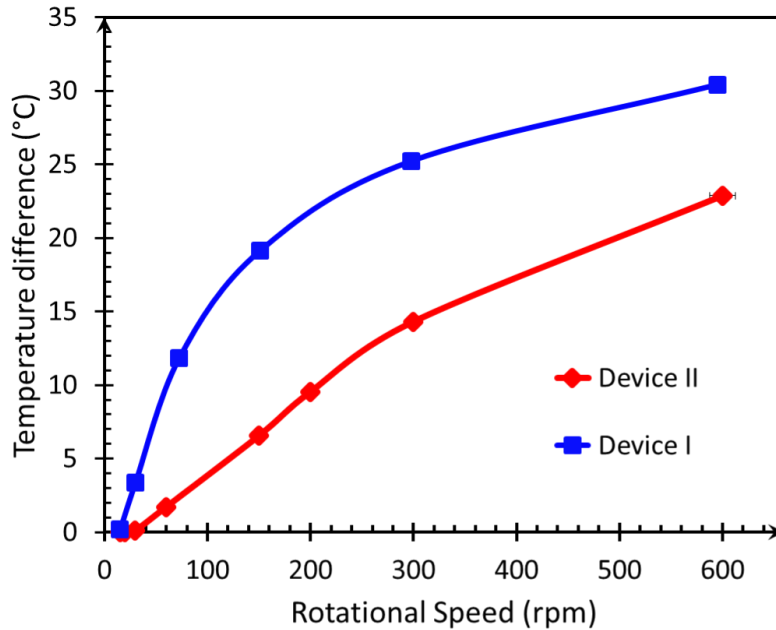


Figure 3.9: Temperature increase vs. rotational speed measured with Device II and Device I.

The measured maximum temperatures of the operating device is plotted as a function of the driving current in Figure 3.10a. The IR images of the device driven at three different currents, 0.8 A, 1.0 A, and 1.3 A, are also displayed in Figure 3.10b-Figure 3.10d. The plot in Figure 3.10a is shown with a fitted curve with quadratic dependence on the current that was found to represent the measured temperature trend well (this can also be seen from the fact that the room temperature suggested by the curve (as the intercept on the Y axis at $X = 0$ A) is 25.5 °C, which matches well with the actual room temperature of 26.4 °C). The fitted curve suggests that in order to limit the device temperature within the threshold level (i.e., ~43 °C), the driving current applied to the motor should not exceed 1.26 A. This allowable current level can be raised by having a packaging layer on the motor to serve as a thermal insulator (at a cost of increased outer diameter of the device).

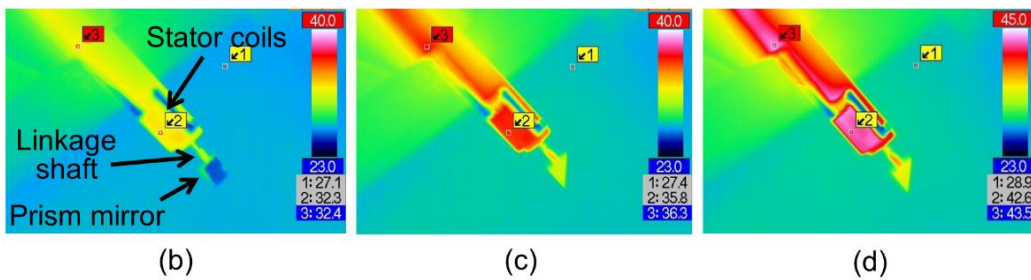
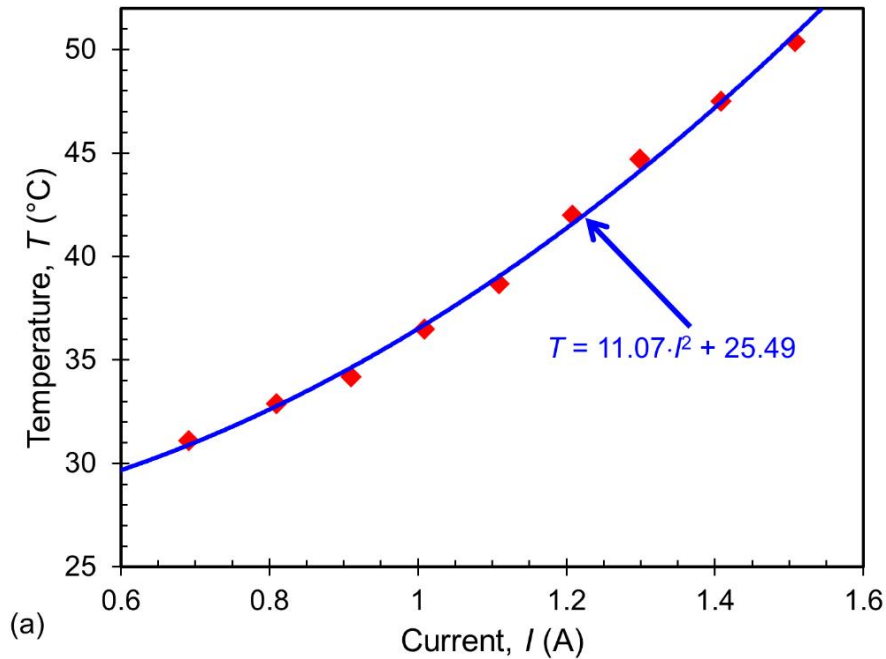


Figure 3.10: Characterization of operating temperature of the micromotor with varying driving current: a) Measured maximum temperature vs. current; IR images of the micromotor driven with the currents of b) 0.8 A, c) 1.0 A, and d) 1.3 A.

3.5.3 Dual-coil mode for fine stepping operation

The device operation using the dual-coil operation method was first tested for the 8-step sequence (Figure 3.4) that theoretically allowed 45° stepping by enabling an equilibrium state in the middle of each pair of adjacent stator lines. This operation test was performed by providing an identical current amount of 260 mA to each stator coil through the same current timing module used in the single-coil mode experiment while implemented with the PWM method in this test.

The duty cycle of PWM defined in each coil line was set to be 50% that was implemented with a PWM frequency of 490 Hz. The measurement results are shown in Figure 3.11 that plots the absolute angles measured at each step of one rotation along with the ideal angular trajectory. As can be seen, the stepping motion showed a good match with the theoretical case, with an average angular deviation of less than 2%.

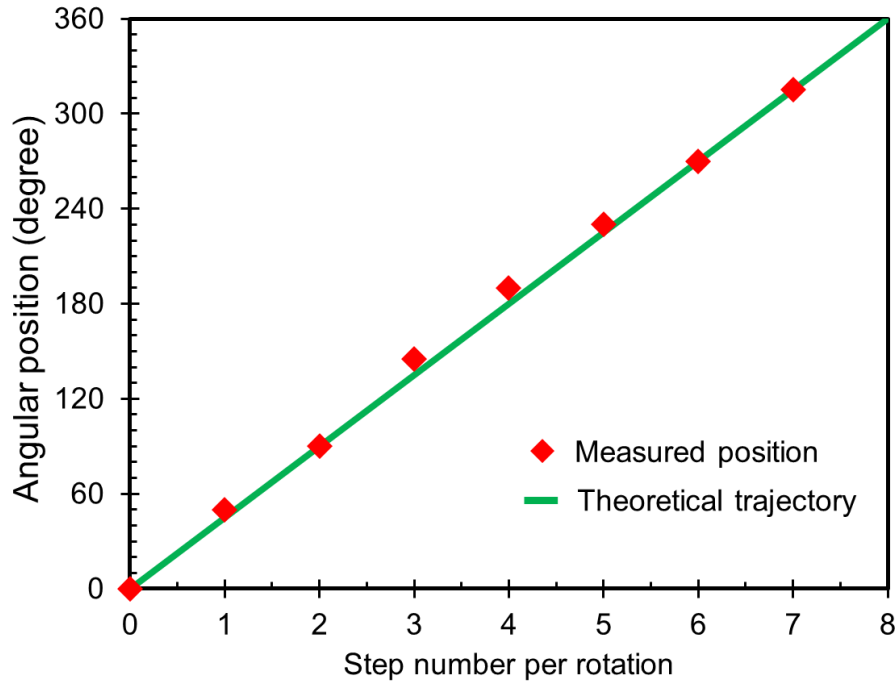


Figure 3.11: Angular positions measured with the dual-coil activation mode for 8-step rotation.

In the RS systems, the laser beams used in them exhibit varying divergence angles depending on different factors such as the laser type and the wavelength of the laser beam (e.g., 0.06° or less for an argon laser, and up to 30° for a diode laser [105]). The areal coverage of RS reading on tissue illuminated by a certain type of laser directly depends on its divergence angle. One of the most commonly used laser sources for RS is the diode laser [105]. Based on the divergence angle of the laser, the micromotor is expected to provide 12 or more steps per rotation, in order to cover the entire circumferential surface of the inner wall of a duct/vessel of the human body. In light of

this condition, a stepping number of 16 (22.5° step) was selected to evaluate the dual-coil mode further. For this stepping, the rotor needs to make two additional stops (22.5° and 67.5°) between two lines compared with the case of 8-step rotation (45°). The PWM duty cycles for positioning at these two angles were calculated to be 29.3% and 70.7% (i.e., when one line is with the 29.3% duty cycle of and the other with 70.7%, the rotor positions at 22.5° from the former line, whereas the rotor positions at 67.5° when the duty cycles are switched between the two lines). The measured angular positions tracked with the 16-step rotation is displayed in Figure 3.12. Compared with the 8-step case, the deviation from the theoretical trajectory was slightly increased (average $\sim 6\%$). Given the single angular step to be less than 30° , this level of tolerance still allows one to capture RS data from the entire circumferential inner surface using a diode-laser-based RS system.

There are multiple potential sources that could lead to the observed errors. In device fabrication, bonding the stator-coil film around the tube using adhesive can cause coils' positional errors (due to, e.g., a misalignment with respect to the tube axis, a non-uniform adhesive layer, and an error between the length of the film and the outer circumference of the tube on which the film was bonded), which calls for further optimization of the assembly process. On the control side, the error in the actual amount of current through the stator's lines with the specific control set-up used (observed to be $\sim 2\%$) can also be a contributor. Regarding the measurement, the data collected with the particular angular reading set-up used in the tests may have errors up to $\sim 1.4\%$; to address this type of issue, an image processing method may be applied to quantify rotational movements of the micromotor with higher accuracy. Nevertheless, the outcomes observed in the 8- and 16-stepping tests of the developed micromotor indicate that its dual-coil mode operation based on PWM is indeed effective to enable angular control of the actuation with finer stepping resolutions, overcoming the limitation in the physical arrangement of many stator coils that could

be accommodated on the micromotor.

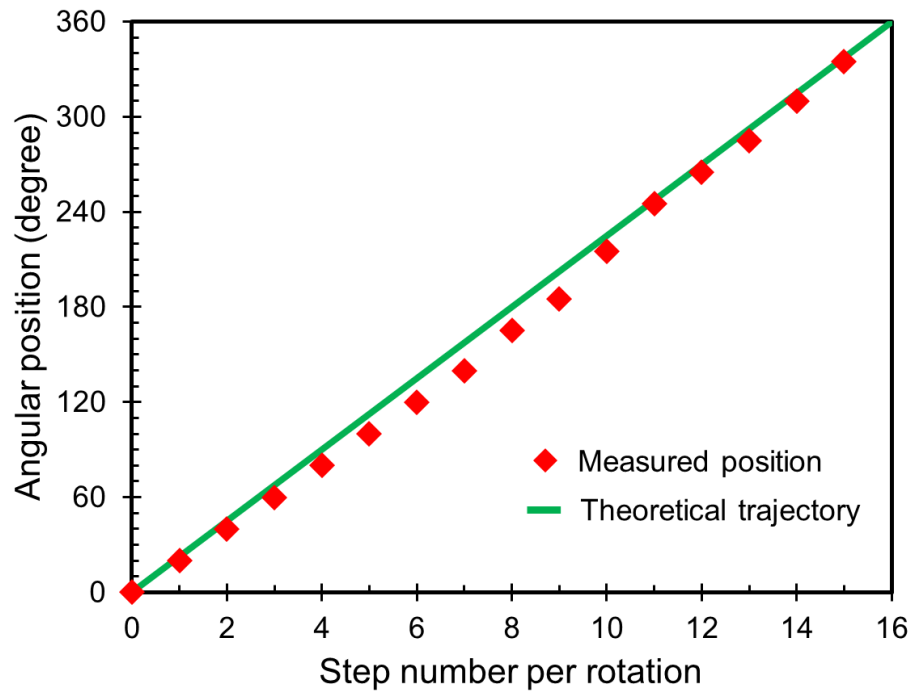


Figure 3.12: Angular positions measured with the dual-coil activation mode for 16-step rotation.

Chapter 4: Side-viewing endoscopic Raman spectroscopy for angle-resolved analysis of luminal organs*

4.1 Introduction

In this chapter, the first MEMS-enabled side-viewing endoscopic RS device that achieves real-time, angle-resolved Raman tissue analysis within narrow conduits is presented. This part of the thesis is particularly intended for the application of detecting peripheral lung cancers grown on the sidewalls of narrow bronchi (Figure 4.1). The performance of the integrated side-viewing endoscopic Raman device prototype using test chemicals is shown and its targeted function for circumferentially localized RS analysis and detection with high accuracy will be verified. In this chapter, for the first time, *ex-vivo* test using harvested bovine lung is performed and due to the promising *ex-vivo* results, we further evaluate and demonstrate *in-situ* RS analysis using rat colon as well as *in-vivo* human skin measurements while showing a high reliability of RS data that are acquired through the device via comparisons with reported reference data obtained using common forward-viewing probes. Device II, superior to Device I in terms of the size, rotational speed and maximum temperature (Chapter 3), is integrated with a RS catheter. Also, it has the potential to scan conduits more precisely due to enabling Device II with micro stepping controller. Hence, the tubular micro rotary stepping actuator, custom-designed with a ferrofluid levitation mechanism, is

*Part of this chapter appeared in the following publications:

1. S.M.H. Jayhooni, M. Short, B. Assadsangabi, G. Hohert, C. Du, H. Zeng, K. Takahata, "Side-view Raman microendoscopy for angle-resolved screening of intraluminal cancers", *Advanced Materials Technologies*, 2019, 1900364 (9pp) (Published).

2. S.M.H. Jayhooni, M. Short, B. Assadsangabi, H. Zeng, K. Takahata, "Side-view Raman microendoscope with Micro stepping motor and its ex-vivo test for real-time cancer detection.", *IEEE MEMS conference 2019*, Seoul, South Korea, Pages. 14-17 (oral presentation, outstanding paper finalist).

integrated with a Raman probe, for the first time, to scan a probing laser beam sideways for angle-resolved Raman excitation and signal collection with no aid of tissue labeling, towards enabling the detection of lesion-induced biochemical changes *in-vivo* and in real time. The results from all these tests can reveal the efficacy of the developed side-viewing device for tissue analysis through the RS modality and illustrate how collected signals are match with known RS characteristics of the tested samples and organs.

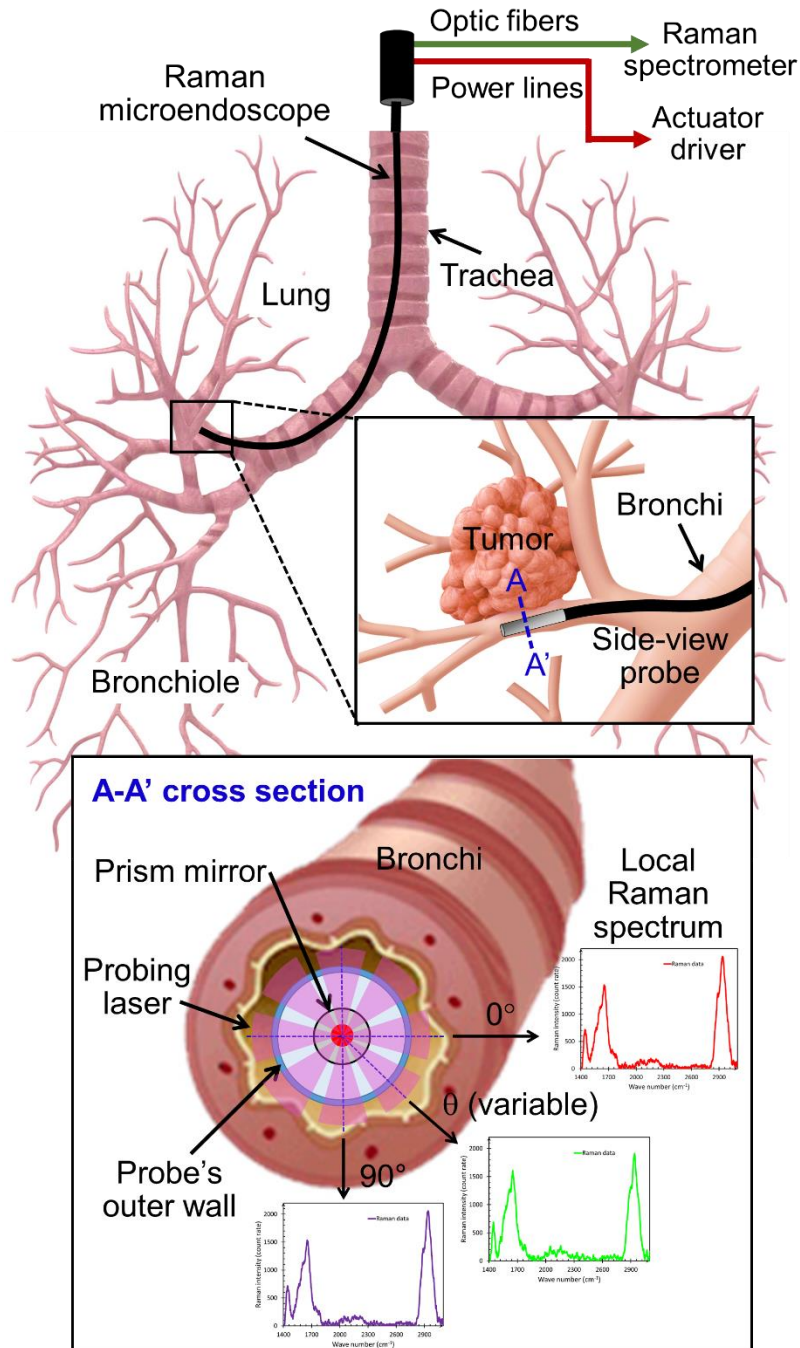


Figure 4.1: Conceptual schematics of the side-viewing Raman device developed with intended application in peripheral lung cancer detection. A probing laser beam emitted from the Raman probe is circumferentially scanned by rotating the prism mirror stepwise at controlled angles, to collect local spectroscopic data for real-time diagnosis within narrow bronchus.

4.2 Working principle and design

The stepping scan of probing laser, a key requirement for the side-viewing RS endoscopic device, is achieved using a custom-developed electromagnetic micro rotary actuator packaged with a Raman probe (Figure 4.2). This micro actuator design is similar to the Device II explained in Chapter 3 except the following changes: the main driving magnet is a permanent NdFeB magnet with a 1.3-mm cubic shape which is bigger than the 1.0-mm cubic shape magnet used in Device II in order to enhance the rotational stability of the actuator (Figure 4.2). A round-shaped, 45°-angled glass prism (1-mm OD and 2-mm length) coated with a thin aluminum film, used for laser beam bending and circumferential scanning with the actuator, is secured at the free end of the linkage shaft so that the angled mirror revolves together with the rotor. The circular cross section of the prism allows the mirror surface to effectively fill the inner cross section of the tube and consequently reflect more light to/from tissue. The forward-viewing RS probe introduced in Chapter 1 and the micro actuator are aligned and integrated together by inserting them into polymeric transparent tube (verified not to substantially distort relevant Raman spectra) that allows for bidirectional passage of the probing laser beam directed to and reflected by tissue circumferentially, while protecting the actuator-mirror component from the biological surrounding (Figure 4.3, Figure 4.4 and Figure 4.5). The same micro stepping controller used in Device II is exploited in this actuator to achieve arbitrary angular positioning of the rotor. We selected 45° stepping motion to conduct 8-step sequence per rotation. Depending on the user's need or the particular condition of the patient, angular positions can be easily changed via programming of the current driver, without the need for modifying the hardware such as the stator circuit design.

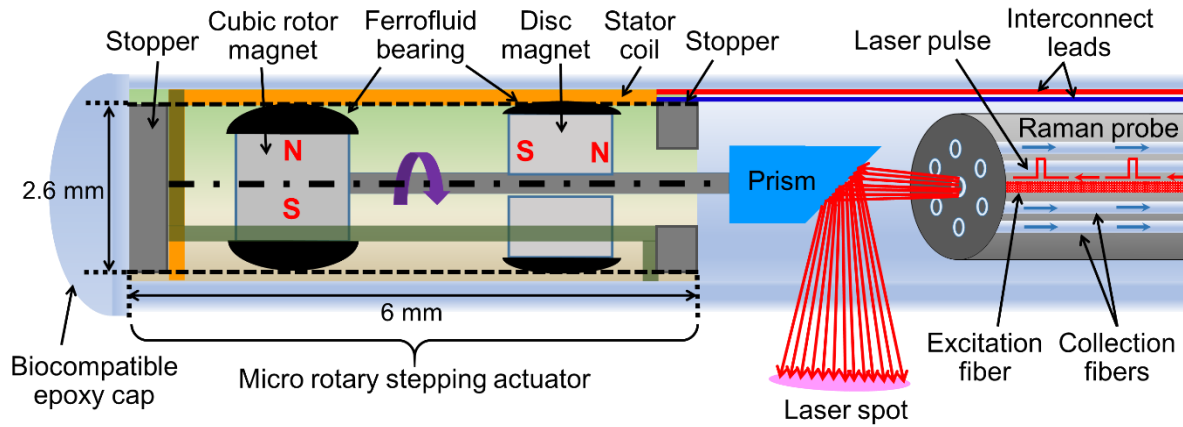


Figure 4.2: Schematic diagram of the construction of the side-view mechanism enabled with the micro rotary actuator integrated at the tip of a Raman probe. The rotor is electromagnetically driven with an aid of ferrofluid levitation mechanism.

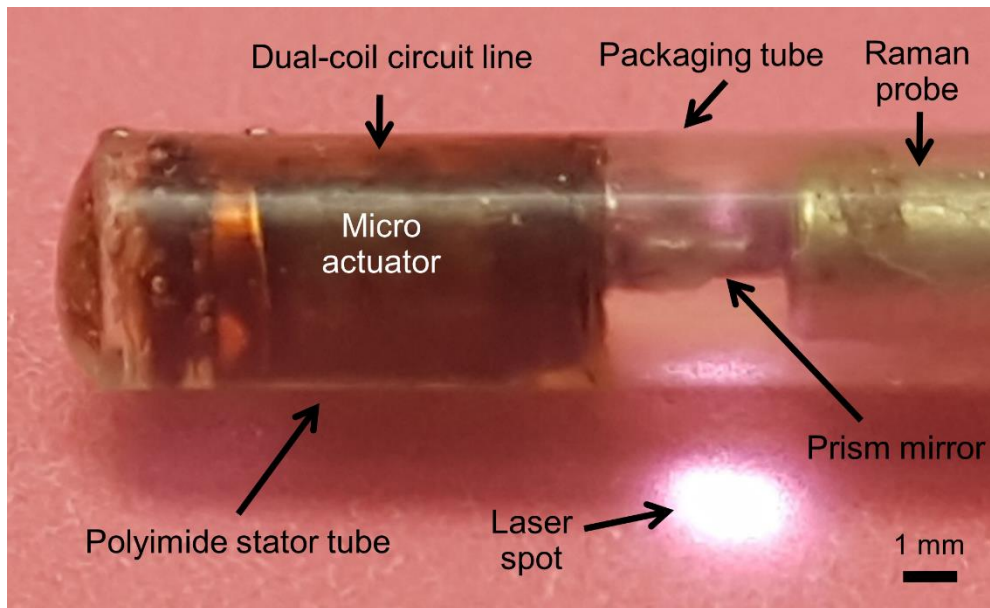


Figure 4.3: A prototype example of the integrated side-viewing RS device functionalized with custom-designed micro rotary stepping actuator and a prototype example.

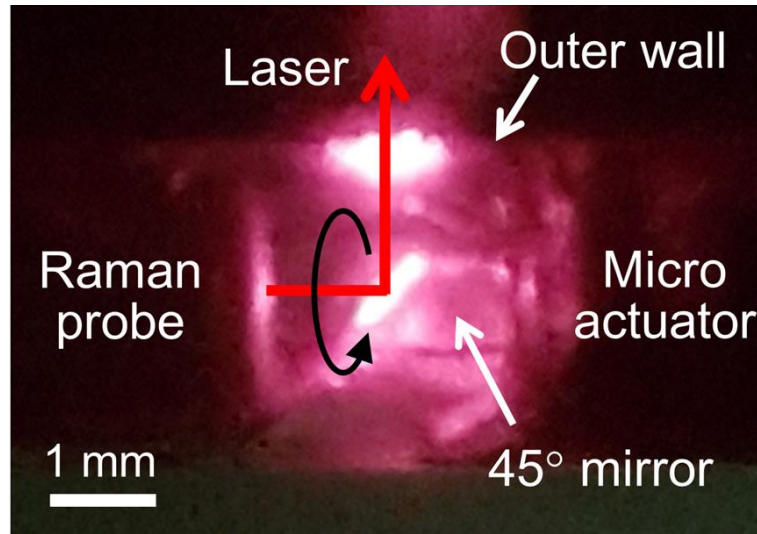


Figure 4.4: The circumferentially scanning a probing laser beam by the prism mirror of the integrated side-viewing RS device.

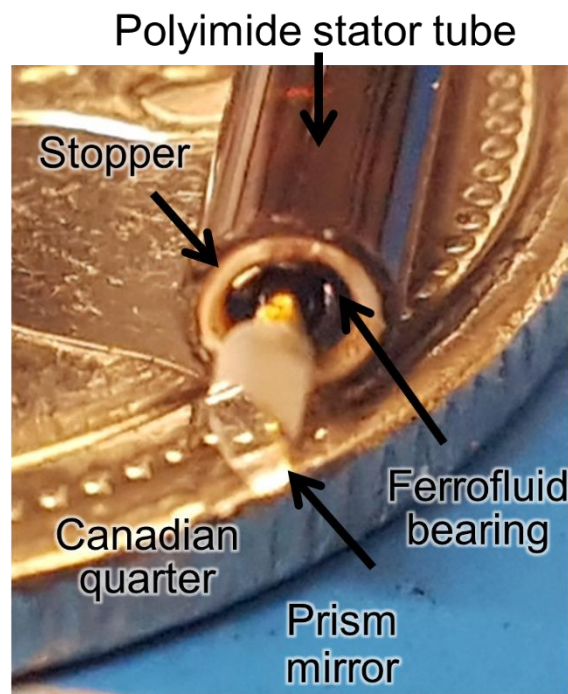


Figure 4.5: The pre-assembly stator tube with the rotor-mirror component showing the ferrofluid bearing inside.

4.3 Prototyping

The rotor component was constructed by mechanically coupling the cubic and ring magnets (N52 with Zinc coating, Ningbo Xinfeng Magnet Industry Co., China) together. The coupling was implemented by bonding one end of a 500- μm -diameter, 4-mm-long stainless-steel linkage shaft to the cubic magnet using a precision alignment set-up while the ring magnet was tightly threaded through it. The 45°-angled mirror prism (RDMR-1-A, Chuo Precision Industrial Co, Japan) was bonded to the other end of the linkage shaft using the same set-up. In addition to the stator circuit fabrication method explained in chapter 3, both sides of the stator circuit that holds the coils are coated with Parylene C, an FDA approved biocompatible polymer [106], for electrical and biological passivation purposes by using a commercial deposition system (Labcoter 2, Specialty Coating Systems, IN, USA). A commercially available oil-based ferrofluid (EFH1, Ferrotec Co., USA) was applied to each magnet with a controlled amount ($\sim 3.5 \mu\text{L}$ in total) using a micro syringe, and then the rotor component was inserted into the stator tube. The disc/ring-shaped stoppers were secured in the tube to limit the axial movement of the rotor (Figure 4.3). The disc stopper (2.15-mm OD and 500- μm thickness) was placed at the free end of the micro actuator, and the ring stopper (identical dimensions as the disc, with the 1.6-mm-ID through hole) was placed between the ring magnet and the prism mirror in which the linkage shaft passed through the ring's hole. The diameter of the stoppers was made to be 50 μm larger than the tube's ID so that they could be tightly fitted into the tube to secure their positions. These stoppers were fabricated with a 3D printer (Freeform Pico2, Asiga, USA) using an ABS-based photopolymer (PlasGRAY Version 2, Asiga, USA). The micro rotary actuator with the prism mirror and the tip portion of the Raman probe were precisely assembled together via their tight insertion into a biocompatible and transparent packaging tube. The gap clearance between the mirror and the probe tip was adjusted

to be ~1 mm.

Stability of the micro motor: In order to use the micro motor with RS probe, one of the key factors is aligning the prism attached with the tip of micro motor with the laser beam of the RS. This is because during the full rotational movement of the micro motor, the laser beam should reflect 90° to scan the tissues surrounding of the device. However, the experiments show that Device II has low stability during each stepwise rotational movement and aligning the Raman probe is not quite achievable. Therefore, the micro motor design is modified in the way that the size of cubic magnet as the main driven part increases from 1.00 mm to 1.3 mm and consequently the gap between its magnetic poles to stator inner wall decreases from 350-550 μm to 140-400 μm . The device was also fabricated and tested to obtain better alignment. Based on the configuration of the micro motor and the gap between the rotor and stator, the theoretical analysis show that if there is no ferrofluids in the gaps, the maximum wobbling of the prism is in orange circle of Figure 4.6 (with $2r$ diameter), the experimental measurements illustrate that all the data are in yellow circle which is completely located in the orange circle as a result of using ferrofluid in this device, thus the experiments and theory confirm each other. The area of the yellow circle that all experimental data are located in every step are called rotational area. The comparison between the modified design and the preceding one shows that the rotational area decreased by 79.32 %. In other words, the stability of the micro motor prism of the modified design is much higher than the preceding one.

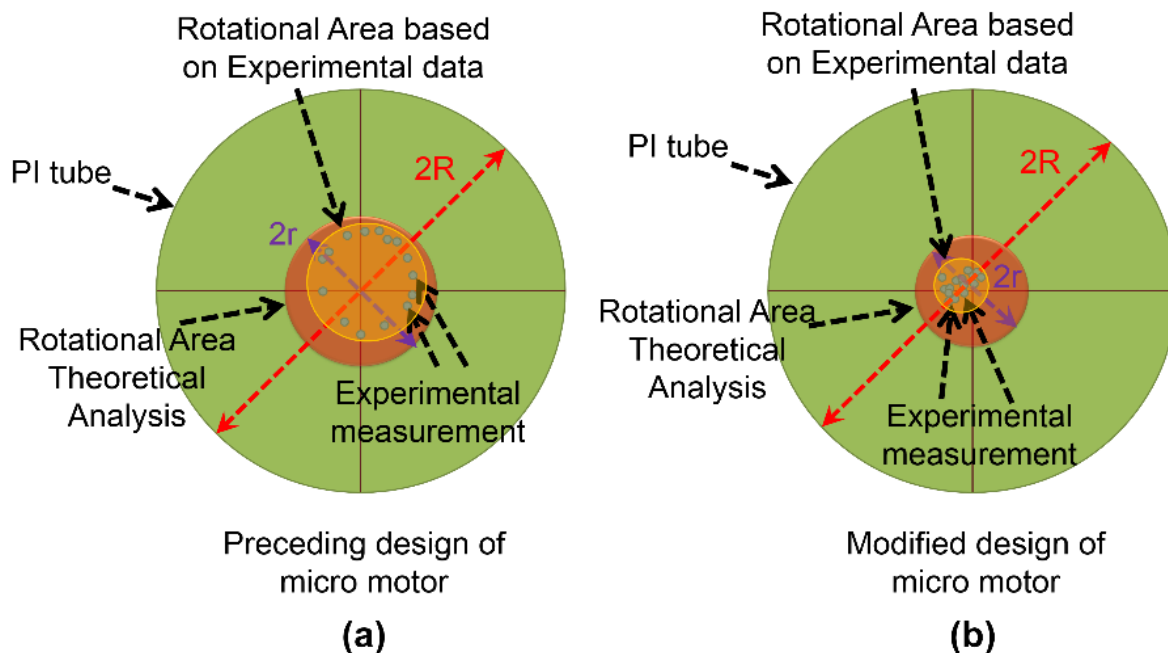


Figure 4.6: Micro motor cross section based on a) preceding design of Device II (1.0 mm cubic magnet) b) modified design of Device II (1.3 mm cubic magnet), green circle is the inside of the stator, orange circle (circle with $2r$ diameter) is the maximum areas that the middle of prism connecting to the shaft of the rotor can reach based on theoretical calculation, the experimental measurements are shown with blue dots and they are repeatedly located in the yellow circle.

4.4 Results and discussion

4.4.1 Chemical detection tests

A preliminary evaluation of the angle-resolved RS analysis through the prototyped side-viewing probe was conducted using test chemicals. For this purpose, type I acetaminophen which is commonly used as a benchmark sample for RS analysis is selected and the collected signals are compared with reported reference data [107], [108]. Another chemical, ibuprofen, was also used in conjunction with acetaminophen to assess the ability for detecting different substances that were present on the circumferential scan path. A hollow aluminum tube (6.5-mm ID and 1.5-mm wall

thickness) with 8 equally spaced slots arranged around the tubular walls was used as the test platform for this measurement (aluminum is known to exhibit low Raman background and to cause no substantial influence on sample's signals). Four acetaminophen samples were placed in every other slot and the rest of the slots were filled with ibuprofen (Figure 4.7a). After positioning the integrated probe inside the tube loaded with the above chemicals, the RS system was operated to perform stepping rotation of probing laser beam continuously while collecting data every one second. The collected raw data contains Raman signals superimposed on a fluorescence background. A special real-time method for fluorescence background removal based on a polynomial curve fitting approach [92] was used to obtain the pure Raman spectra.

The 8-step collection of signals from acetaminophen and ibuprofen was successfully conducted using the PWM control method under the dual-coil operation mode as described in section 3.2., and the two spectral signals processed as a function of wavenumber are shown in Figure 4.7b. It should be noted that in RS, the wavenumbers of Raman peaks and the pattern (shape) of the spectrum are more important characterization factors than the intensity of the peaks, as the former data are representative of specific chemicals/molecules and the latter can show whether the tissue of interest is normal/healthy or not, whereas the peak intensity depends on various external parameters (including the distance between the probe and a targeted tissue, Raman fiber characteristics, spectrometer specifications, and type of laser source and its power) with which the above two factors do not significantly change. The signals of acetaminophen are labeled with the wavenumber of major spectral peaks that characterize the chemical. These characteristic peaks were compared with those of the reported Raman signals that were obtained using a commercial Raman system [107]. This comparison indicates that the spectral shapes and peaks matched well with those of the reference data, with significantly small wavenumber deviations

($\leq 0.5\%$) for all the major peaks as shown in the graph. The only difference with the reference was the amplitude of the peaks, which is related to the difference in the set-up conditions including the distance between the probe and the chemical sample. The signals obtained from all ibuprofen samples also exhibited nearly identical spectral patterns and peak wavenumbers with the only difference in their intensities, similar to the case of acetaminophen. It has been reported that obtaining tissue signals in a high frequency range (from 1400 cm^{-1} to 3100 cm^{-1}) is effective for lung cancer detection with human *in vivo*, because this range provides clear and sufficient *in-vivo* lung Raman spectra that allow for characterizing lung tissue using RS *in vivo*, opening an avenue to improve early cancer detection [92]. (In contrast, raw tissue data in a finger-print/low-frequency range is dominated by a fluorescence emission, which makes it difficult to discern Raman peaks in the raw data, and this adverse effect is more significant in lung tissue due to having strong autofluorescence and thus extracting of Raman signals in this region is unreliable [92].) The above results suggest that the developed endoscopic Raman device offered the designed side-view capability that could distinguish samples with different chemical compositions, present at different angular positions within a conduit, and that it provided accurate Raman data, with a distortion level that was almost negligible, for a frequency range relevant to cancer detection.

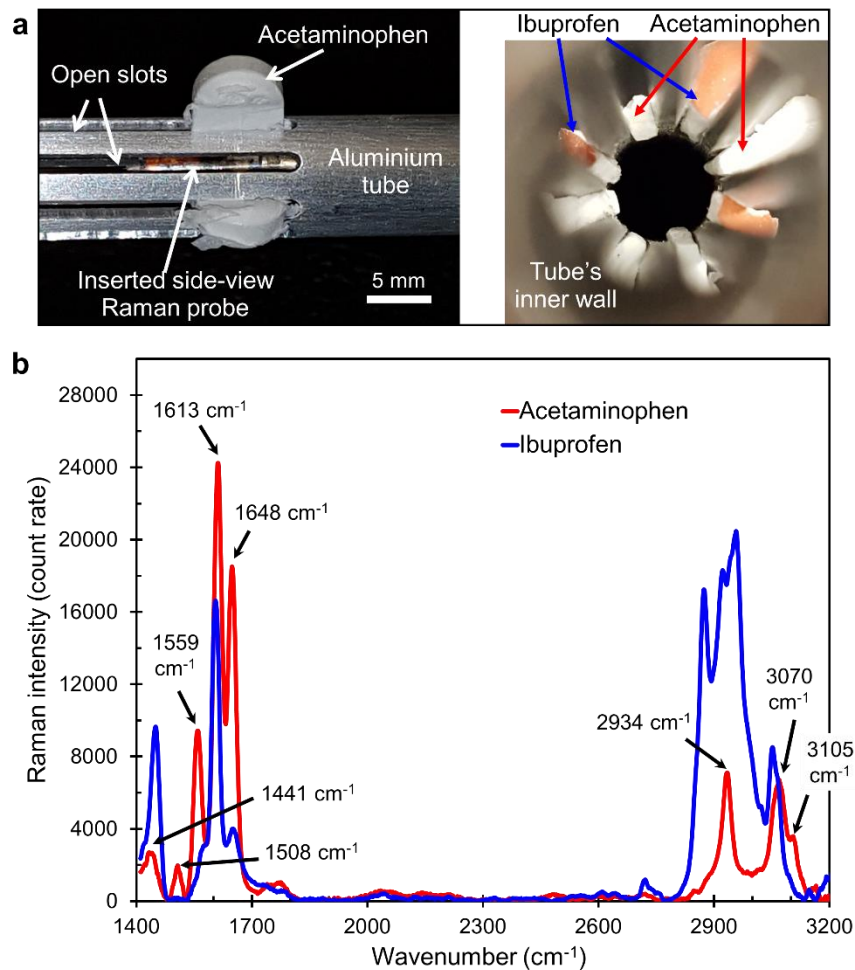


Figure 4.7: Angle-resolved chemical detection test. a) Tubular test set-up with acetaminophen and ibuprofen samples alternately loaded in the open slots (one of ibuprofen samples removed to show the device positioned inside the tube - left), and an axial internal view of the set-up with the two test chemicals (right). b) Raman signals of acetaminophen and ibuprofen samples obtained stepwise, and comparison of the former case with reported data [108] showing high accuracy of the measured peak positions (maximum wavenumber deviations: 0.5%).

4.4.2 *Ex-vivo* test with animal lung

Following the encouraging results with chemicals, we tested the integrated probe for real-time side-viewing scanning of animal bronchi *ex vivo*. This experiment used a harvested healthy bovine

lung (obtained from a slaughterhouse) that contained many bronchi with various sizes (with luminal diameters from ~10 mm down to ~1 mm or less). The probe was inserted into different bronchi (including right main bronchus as well as upper and middle lobar bronchi) of the right lung (Figure 4.8a). The micro actuator was operated with the 8-step rotational mode with 5-s stoppage at each angle. The spectrometer system continuously collected Raman data every one second during the operation. Figure 4.8b illustrates an example of analyzed real-time data (i.e., signals captured within the 1-s window) based on the raw data (Figure 4.9) that were obtained from an inner wall of the bronchus (entrance diameter ~4.0 mm) into which the probe was inserted. This measurement did not use any suction to remove mucus (similar to peripheral lung human tests [73]) and the probe was in contact with the inner wall of the bronchus due to its small size. The Raman spectrum, which shows biological characteristics with spectral peaks, was extracted by removing fluorescent signals from the raw data in the process. The acquired spectrum was compared with a reported Raman result of human lung measured using a common type of forward-view Raman probe [73] (the tissue structures of cattle lungs are known to be similar to those of the human lung [109], [110]). This comparison indicates that the wavenumbers of the obtained major Raman peaks closely correspond with the reported Raman peaks of the human lung showing deviations of <1%. This *ex-vivo* test demonstrates the efficacy of the developed side-viewing probe for performing tissue Raman analysis on the inner walls of narrow lumens.

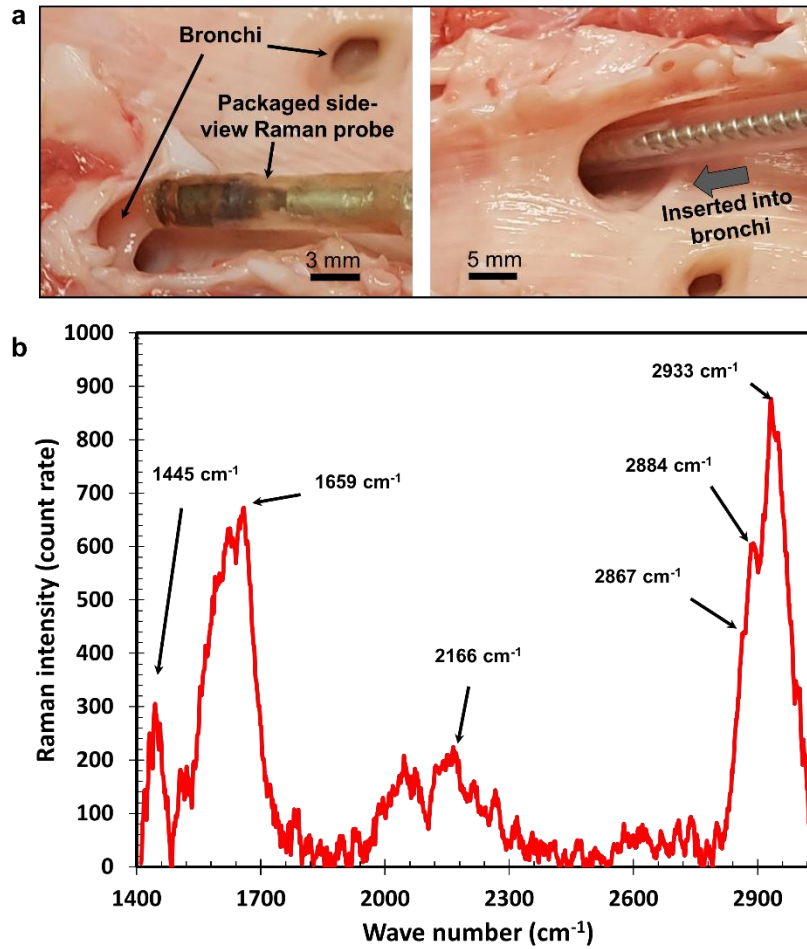


Figure 4.8: Ex-vivo test results with bovine lung. a) The side-view probe before inserting the probe to a bronchus (left), the side-viewing probe inserted into a bronchus (right). b) Obtained Raman spectrum with major peak wavenumbers showing good agreements with reported data [73] with low wavenumber deviations ($\leq 0.8\%$).

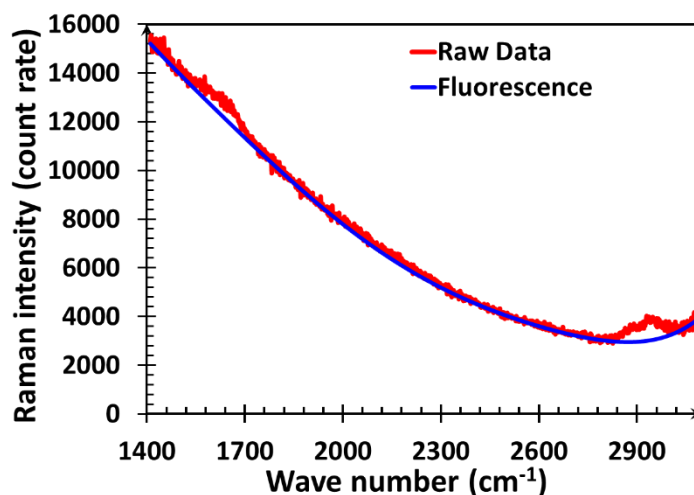


Figure 4.9: The raw data with fluorescence signals acquired from the *ex-vivo* bovine's lung test.

4.4.3 *In-situ* test with rat colon and *in-vivo* test with human skin

The animal test of the developed side-viewing Raman probe was conducted using the colon of a rat model. Raman scanning of mucosal tissue layers of the colon (~4 mm ID) was performed right after sacrificing the rat with carbon dioxide through a standard procedure as described in experimental section (Figure 4.10a and Figure 4.10b). The colon tissue was fresh and close to an *in-vivo* condition. The Raman signals were collected from the mucosal tissue in the same manner as the *ex-vivo* test (i.e., the micro actuator was rotating with the 8-step mode while acquiring the signals every second). The raw data with fluorescence signals acquired from a single sampling (Figure 4.11) were used to extract the Raman spectrum, which is shown in Figure 4.10c along with major peak wavenumbers. The comparison between the major Raman peaks obtained from the current murine test and the reported peaks of murine colon [111] indicates that the obtained data matched very well with the reference with small wavenumber deviations (maximum 0.5%).

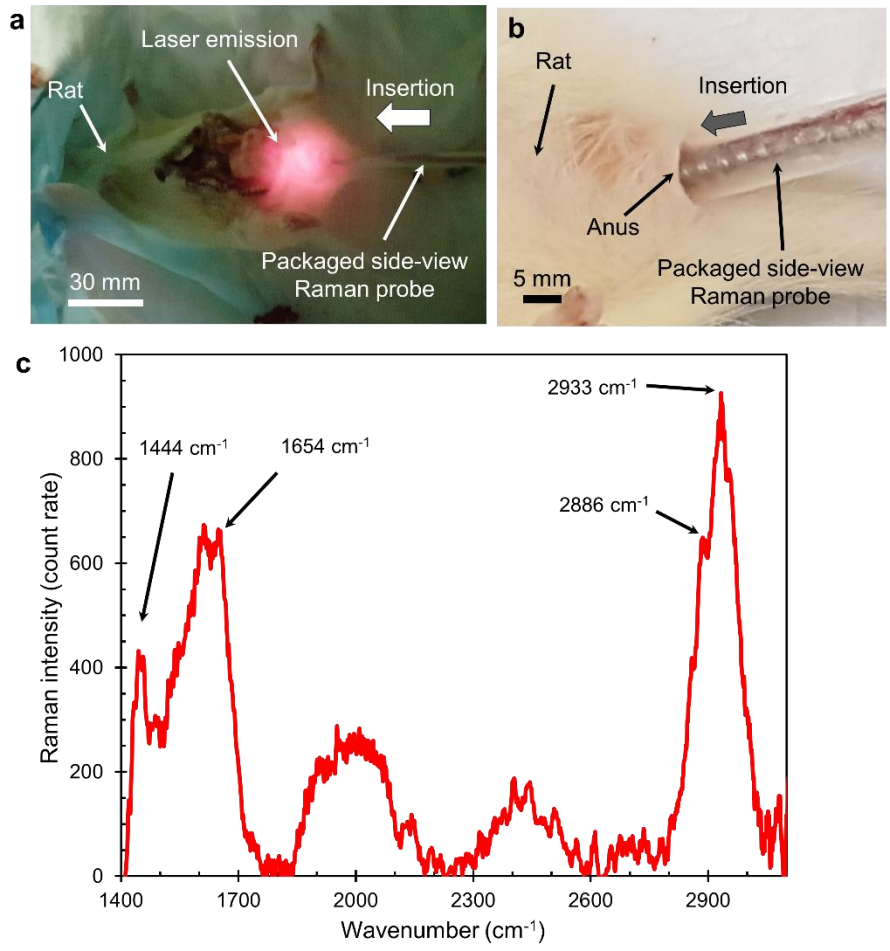


Figure 4.10: Results from in situ test using a rat model. a) The side-view Raman probe inserted into the colon of the euthanized rat showing emissions of probing laser. b) The side-viewing probe inserted to colon through anus and rectum. c) Raman spectrum obtained from the raw data showing major peak wavenumbers which are matched well with reported peaks of murine model [111] (wavenumber deviations $\leq 0.5\%$).

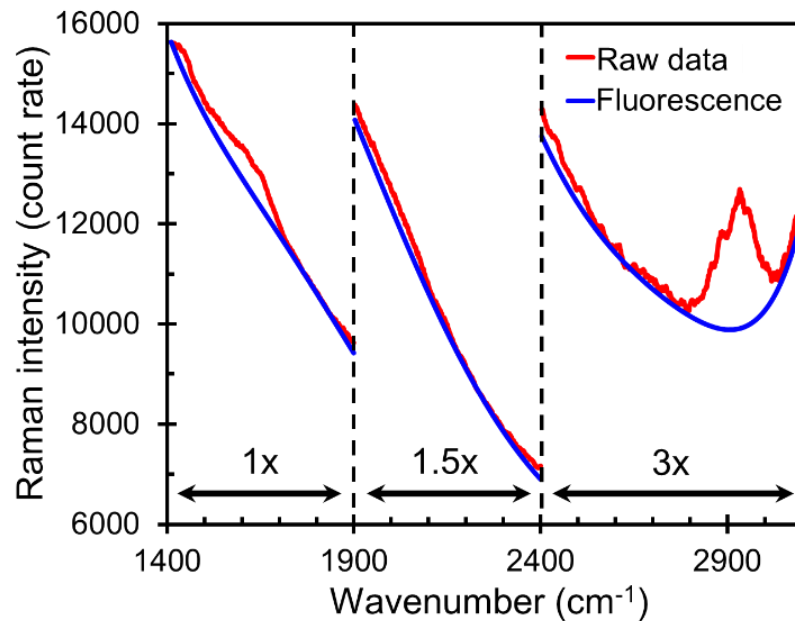


Figure 4.11: Results from in-situ test using a rat model. Raman raw data and fluorescence signals acquired from the 1-s sampling window at a single step angle. The intensities of the signals are plotted with amplified scales (1.5 \times and 3 \times) for higher wavenumber regions (1900-2400 cm^{-1} and 2400-3100 cm^{-1} , respectively) to show that fluorescence curve followed the raw data well (supporting the reliability of the Raman data) in a clearer manner.

There are two important sub-regions of Raman spectrum in human colon signals, 1400-1700 cm^{-1} and 2800-3100 cm^{-1} , where Raman peaks of normal colon tissue and carcinoma could be differentiated [112], [113]. These sub-regions cover major peaks from lipids, proteins, and nucleic acids in tissue. It was reported that the prominent Raman peaks of colonic tissue in human were 1445, 1618, 1655, 2850, 2885 and 2940 cm^{-1} [112], [113]. Those peaks were representative of $\delta(\text{CH}_2)$ deformation of proteins and lipids (1445 cm^{-1}), $\nu(\text{C}=\text{C})$ of porphyrins (1618 cm^{-1}), amide I $\nu(\text{C}=\text{O})$ of proteins (1655 cm^{-1}), symmetric and asymmetric CH_2 stretching of lipids (2850 cm^{-1} and 2885 cm^{-1}), and CH_3 stretching of proteins (2940 cm^{-1}). Given the facts that murine colon exhibit Raman peaks [111] close to those of human colon in the same sub-regions and that there

are many similarities between human colon cancer and colon cancer in rats [114], the obtained result is encouraging to support further evaluations for this application area.

We further assessed the efficacy of side-viewing RS probe function with live human skin and compared the results with reported data measured with forward-viewing Raman probes [113], [115], [116]. In this test, the active tip portion of the probe was all surrounded by healthy human skin (of the fingers), while rotating the mirror/laser stepwise (for 35 steps in total) and collecting and analyzing Raman data in the same manner as the previous tests (Figure 4.12a). An example of real-time single Raman spectrum collected from the 1-s sampling window and the averaged Raman spectrum acquired using the 35 sets of raw data collected from different angular/skin locations (along the circumferential scan path) are displayed in Figure 4.13. As can be seen, the characteristic peaks were observed in the two major sub-regions noted above. To validate the accuracy of the peak wavenumbers, the current data in the lower sub-region ($1400\text{-}1700\text{ cm}^{-1}$), which are representative of lipids and proteins (CH_2 and CH_3 bending modes) as well as proteins ($\text{C}=\text{O}$ stretching mode and amide I), were compared with reported results from *in-vivo* human skin tests performed using a regular Raman probe [113], [116]. The obtained peaks in the higher sub-region ($2800\text{-}3100\text{ cm}^{-1}$), which represented proteins (C-H vibration), lipids and nucleic acids (CH_3 asymmetric stretching), and lipids (CH_3 symmetric stretching), were also compared with the results reported for the particular spectral region [113], [115]. These comparisons showed excellent agreements with the above mentioned reference data with deviations of 0.3% or less. The wavenumbers of all four major peaks were highly stable among the acquired data (Figure 4.12b) and almost identical to those of the averaged spectrum. The standard deviations of these wavenumbers (with the 35 data sets) were calculated to be up to 2.7 cm^{-1} . This implies that the real-time single sampling could be sufficient to obtain reliable Raman data with the current system,

removing the need for a time-consuming process that collects many sets of signals at a specific location/angle and averages them for accuracy improvement. Considering 1-s stoppage per angular step for data collection, with a hypothetical model of 4-mm-diameter bronchi being scanned by a laser spot of 1.5-2 mm in size with 8 steps per 360° rotation, theoretically, the system (with an aid of external axial positioning mechanism) could scan the entire luminal surface for an axial length of up to ~7.5 cm in 5 min. As noted earlier, the system allows for arbitrary adjustment of stepping angle depending on particular clinical needs, and scanning throughput depends on the selection of the stepping angle.

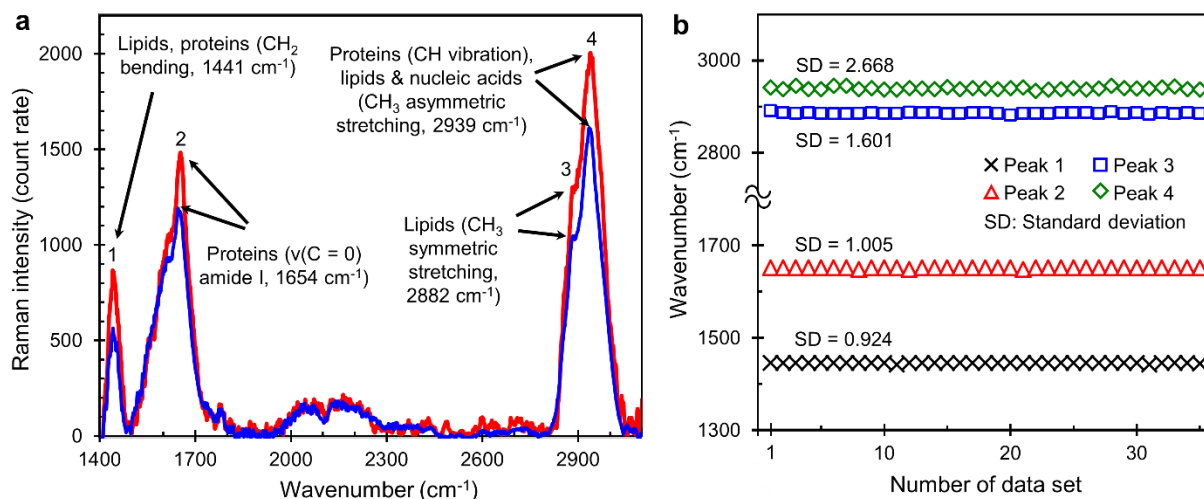


Figure 4.12: Results from the test using live human skin tissue. a) The average of 35 data sets of extracted Raman spectrum from different human skin sites acquired while scanning the laser on the skin tissue stepwise exhibiting four major peaks as labeled (blue), the single Raman spectrum obtained from the raw data (red), showing the major peak wavenumbers (with their corresponding signal sources) and results match well with reference data [113], [115], [116] (wavenumber deviations $\leq 0.3\%$). **b)** Trends of the major peak wavenumbers tracked through the acquired 35 sets of Raman data. The standard deviations of these characteristic wavenumbers were within 2.7 cm⁻¹ as shown.

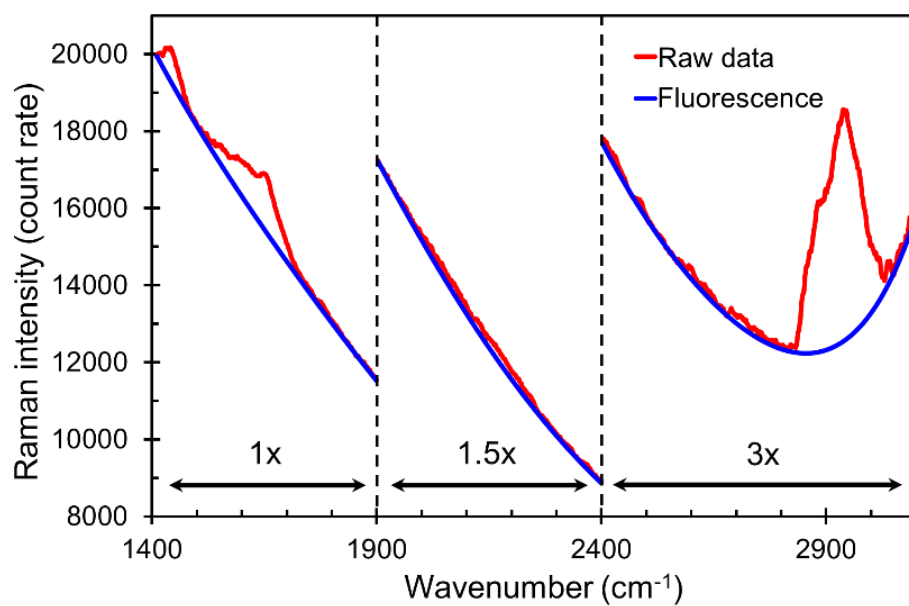


Figure 4.13: The raw Raman data and fluorescence signals acquired from the *in-vivo* human skin test. The intensities of the signals are plotted with amplified scaled (1.5× and 3×) for higher wavenumber regions (1900-2400 cm⁻¹ and 2400-3100 cm⁻¹, respectively).

Chapter 5: Miniaturized MEMS rotary actuator for high-speed operation of side-viewing endoscopy*

5.1 Introduction

In this chapter, I introduce a novel miniaturized MEMS rotary stepping actuator (Device III) that has a significantly lower diameter and higher performance with respect to Devices I & II for scanning small lumen such as peripheral lung in endoscopic probes. Numerical modeling is used to optimize the design of MEMS actuator and assess the performance of the stator designs. In light of this, FEM is utilized to investigate the influence of different designs of stator coils (by varying coils' lead widths) on electromagnetic fields provided to the rotor space. The 2D map of simulated fields with 4 given widths of stator leads is probed at the central (pole) location of the rotor (cubic magnet) surface when positioned right below an active lead, which is placed in the inner surface of the stator tube. Also, the effect of coils' lead width on the field distribution in the rotor space is assessed. To compare the performance of the current design (Device III) with Devices I & II, all devices are operated with the same operation mode and electrical conditions (i.e. single controlling mode and 1A feeding current). The achieved results from the FEM modeling are used for designing and developing the miniaturized MEMS actuator (Devices III) to enhance its size and performance and consequently to be integrated and packaged with an endoscopic catheter. This novel design is configured to raise rotational speeds while lowering power consumption and heat generation.

*Part of this chapter will appear in the following publication:

S.M.H. Jayhooni, B. Assadsangabi, Geoffrey Hohert, P. Lane, H. Zeng, K. Takahata, "High-speed and stepping MEMS rotary actuator for multimodal 360° side-viewing endoscopic probes.", IEEE MEMS conference 2020, Vancouver, Canada.

Afterwards, the developed actuator is characterized based on its rotational performance, power consumption and heat generation. The achieved results are compared with previous data shown in Chapter 3 to illustrate the advantages of Devices III.

5.2 Principle and design of the miniaturized MEMS rotary stepping actuator

Improving the rotational velocity of the actuator provides the opportunity to broaden the application of the MEMS actuator to be used not only in RS but also in other modalities such as OCT and EUS. This goal can be achieved by increasing the electromagnetic force created in the actuator. One effective and direct way to increase the force is to enlarge the volume of the driver magnet. The magnet of Device III, hence, is extended along the tubular axis direction and connected directly to a micro prism mirror. It has a rectangular cubic shape and is 3x bigger than the original shape while maintaining the same square cross-section shape but a 3x greater length than the driver magnet of Device II. The rotor component is enclosed in the stator tube as illustrated in Figure 5.1. Another way to increase the electromagnetic force is by reducing the distance between the stator circuit and the magnet. Originally, the stator circuit was wrapped and bonded on the outer wall of the stator tube. To reduce the distance, relocating the stator circuit inside the stator tube may be effective because the stator coils are closer to the rotor and create more electromagnetic fields on the driver magnet. This setting is achieved by using a shrinkable polymer tube as the stator tube. The advantages of using a shrinkable tube is that it can achieve any stator ID dimensions and remove the need of using adhesive for attaching the stator circuit to the stator tube (The prototyping method will be explained later). The maximum size that the stator tube can shrink down to is 77% of its original size. In Device III, the ID and OD of the tube shrink down from 1.90 mm to 1.65 mm and from 2.40 mm to 2.25 mm, respectively, in order to assess the rotor

to revolve easily. The rectangular cubic magnet has the dimension of $1.0 \times 1.0 \times 3.0 \text{ mm}^3$ and is magnetized along the radial direction of the catheter device. The longer side of the magnet is along with the axial direction of the stator tube and catheter device shown in Figure 5.1. The prism mirror in this design is the same as the one implemented in Device II (Figure 5.1). The stator circuit is fabricated with the photolithography method explained previously (Chapter 2). In this design, the dimensions of the coils are matched with the targeted ID of this device (1.65 mm) and the width of coils' leads is $400 \mu\text{m}$ which is half of leads' widths in Devices I & II (Figure 5.2). Decreasing the leads' widths also helps to increase the electromagnetic fields and the results are demonstrated later. The clearance between the rotor surfaces and the inner wall surface of the stator which is between $100 \mu\text{m}$ and $300 \mu\text{m}$ is filled with oil-based ferrofluids used in Device II. Also, the controlling system and technique including PWM method, current divider, timing controller and motor shield are the same as the ones described in chapter 3 (Figure 5.2).

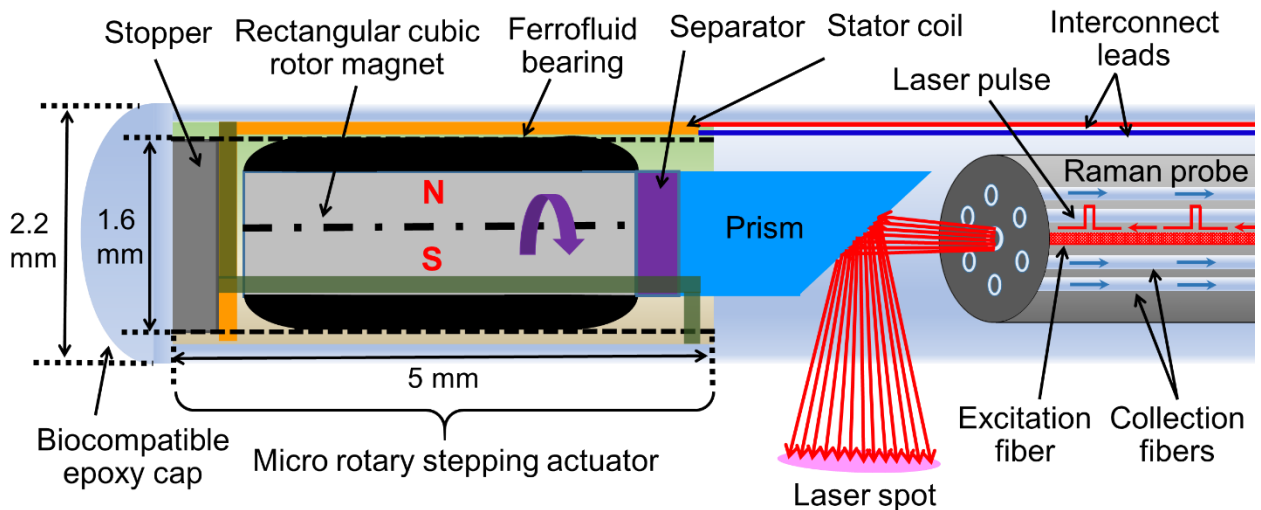


Figure 5.1: Design of the novel MEMS rotary stepping actuator circumferential beam scan

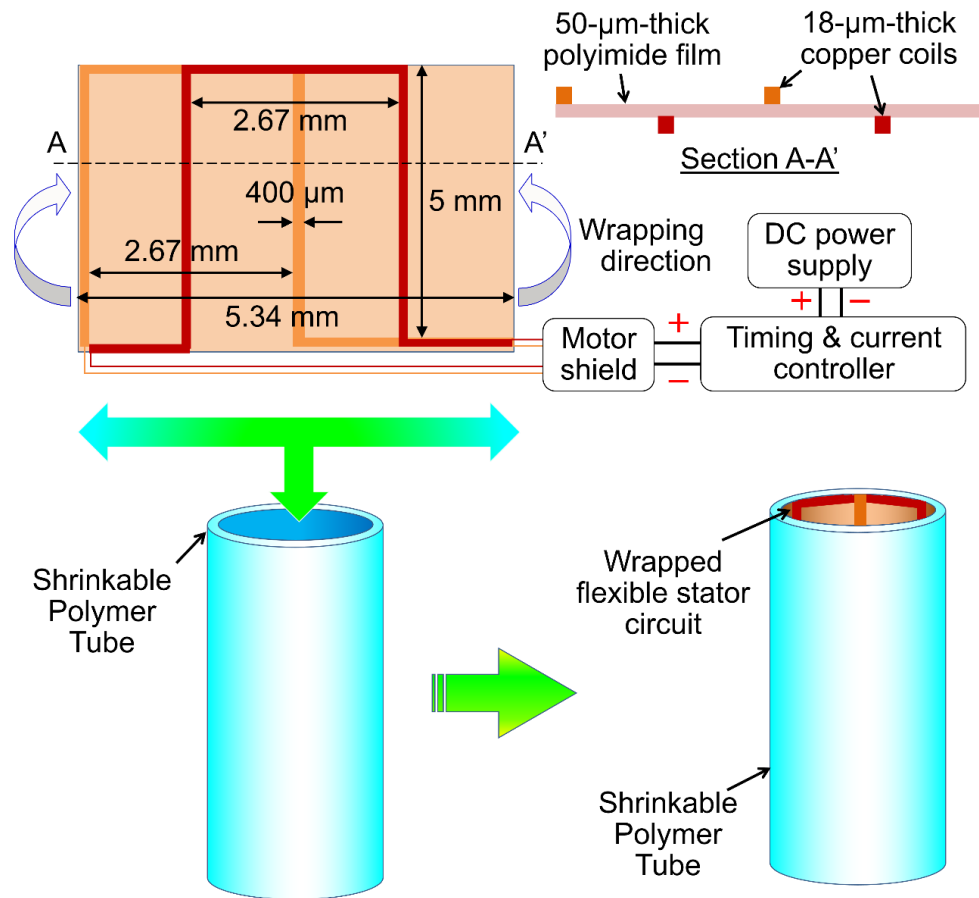


Figure 5.2: Stator circuit assembly and its connection to the driver module developed for Device III operation as well as placing the flexible stator circuit inside the shrinkable polymer tube

5.3 Finite element analysis of tubular stator

In this section, FEM technique is used to model the electromagnetic fields created inside the Devices II & III and compare the magnetic flux density on their driving magnets. In addition, FEM is used for investigating the effect of stator coil's lead width on the electromagnetic field. Four designs with different width of the coil's lead (200- μm , 400- μm , 600- μm , 800- μm widths) are modeled by FEM technique to investigate the influence of the lead's width on creating electromagnetic field on the side of the rotor driving magnet (located at the center of the stator). In all designs, the ID of the stator is 1.65 mm, the same as the targeted stator dimension for prototyping. FEM technique, numerical equations, boundary conditions and other assumptions for the evaluation of electromagnetic field around the rotor are the same as the ones used in Chapter 3. By using this simulation, the 2D map of the electromagnetic fields around surfaces of the driving magnet served as the main part of the rotor in Device III are investigated. The magnet is radially located in the center of the stator tube and its surface is positioned right below the active leads carrying 1 A current. Figure 5.3 (a)-(d) displays the cross-sectional maps of flux density for the abovementioned designs with four different lead's widths to demonstrate the influence of copper coils' widths on creating electromagnetic field inside the stator. Figure 5.4 shows the simulated maps of electromagnetic fields created by the stator lead width of 200 μm in the stator tubes of Device III and Device II. The results verified the effectiveness of placing the stator circuit inside the stator tube in enhancing the field strength around the rotor magnet.

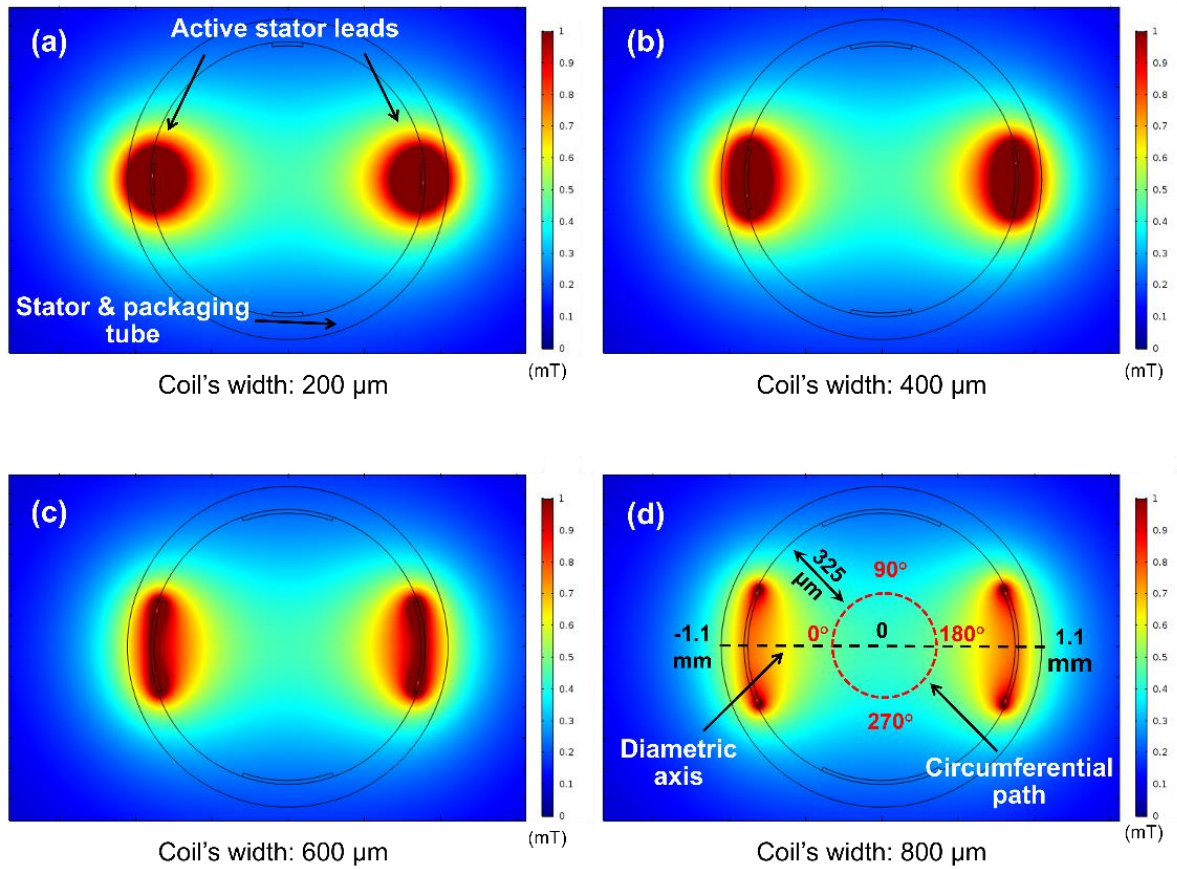


Figure 5.3: 2D cross-sectional maps of simulated electromagnetic fields inside the single-layer stator for four different active stator lead widths: a) 200 μm, b) 400 μm, c) 600 μm and d) 800 μm with 1.0-A current feed.

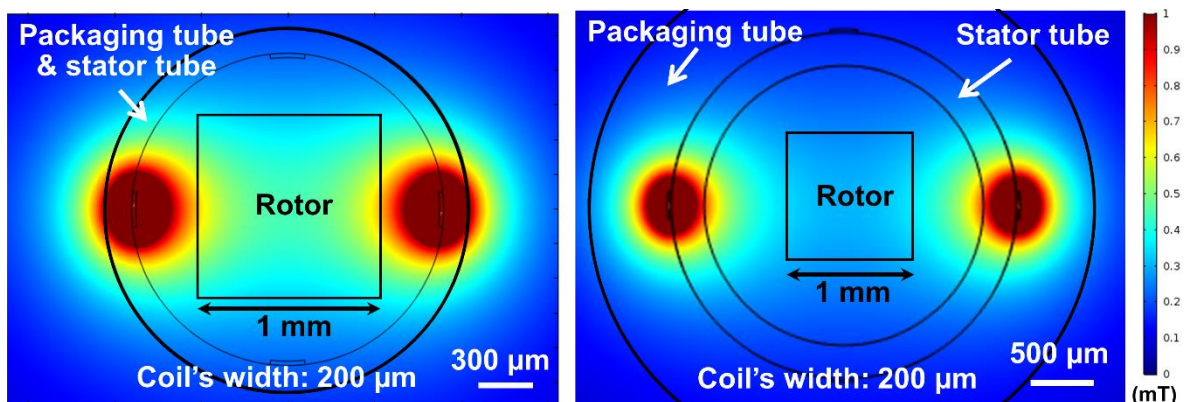


Figure 5.4: Simulated maps of electromagnetic fields created by the stator lead width of 200 μm in the stator tubes of the Device III (left) and Device II (right), verifying enhanced field strength in the tube stator.

FEM technique is used to calculate and simulate the electromagnetic flux inside areas of Devices II & III along the radial direction bridging the two active leads (Figure 5.5 (the axis shown in Figure 5.3 (b))), and also along the circumferential path 325 μm away from the inner stator circuit surface, Figure 5.6. Although the leads' widths of prototypes are different in Device II (800 μm) and Device III (400 μm), for investigating the influence of placing the stator circuit inside the stator tube wall (Device III) and bonding it around the outer stator tube wall (Device II), the lead's width for both cases (Devices II & III) are chosen to be 800 μm in numerical simulation. The magnetic flux density created with the same stator line widths of 800 μm on the side of the driving magnet is enhanced by up to 61 % in Device III in comparison with Device II, illustrated in Figure 5.5 and Figure 5.6. It is also worth mentioning that by decreasing the coil lead's width, the electromagnetic field on the magnet surface increases. For instance, the field is decreased by 13.4% when the lead's width decreases from 800 μm to 400 μm . However, coils with narrower lines' width create more heat due to the Joule heating effect, hence, there is an important temperature restriction on decreasing the lines' width that the maximum temperature of the device should be within allowable biocompatible temperature which is explained later.

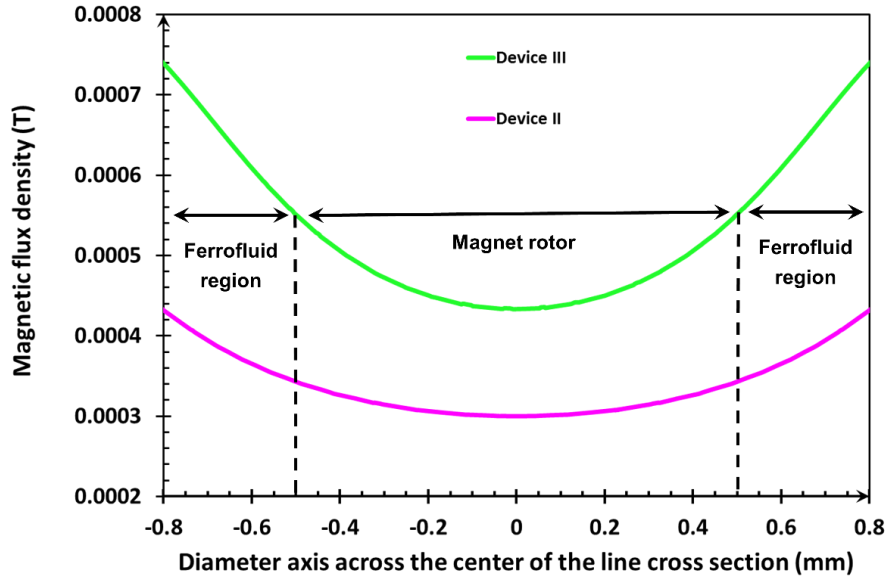


Figure 5.5: The distributions of magnetic flux density along the diametric axis bridging the two active leads of Devices II & III with 1.0-A current feed passing the same stator line width (800 μm).

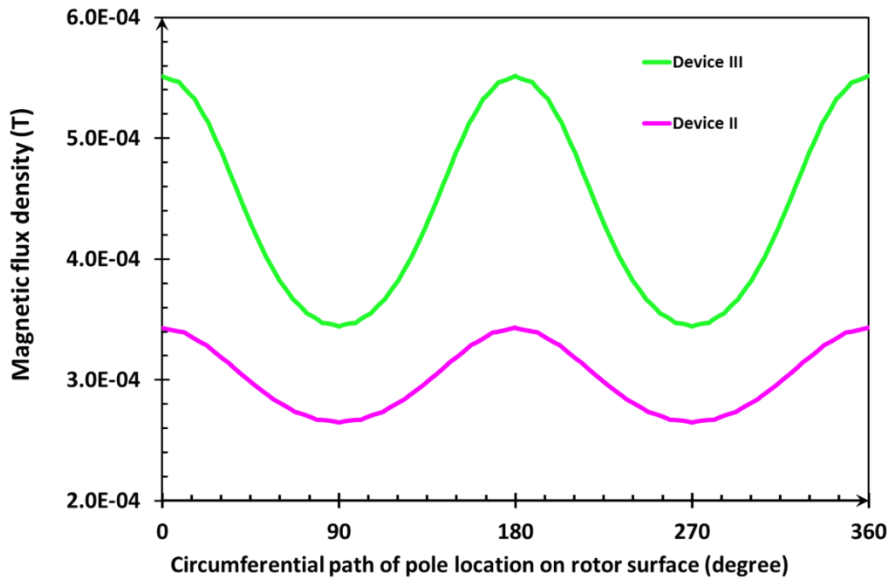


Figure 5.6: The distributions of magnetic flux density along the circumferential path at 325- μm inward from the stator circuit's inside wall the diametric axis bridging the two active leads of Devices II & III with 1.0-A current feed passing the same stator line width (800 μm). This circumferential path is the path where the rotor magnet poles passes during each actuator rotation.

5.4 Prototyping

For prototyping Device III, the stator circuit is developed by a photolithography-based method described in Chapter 2. The rotor component is constructed by a rectangular cubic magnet (N52 with Zinc coating, Ningbo Xinfeng Magnet Industry Co., China), a MEMS separator and a prism mirror. The MEMS separator is used as a connection between the magnet and prism mirror in order to prevent any ferrofluid leakage from the magnet to the prism mirror which prevents the reflective part of the prism to become opaque and not work properly. Based on the shape of the separator, it can collect different amounts of ferrofluids. The 45°-angled prism mirror is aligned and bonded to the MEMS separator (this part describes with more details later) (Figure 5.7). The oil-based ferrofluid (the same ferrofluid used for Device I and Device II) is applied to the magnet with a controlled amount (~4 μL in total) using a microsyringe. The stator circuit is coated with 10- μm -thick Parylene C. In the FEM section (section 5.3), it is shown that placing the stator circuit inside the stator tube enhances the electromagnetic fields around the rotor and causes to create higher electromagnetic force. However, it is challenging to practically fabricate the prototype based on this design, particularly the stator circuit should be precisely rounded to allow the rotor to revolve smoothly. The advantage of this design is to remove the polyimide tube used in Device II and to utilize only the packaging tube (explained in Chapter 4) to play two roles: 1- stator tube and 2- packaging tube. This design contributes to decreasing the overall OD diameter of MEMS actuator and providing the opportunity to be used in different endoscopic modalities for in vivo scanning of small human lumens. To circumvent the fabrication challenge, the stator circuit is wrapped around a stainless steel rod with an OD of 1.65 mm and the stator circuit and the rod are inserted into the shrinkable polymer tube. As noted previously, the tube can shrink to $\leq 77\%$ of its original size, with the original inner ID and OD of 1.90 mm and 2.40 mm, respectively. Next, the heat

airflow with the temperature of 230 °C is applied to all flexible stator circuit, stainless steel rod, and shrinkable tube continuously and uniformly with a digital temperature-controlled heat gun (TR Industrial, CA, USA). The ID and OD of the stator tube including the stator circuit are shrunk down to 1.65 mm and ~2.2 mm, respectively. The method also has the advantage to remove the bonding step (which is not practically very accurate and causes to increase the overall actuator size), as during the heat shrinking process, the inner surface of the polymer slightly melts and fixes around the stator circuit by being trapped and pressurized between the shrinkable polymer and the rod without using any adhesive (Figure 5.8a). In the next step, after cooling down them, the rod is removed and extracted from the inner part of the stator (polymer and flexible circuit) displayed in Figure 5.8b. The four terminals of the stator circuit are wire bonded to power the stator circuit with controlled pulses of driving currents. Figure 5.9 displays the completed actuator including its rotor and stator integrated with dummy endoscopic probe (for integration testing) and packaging tube.

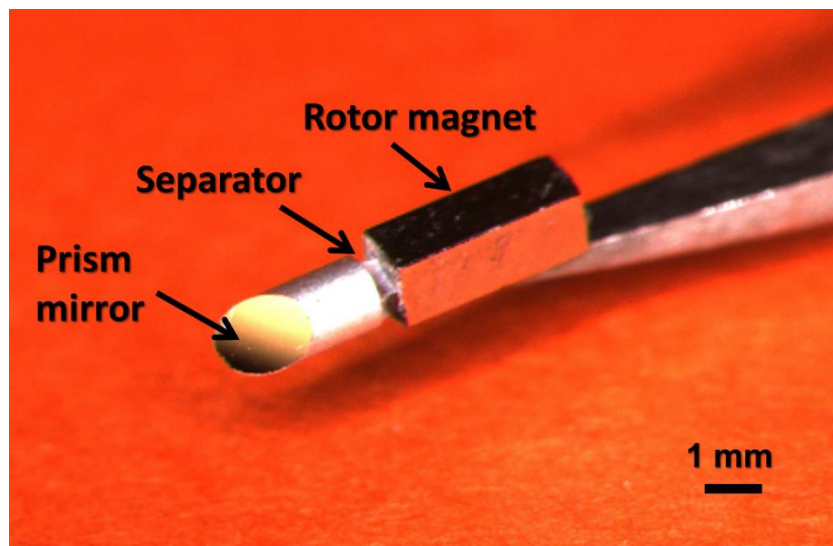


Figure 5.7: Rotor component of the actuator including rectangular cubic magnet, the separator and prism mirror.

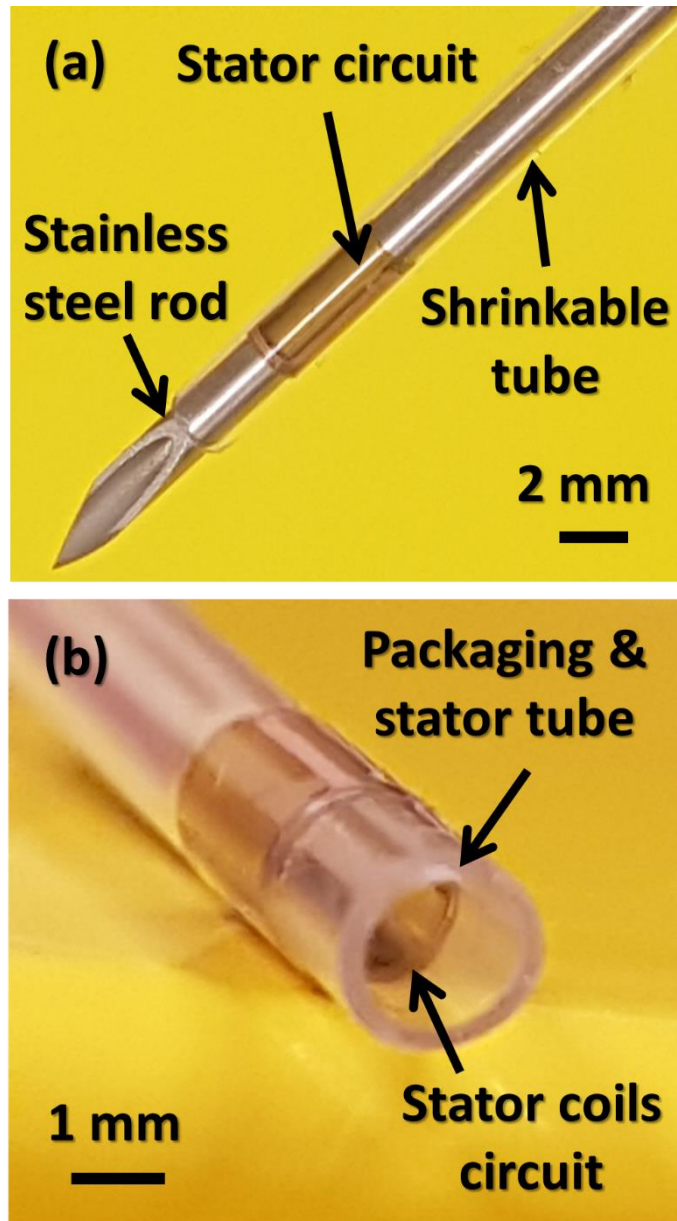


Figure 5.8: Device III stator a) before removing the rod, b) after removing the rod and its inner view of the stator including the polymer tube and flexible circuit showing the inner wall is round enough for the rotor to revolve in it.

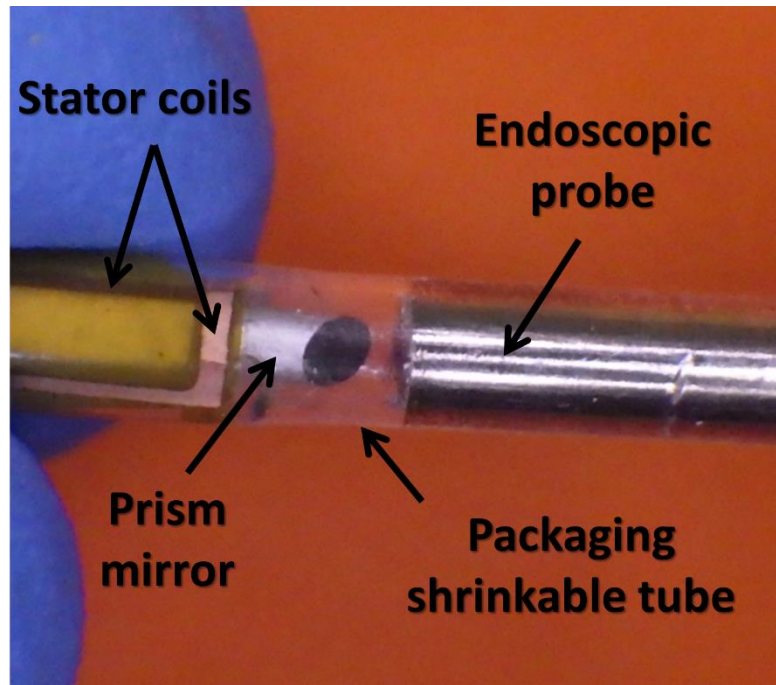


Figure 5.9: Completed endoscopic prototype including its packaging tube prior to injecting ferrofluids.

5.5 MEMS separator

5.5.1 Fabrication method

For the fabrication of the MEMS separator part, a negative epoxy-based photoresist (SUEX thick film sheet, DJ MicroLaminates, Inc., Sudbury, USA) is used by placing it between the driver magnet and the prism. This thick film sheet is comprised of cationically cured modified epoxy and prepared under a highly controlled solvent-less process for the uniform coating purpose. This film sheet is a negative photoresist that can be patterned by UV light. To pattern the film sheet on the end surface of the magnets, a 3D disc with a rectangular hole at the center of the disc is designed. The disc had 4 cm OD and 3 mm thickness, and the hole has 1 mm \times 1 mm cross-section area (the same dimension of the rectangular magnet) and it passes all the way through the disc. Hence, the magnet can be located in the hole of the disc and secured properly. The disc is fabricated with a 3D printer (Freeform Pico2, Asiga, USA) using an ABS-based photopolymer (PlasGRAY Version

2, Asiga, USA). The film sheet with a thickness of 300 μm is placed on the top of the disc while holding the magnet and then they are laminated by a hot roll lamination system. The temperature of the hot rolls sets to 70 $^{\circ}\text{C}$ and the lamination process is performed with the rolling speed of 0.5 ft/min and the pressure of around 60 kPa (Figure 5.10a). For the exposure process, a mask aligner (Model NXQ4006, Neutronix-Quintel Co, USA) with 365 nm optics is utilized to expose 1800 mJ/cm^2 to the thick film. The post-exposure bake is performed at 65 $^{\circ}\text{C}$ followed by another 95 $^{\circ}\text{C}$ baking step (Figure 5.10b). Finally, the thick film is developed by propylene glycol methyl ether acetate with mild agitation at room temperature (Figure 5.10c). The whole process flow steps of the separator patterning is shown in Figure 5.10. Figure 5.11 illustrates two magnets with different MEMS separators (with different ferrofluid absorption capacity) after removing the samples from their disc holders. The magnet with the MEMS separator shown in Figure 5.11 (left) is attached to the prism mirror with adhesive (LePage[®] Gel Control Super Glue, Henkel Co., ON, Canada) which is accurately placed on the top of the thick film structure (Figure 5.7).

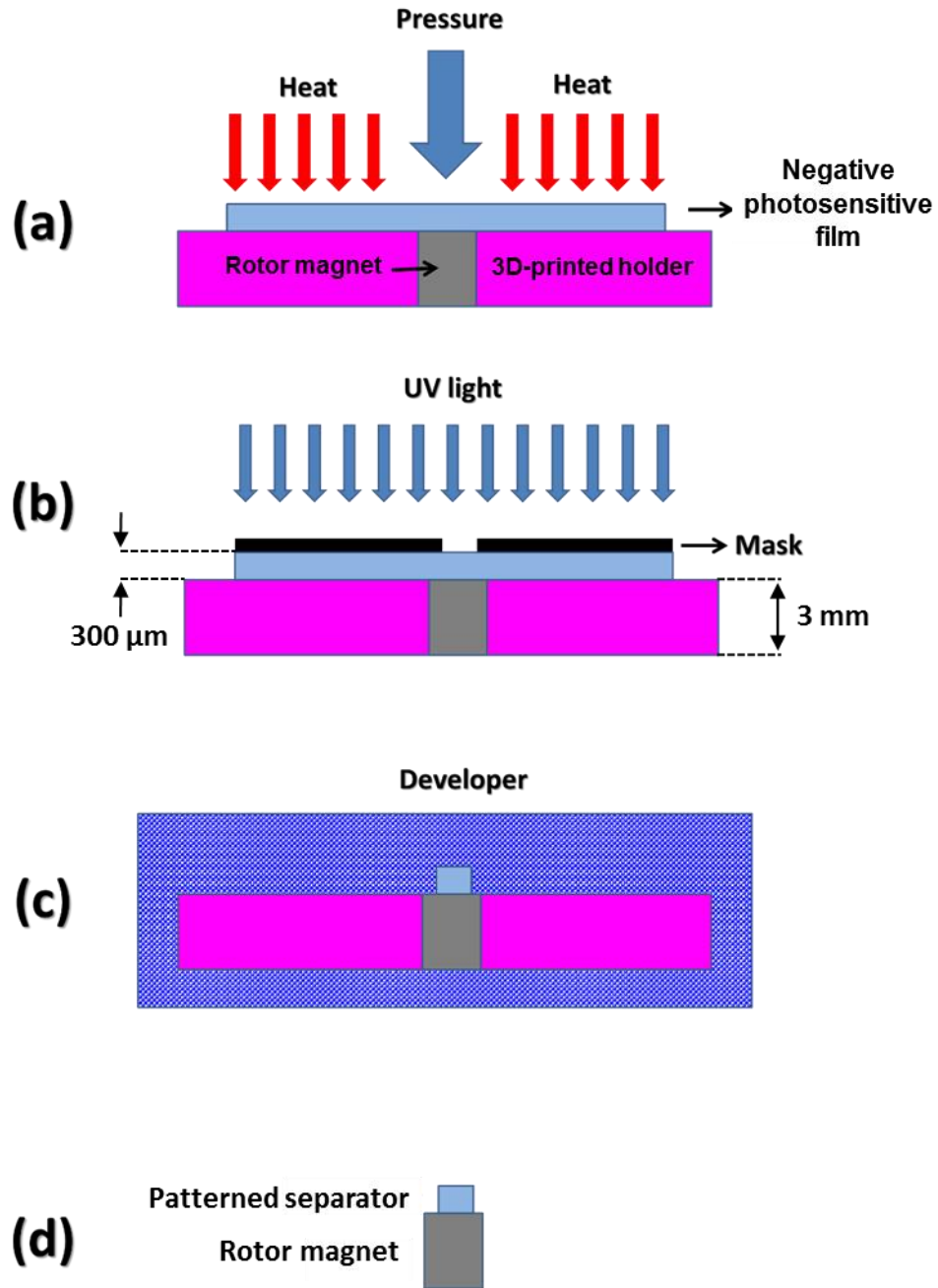


Figure 5.10: Process flow steps of the separator patterning and fabrication.

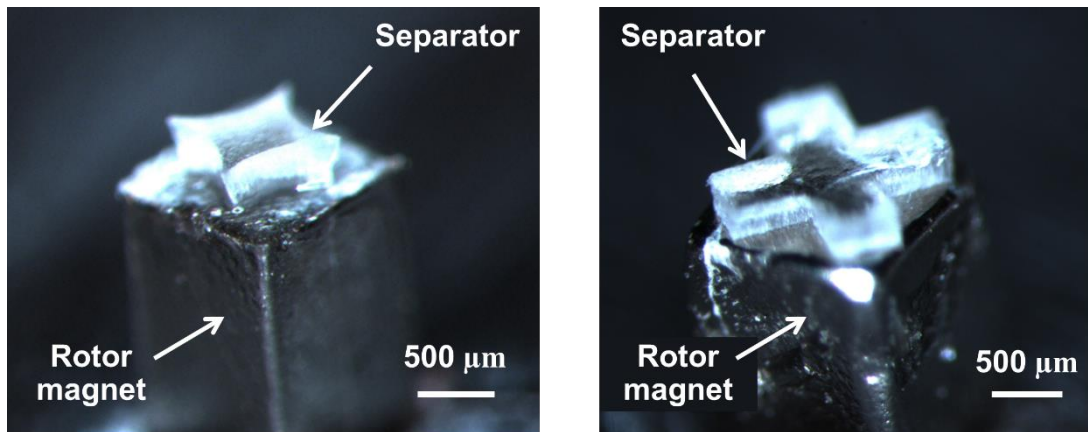


Figure 5.11: Two different types of MEMS separator fabricated on the one end of the rotor magnet.

5.5.2 Evaluation

In order to investigate the effectiveness of the separator in preventing the ferrofluids leakage to the prism magnet, a rotor without a separator was also fabricated (the prism mirror attached to the magnet directly with adhesive).

Figure 5.12 illustrates the ferrofluid was applied to this rotor magnet without the MEMS separator for 6 different amounts from zero to $\sim 4\mu\text{L}$ and it shows how ferrofluid tended to accumulate on the poles of the magnet for a different amount of applied ferrofluid. It is also worth noting that when the ferrofluid applied, the ferrofluid equally accumulates on the north- and south-pole sides of the rectangular cubic permanent magnet surfaces and it is self-sustained around the magnet. However, by increasing the amount of ferrofluid on the rotor magnet, this fluid reaches the prism. Figure 5.12f shows by applying $\sim 4\mu\text{L}$ ferrofluid on the rotor magnet, the ferrofluid leaked to the prism mirror even before locating the rotor inside its stator (Figure 5.13). Furthermore, the results demonstrate that after placing the rotor in the stator and running the MEMS actuator, ferrofluid covers up to $\sim 300\ \mu\text{m}$ of the prism longitudinally (Figure 5.14). In the current design, leaking ferrofluid has no adverse influence on the reflective part (the main part of the prism mirror).

However, this covering is problematic as the fluid could accidentally reach the reflective surface of the rotating actuator when the length of the prism component is shortened for further miniaturization of the rotor in the future design.

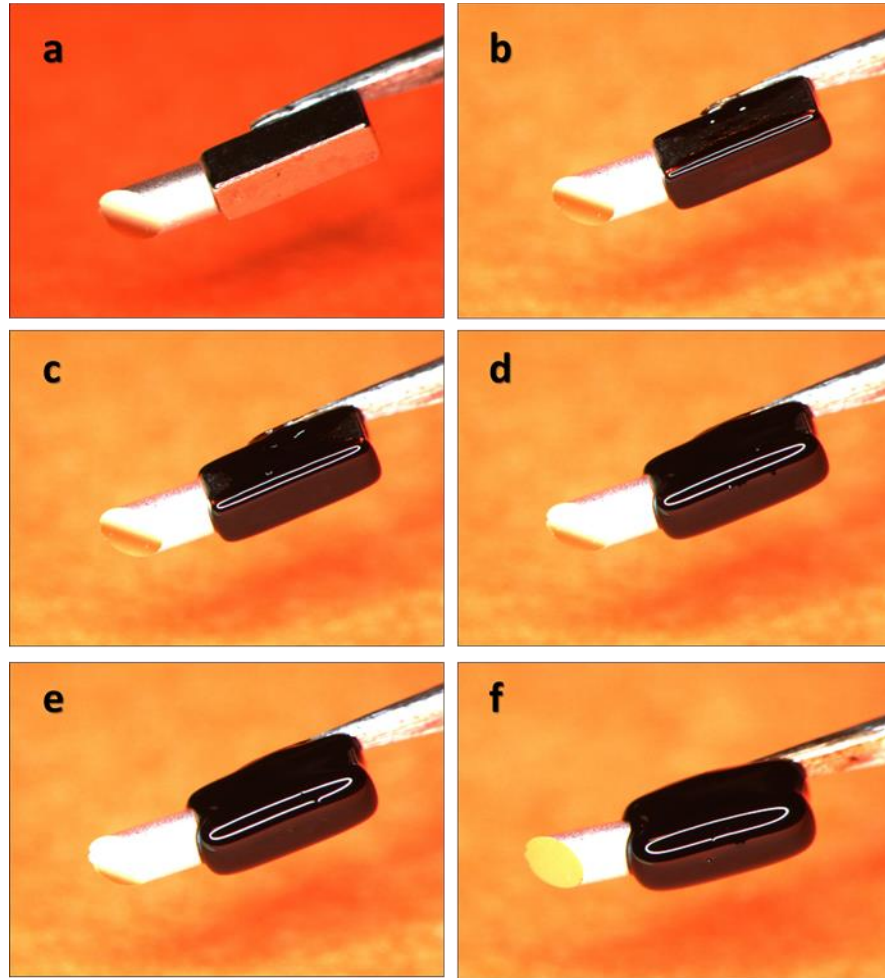


Figure 5.12: Ferrofluid is applied to the rotor magnet without the MEMS separator showing the cases of 6 different amounts from zero to $\sim 4\mu\text{L}$.

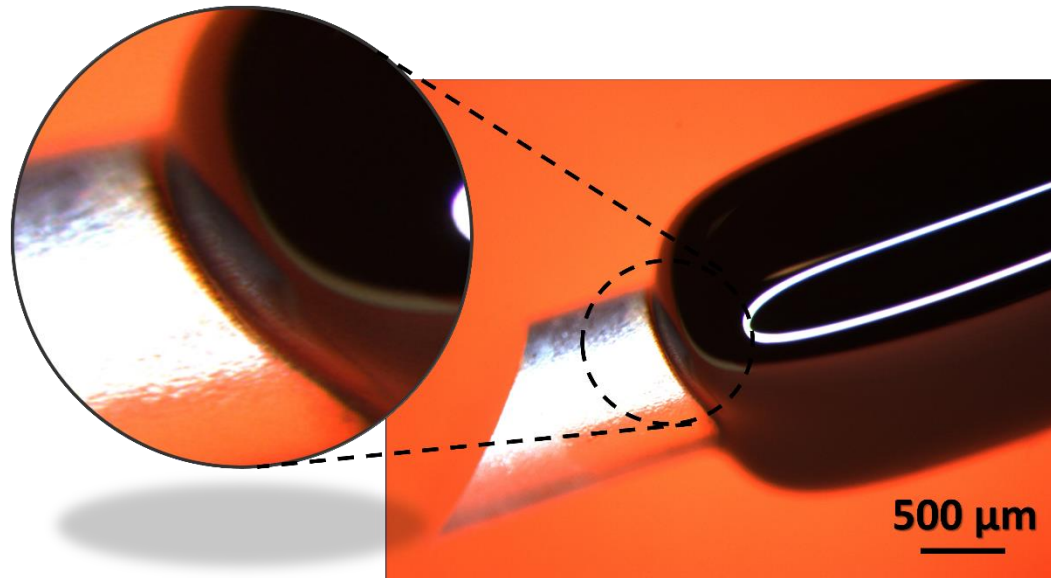


Figure 5.13: ~4μL ferrofluid is applied to the rotor magnet before locating the rotor in its stator, ferrofluid reaches to the prism mirror.

Next, the ferrofluid was applied to the rotor magnet with the MEMS separator in 8 steps from zero to the same total amount (~4μL) (Figure 5.14). As shown in Figure 5.16, although ferrofluid overflowed out of the magnet, the separator trapped the extra fluid and prevented any leakage to the prism mirror side in all the steps, including when the maximum amount of ferrofluids (~4μL) was applied to the rotor magnet (Figure 5.15). The rotor was finally inserted into the stator and run with the rotational speed of 300 rpm to illustrate the effectiveness of the separator in successfully blocking the fluid to cover the prism mirror components (Figure 5.16).

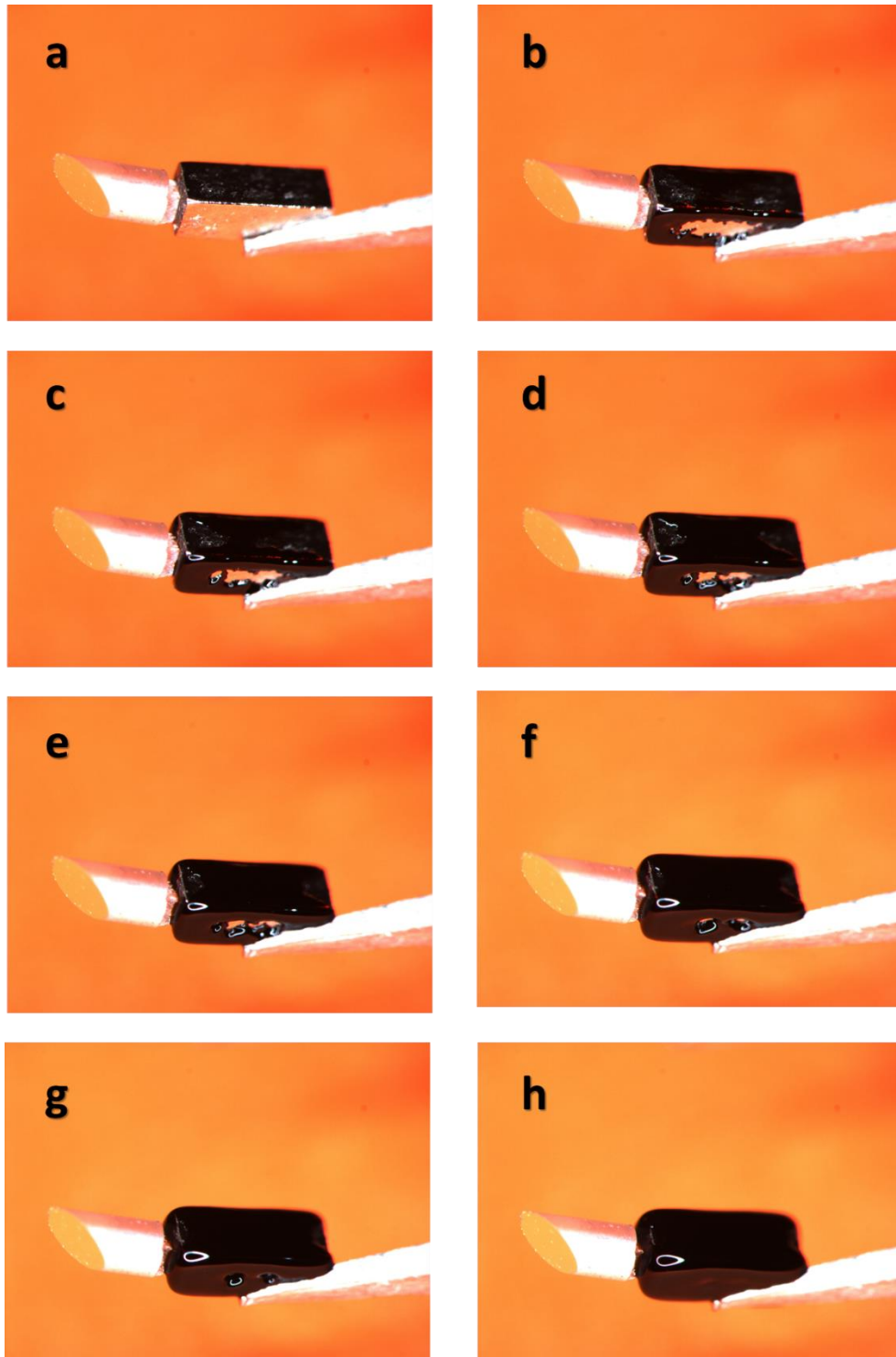


Figure 5.14: Ferrofluid is applied to the rotor magnet with 8 different amounts from zero to $\sim 4\mu\text{L}$, showing the effectiveness of the separator in making a gap between the two parts of the rotor and preventing ferrofluids leakage from the magnet to the prism mirror.

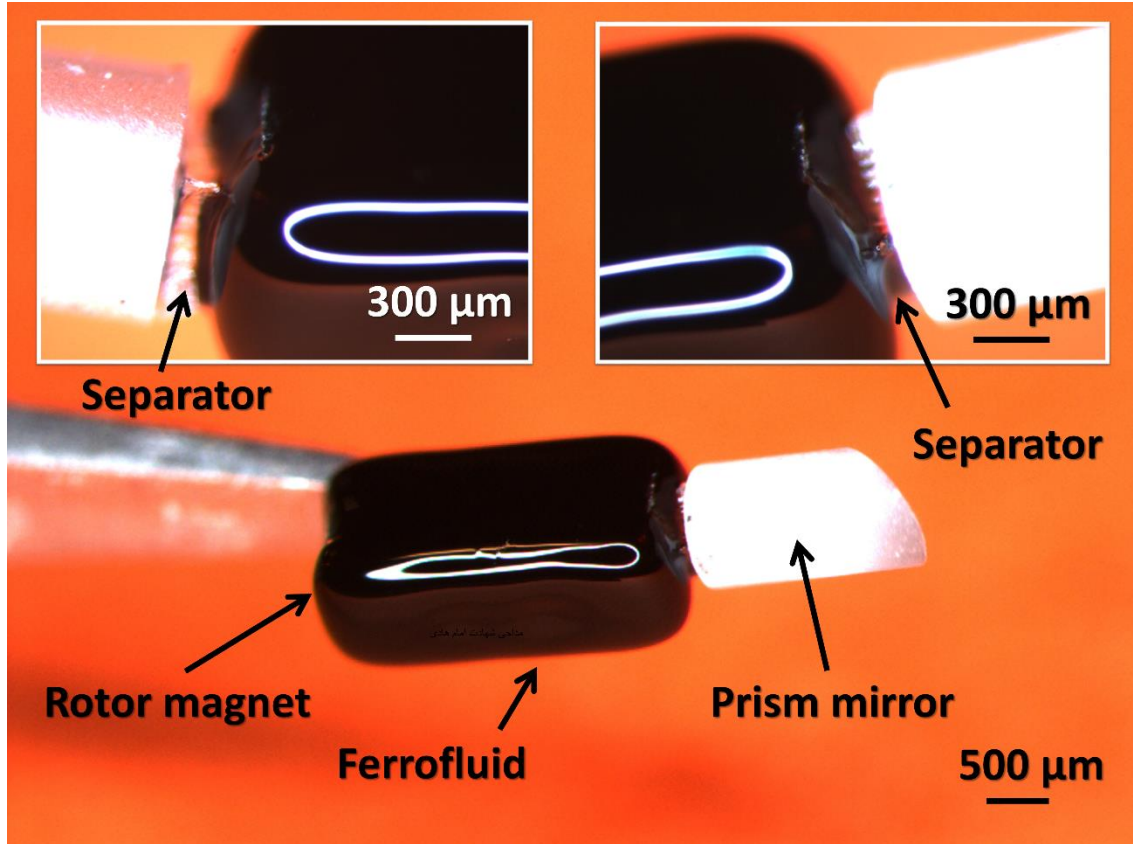


Figure 5.15: Rotor magnet is subjected to the maximum amount of ferrofluids ($\sim 4\mu\text{L}$) used in the actuator, the two inset figures show two different views of the separator and illustrate the effectiveness of the separator in preventing the ferrofluid to spread to the prism mirror.

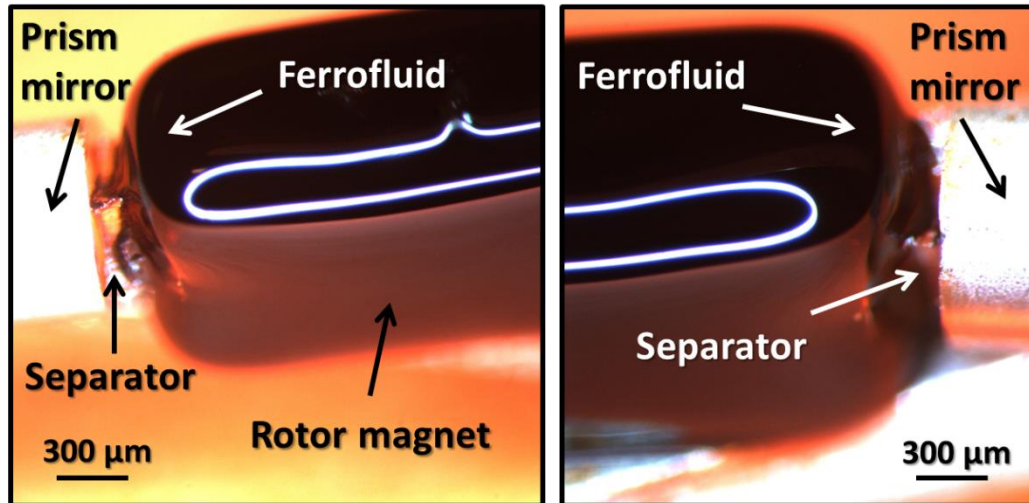


Figure 5.16: The rotor magnet after being inserted into the stator and run with the rotational speed of 300 rpm, two different perspectives of the rotor after revolving are shown in this figure, the separator successfully blocked ferrofluid to cover the prism mirror components.

5.6 Experimental results and discussions

5.6.1 Speed characterization

The fabricated prototype was operated in the single-coil mode explained in Chapter 3 to characterize the relationship between the rotational speed and the driving current in the mode. The experimental set-up was similar to the one used for the characterization of Device II explained in chapter 3. For measuring the rotational speed as a function of the driving current, the driving current and its direction passes through the stator coils were set that the actuator could rotate from low speed, 1 rpm, to higher speed such as 2500 rpm and the results were compared with Devices I & II (Figure 5.17). It illustrates that, as predicted from the simulation results provided in Section 5.3, the stator distance from the rotor's magnet poles had a significant influence on the electromagnetic fields inside the stator. As noted previously, the rotary driver magnet of the rotor was $3\times$ longer and consequently showed a stronger response to the magnetic field as well as the gap between the inner stator wall and the driver magnet filled with ferrofluid was smaller. All

those factors contributed to significant improvement in enhancing the rotational speed of Device III in comparison with the before-mentioned devices (Device I & II explained in Chapters 2 & 3). In particular, the rotational speed of Device III could boost to 2500 rpm by feeding 0.56 A current which was much higher than the preceding devices (Devices I & II). By comparing the achieved results of current device and Devices I & II for certain feeding powers (currents), the speed improvement of the novel device became more noticeable and reached approximately up to 30× and 125× higher speeds at the same feeding current, respectively (Figure 5.17). The results also show that Device III could reach the rotational speed of 600 rpm with up to ~79% smaller feeding currents (or ~96% smaller power consumption) compared to the case of the preceding devices (Device I & II). These results well represented the new motor's ability of high revolution rate efficiency as experimentally demonstrated.

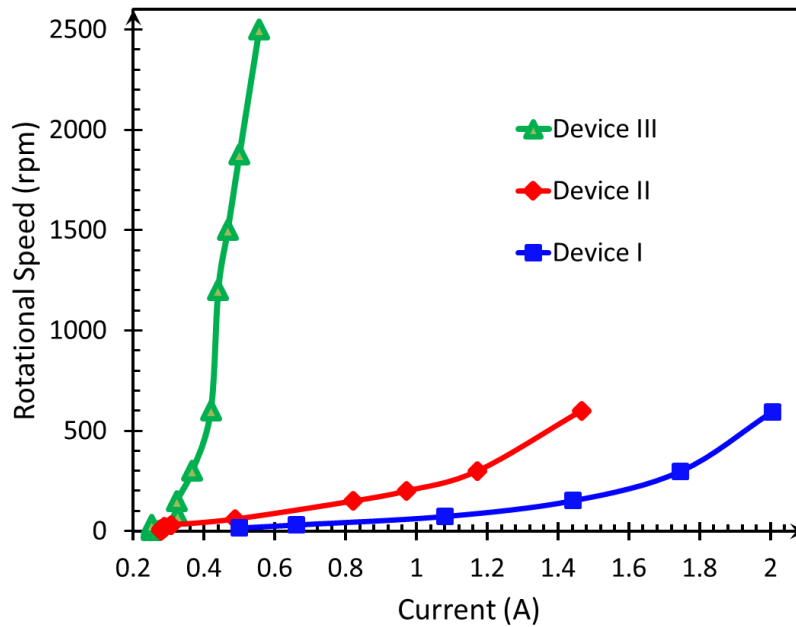


Figure 5.17: Measured rotational speed vs. driving current for the developed actuator (Device III) and comparison with those of preceding devices: Device I, explained Chapter 2 and Device II described in Chapter 3.

5.6.2 Thermal characterization

Regarding the biocompatibility of the catheter probe in terms of maximum allowable temperature, it was mentioned in Chapter 3 that temperature exceeding ~ 43 °C can cause damages to the tissues that are in contact with the endoscopic probe. The operating surface temperature of the present device depends on different factors such as stator coils dimensions (i.e. copper lines' width and thickness), feeding current and packaging material (i.e. thermal insulation characteristics). The stator coil's width was 400 μm which was half the size of the preceding devices. This size increased heat production in the coils due to having less cross-section area and passing higher current per cross-section area. However, this presented actuator required less driving current in comparison with Devices I & II to reach a certain rotational speed (e.g. 600 rpm), thus it was expected to create less heat as a result of Joule heating effect in general. Also, the stator tube played the role of a packaging layer or thermal insulator which could suppress the temperature of the outmost surfaces of the motor-embedded catheter device. To assess the collective effect of these factors, the thermal behavior of Device III was experimentally characterized under the single-coil operation mode that in general involved the use of higher currents for high-speed operation. The measurement was conducted using the actuator prototype (operated with varying rotational speeds; the relationship between the rotational speed and the current) while recording temperature distribution on the active device exploiting the same IR camera. The temperature map result with the IR camera is displayed in Figure 5.18 after placing the stator circuit inside the stator tube. It illustrated how the feeding current increase the temperature in the stator is due to the Joule heating effect.

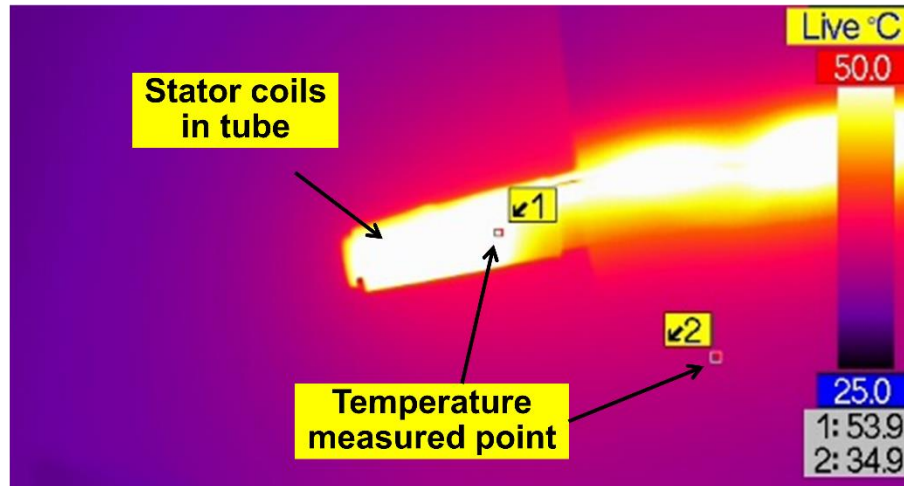


Figure 5.18: Temperature map result with the IR camera around the MEMS actuator after completing the stator prototype.

Figure 5.18 illustrates the maximum actuator temperature vs. driving current for Device III and the comparison with those of the preceding designs (Devices I & II). It shows also the maximum temperature increased from room temperature (28.6 °C) measured for the rotational speeds of up to 2500 rpm. The results indicate the merit of the developed device compared to the counterparts in suppressing temperature increase when operated at identical rotational speeds. For example, at 300 rpm, the current device exhibited 34.9 °C, which is lower than the biocompatible threshold temperature (~43 °C), whereas the counterparts (Devices I & II) reached 40.7 °C and 51.6 °C, respectively. The device temperature dropped from Device I & II by ~65% and ~74 % for the given speed of 600 rpm in comparison with Devices I & II, respectively. This is a significant outcome in light of extending application range of the device. In the present actuator, the maximum temperature reached ~42 °C (within the threshold) at the rotational speed of ~2200 rpm which is significantly higher than the preceding devices, hence, Device III can be utilized in other modalities requiring higher rotational speed (e.g. OCT). Additionally, Figure 5.19 shows the present actuator

could reach 20× and 5× higher speed in comparison with Devices I & II, respectively, while the actuator maximum temperature is within the biocompatible temperature range (i.e., ≤ 43 °C).

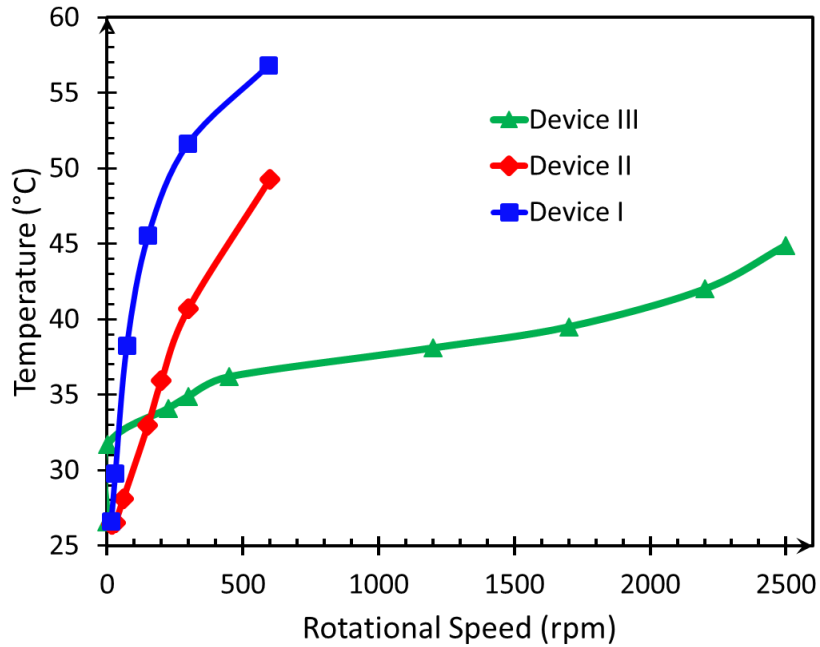


Figure 5.19: Measured maximum actuator temperature vs. driving current for the developed actuator and comparison with those of the preceding designs (Devices I & II).

The measured maximum temperatures of the operating device (Device III) is plotted as a function of the driving current in Figure 5.20. It illustrates that by increasing the feeding current higher than 0.6 A, the maximum created temperature passes the threshold level explained previously (i.e., ~ 43 °C). Therefore, this developed device should be run within the above-mentioned current for precaution to be safely exploited in in-vivo tests. However, this amount of current is enough for this device to reach almost 2500 rpm which is significantly higher than Devices I & II in order to be used in other endoscopic modalities including OCT and EUS. Also, this allowable current level can be raised by having an extra packaging layer on the motor to serve

as a thermal insulator (at the cost of increasing the outer diameter of the device). Finally, the overall comparison of the features and performance of those three devices (I, II, III) is shown in Table 5.1.

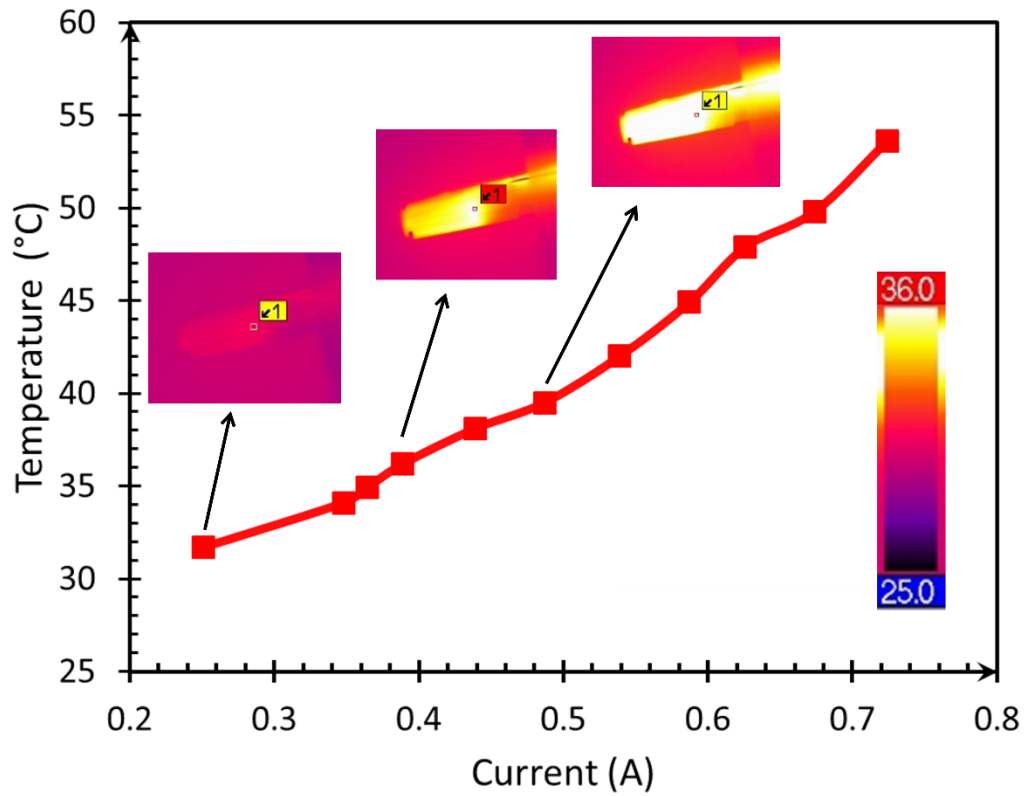


Figure 5.20: Characterization of operating temperature of the presented MEMS actuator with varying driving current and its IR thermal images.

Table 5.1: the overall comparison of the features and performance of those three devices (I, II, III), data are rounded.

	Device I	Device II	Device III
Maximum achieved speed (rpm)	600	600	2500
Actuator OD size before packaging (mm)	4.5	2.8	2.2
Actuator OD size after packaging (mm)	6	4	2.2
Maximum speed within temperature threshold (rpm)	100	400	2200
Feeding current at speed of 600 rpm (A)	2.0	1.5	0.4
Maximum speed at feeding current of 0.6 A (rpm)	20	100	2500
Power consumption at speed of 600 rpm (W)	40	22.5	1.6

Chapter 6: Conclusion

In this dissertation, ferrofluid based MEMS actuators are experimentally and numerically investigated for microendoscopic application. To achieve this goal, through research and investigations, including numerical modeling and simulation, experimental design, fabrication, characterization and verification as well as chemical, animal and human tests on MEMS actuators and side-viewing Raman probe have been performed. In this chapter, a summary of this research's achievements and contributions is presented.

6.1 Contributions

The main contribution of the present dissertation is about designing, developing and optimizing the novel endoscopic catheter for circumferential and 3D endoscopic screening. This thesis is the first research that has demonstrated the miniaturized and fully packaged side-viewing Raman probe device enabled by novel MEMS rotary actuators has the potential to enable *ex-vivo* and *in-vivo* raw tissue analysis without using any biomarkers or labeling techniques. The application of this endoscopic catheter is not restricted to RS and can be extended to other modalities such as OCT and EUS. Also, the novel catheter can be a good candidate for potentially detecting cancers in different human lumens. In order to succeed in the achievement, three different MEMS stepping actuators (Devices I, II & III) enabled with the ferrofluid levitation mechanism were designed and prototyped. Devices were integrated and packaged with the RS system to demonstrate the functionality of the actuator for angle-resolved side-viewing Raman analysis through *ex-vivo* animal lung tissue, an *in-situ* murine colon model, and *in-vivo* human tissue tests. Furthermore, the MEMS technology was exploited to develop those miniaturized and custom-designed actuators enabled with the controlling system to uniquely revolve them with arbitrary

numbers of stepping per rotation with programmable scanning angle an important key to successfully collecting localized Raman signals from raw and unlabeled tissues. This opens an avenue to detect local *in vivo* lesions with a highly reliable signal collection. For the packaging of the motorized side-viewing probe, a biocompatible, electrically insulated and transparent (for Raman spectral range) polymer was used and this packaging prevents Raman signal distortion or significant noise creation which regularly happened in most polymers. In the prototyping process, a novel self-aligned method enabling the MEMS actuator to be precisely integrated with the endoscopic probe was used. This method provided the opportunity for the endoscopic probe and the actuator to be optically aligned with each other and consequently collect signals from targeted tissues completely and accurately.

More detailed contributions of the present research and the achievements and contributions of each chapter are provided as follows:

I. Chapter 2

In this chapter, a new ferrofluid-enabled microactuator with selective/simultaneous rotary and linear motion capabilities has been developed (Device I). Ferrofluid-based levitation was utilized to enable a low-friction and self-maintained liquid bearing for rotor/slider assembly within the stator tube. To achieve 360° rotation, the rotor/slider assembly was electromagnetically actuated using the two coils microfabricated on the outer surfaces of the stator tube. Ferrofluid also provided a sealing effect for the rotor/slider assembly inside the tube, which permitted linear actuation using fluidic pressure for displacements of up to 13 mm. The simultaneous circumferential-axial scanning of a laser beam was successfully demonstrated with the prism-mirror-coupled prototype. The axial stability of the rotation was measured to be $<127 \mu\text{m}$. An application of the developed

prototype for circumferentially localized endoscopic RS was experimentally demonstrated through chemical detection as well as an *ex-vivo* test using mouse tissue, proving the effectiveness of the prototype design for the targeted applications.

II. Chapter 3

In order to improve the size, performance and controllability of the actuator described in Chapter 2, a novel electromagnetic micro stepping motor based on a ferrofluid levitation mechanism has been developed for its application to side-viewing microendoscopes (Device II). The developed prototype of the micromotor, housed in a thin polyimide tube serving as the stator substrate, was experimentally demonstrated to provide higher performance in important aspects of the device, including rotational speed, power consumption, and thermal behavior, with a smaller miniaturized form compared with the preceding device (Device I). Finite element analysis indicated the significance in the effect of the tube's wall thickness on the formation of driving electromagnetic fields, and simulation results were used to optimize the stator coil design. The device operation with the dual-coil control scheme in combination with the pulse width modulation method was revealed to enable precision stepping control with finer resolutions, demonstrating twice and four times the step numbers per rotation, compared with the conventional single-coil scheme the stepping resolution of which was limited by the physical number of stator coils. The results obtained with the new micromotor were promising for its application to microendoscopic imaging, especially for the Raman spectroscopic modality that requires fine-step scanning of a probing laser beam.

III. Chapter 4

In this chapter, the previous actuator explained in Chapter 3 has been optimized to be used in the actual Raman catheter. Hence, a side-viewing endoscopic RS device has been demonstrated using a custom-designed micro rotary stepping actuator enabled with a self-sustained ferrofluid bearing (Device II). The tubular micro actuator was integrated and packaged with a forward-viewing Raman probe to achieve full 360° RS tissue analysis towards its application to cancer detection within narrow conduits *in vivo* in real-time. The bench test using different chemicals showed that the side-viewing probe and its system could resolve and distinguish the chemicals that were arranged circumferentially and obtain correct signals at high accuracy. The device was tested with the airway and colon of animals, without using any biomarker, as well as with human skin *in vivo* in an angle-resolved and real-time manner through programmed stepping defined by the micro actuator. All the acquired data clearly illustrated tissue Raman signals with high S/N and were revealed to be reliable with negligibly small variations. These results suggest that the developed side-viewing Raman device could be a good candidate for finding lesions within the bronchi of the peripheral lung. To this end, further tests will follow to evaluate the sensitivity of the developed side-viewing device in lesion detection through comparative tissue analyses. The technology potentially offers wider diagnostic applications for other small luminal organs.

IV. Chapter 5

In this chapter, a novel miniaturized MEMS rotary stepping actuator (Device III) was introduced with significantly lower diameter and higher performance in important aspects of the device, including rotational speed, power consumption, and thermal behavior, with a smaller miniaturized form compared with the preceding device for using in endoscopic probes to scan

small lumen such as peripheral lung. Finite element analysis was utilized to investigate and optimize the stator design of the MEMS actuator and compare the results with the preceding device. The stator design was analyzed and the magnetic field effects on the rotor were illustrated. In the fabrication process, a new method for placing the stator flexible circuit inside the stator tube was proposed. This method assisted the rotor to smoothly and perfectly revolve inside the stator with approximately up to $\sim 30\times$ and $\sim 125\times$ higher rotational speeds in comparison with the Devices II & I explained in Chapter 3 and Chapter 2, respectively, while feeding powers (currents) were the same. Also, in this new actuator, the results displayed that the present device consumed up to $\sim 96\%$ lower electrical power compared with the case of the preceding devices. Finally, it showed the present actuator could reach $5\times$ and $20\times$ higher speed in comparison with Devices I & II, respectively, while the actuator maximum temperature is within the biocompatible temperature range (i.e., $\leq 43\text{ }^{\circ}\text{C}$).

6.2 Future work

The overall objective of the future work is to design and develop a novel side-viewing endoscopic probe enabled with a further miniaturized rotary actuator with better performance in scanning and detecting local *in vivo* lesions in small human lumens with high reliability.

Future works as the continuation of this dissertation can be grouped into the following categories:

I. Investigations on miniaturizing the MEMS actuators, including design, fabrication and characterization as well as improving their performance.

Further design and development of the MEMS stepping actuator is recommended to be performed in order to decrease the axial and radial size of the actuators to be used in smaller

endoscopic probes. The probe should have the capability to scan small lumen such as the peripheral lung (e.g. 1.5 mm diameter or smaller). Some of the methods of developing the actuator can be to use different magnet shapes such as cylindrical magnets or cubic magnets with smaller dimensions constructed from stronger magnet materials, to develop the stator circuit with the new design that can create higher magnetic fields with less current consumption, and also to locate the developed circuits as close as possible to those driver magnets, as well as exploiting packaging tubes with ultrathin wall thickness. The characterization of the developed actuator, including rotational speeds, heat generation, power consumption and reachable number of rotational steps will be the next step to show its performance in comparison with preceding devices. Another important component is to optimize the actuator design to create more magnetic fields and consequently, the actuator can work with higher speeds and lower power consumption. One of the approaches can be to use different stator circuit designs (double-layer circuits) and place them inside the stator tube in order to enhance the electromagnetic fields and consequently augmenting rotational speed and decreasing power consumption.

II. Further study on the integration of actuators and catheter methods for full 360° side-viewing applications with maximized signal collection with different endoscopic techniques.

The axial and radial stability of the new design should be investigated and improved, which will contribute to achieving better alignment. Further investigation is recommended regarding the materials that can reflect excitation signals and collect tissue signals without distorting them, which can be significantly helpful for maximizing the tissue signal collection and consequently detecting cancers in lumens. Finally, a new integration method should be utilized to remove the adverse influence of blind spots culminating in wire blockage, passing along the transparent

window to power the actuator and consequently achieving a full 360° side-viewing angle-resolved endoscopic catheter.

III. Evaluating the performance of the miniaturized side-viewing Raman probe in small human lumens, particularly peripheral lung and detecting cancers.

Other work that can be done in the future is to evaluate the miniaturized side-viewing Raman catheter in actual clinical endoscopic tests in human organs such as the GI tract, respiratory tract (lung, peripheral lung, bronchi trees) and esophageal. The final suggestion is to investigate the Raman signals achieved from cancerous tissues and compare them to healthy ones and benign lesions to identify the Raman peak differences and opening a new avenue for detecting early cancers.

IV. Investigations on a novel MEMS actuator having the potential to be used in different endoscopic modalities for *in-vivo* human tests

The next study that can be performed is to design and develop a MEMS actuator that has all the features and advantages of Devices I, II & III, including having the potential for linear and angle resolved rotary motion, in order to achieve high axial and radial scanning resolutions while having small OD to be exploited in small human lumens, and being completely packaged with biocompatible materials for actual human tests. It should be improved a way that it can rotate stepwise, low speed and high speed in order to have the potential to be used in different modalities such as RS, OCT, EUS and multimodal endoscopic systems. For the performance evaluation, it is important to investigate if the endoscopic probe integrated with this MEMS actuator and connected to different endoscopic modalities can scan lumens with high resolution and accuracy. The final

suggestion is to conduct *in-vivo* lumen tests with healthy and cancerous human tissues with other modalities (e.g. OCT and EUS) to open a new avenue for detecting early cancers.

Bibliography

- [1] A. Iino, K. Suzuki, M. Kasuga, M. Suzuki, and T. Yamanaka, "Development of a self-oscillating ultrasonic micro-motor and its application to a watch," *Ultrasonics*, vol. 38, no. 1, pp. 54–59, 2000.
- [2] Shi-Uk Chung, Gun-Yong Hwang, Sang-Moon Hwang, Beom-Soo Kang, and Han-gyoo Kim, "Development of brushless and sensorless vibration motor used for mobile phone," *IEEE Trans. Magn.*, vol. 38, no. 5, pp. 3000–3002, 2003.
- [3] F. Gemperle, N. Ota, and D. Siewiorek, "Design of a wearable tactile display," pp. 5–12, 2002.
- [4] R. Bogue, "Assembly of 3D micro-components: A review of recent research," *Assem. Autom.*, vol. 31, no. 4, pp. 309–314, 2011.
- [5] B. Watson, J. Friend, and L. Yeo, "Modelling and testing of a piezoelectric ultrasonic micro-motor suitable for in vivo micro-robotic applications," *J. Micromechanics Microengineering*, vol. 20, no. 11, 2010.
- [6] D. Floreano and R. J. Wood, "Science, technology and the future of small autonomous drones," *Nature*, vol. 521, no. 7553, pp. 460–466, 2015.
- [7] M. Barbic, J. J. Mock, A. P. Gray, and S. Schultz, "Electromagnetic micromotor for microfluidics applications," *Appl. Phys. Lett.*, vol. 79, no. 9, pp. 1399–1401, 2001.
- [8] L. K. E. A. Abdelmohsen, F. Peng, Y. Tu, and D. A. Wilson, "Micro- and nano-motors for biomedical applications," *J. Mater. Chem. B*, vol. 2, no. 17, pp. 2395–2408, 2014.
- [9] S. Sen, K. Harada, Z. Hewitt, E. Susilo, E. Kobayashi, and I. Sakuma, "Concept design of robotic modules for needlescopic surgery," *Minim. Invasive Ther. Allied Technol.*, vol. 26, no. 4, pp. 232–239, 2017.
- [10] W. Lee *et al.*, "A 10 Fr ultrasound catheter with integrated micromotor for 4D intracardiacechocardiography," *IEEE Trans. Ultrason. Ferroelectr. Fr equency Control*, vol. 58, no. 7, pp. 1478–1491, 2011.
- [11] S. Woods and T. Constandinou, "Engineering Micromechanical Systems for the Next Generation Wireless Capsule Endoscopy," *Biomed Res. Int.*, vol. 2015, pp. 1–14, 2015.
- [12] A. Chałupniak, E. Morales-Narváez, and A. Merkoçi, "Micro and nanomotors in diagnostics," *Adv. Drug Deliv. Rev.*, vol. 95, pp. 104–116, 2015.
- [13] J. Li, B. E. F. De Ávila, W. Gao, L. Zhang, and J. Wang, "Micro/nanorobots for Biomedicine: Delivery, surgery, sensing, and detoxification," *Sci. Robot.*, vol. 2, no. 4, 2017.
- [14] B. E. F. De Ávila *et al.*, "Micromotor-enabled active drug delivery for in vivo treatment of stomach infection," *Nat. Commun.*, vol. 8, no. 1, pp. 1–8, 2017.
- [15] Y. H. Lu, K. Mani, B. Panigrahi, S. Hajari, and C. Y. Chen, "A Shape Memory Alloy-Based Miniaturized Actuator for Catheter Interventions," *Cardiovasc. Eng. Technol.*, vol. 9, no. 3, pp. 405–413, 2018.
- [16] E. Meng and R. Sheybani, "Insight: Implantable medical devices," *Lab Chip*, vol. 14, no. 17, pp. 3233–3240, 2014.

- [17] A. H. Gosline *et al.*, “Metal MEMS Tools for Beating-heart Tissue Removal,” *2012 IEEE Int. Conf. Robot. Autom.*, pp. 1921–1926, 2012.
- [18] S. Russo, P. Mems, S. Kesner, R. Howe, R. Wood, and C. Walsh, “Toward Medical Devices With Integrated Mechanisms , Sensors , and Actuators Via,” vol. 11, no. March, 2017.
- [19] K. J. Rebello, “Applications of MEMS in Surgery,” vol. 92, no. 1, pp. 43–55, 2004.
- [20] A. Jovic *et al.*, “A MEMS Actuator System for an Integrated 3-D Optical Coherent Tomography Scanner,” vol. 27, no. 2, pp. 259–268, 2018.
- [21] S. Chang, E. Murdock, Y. Mao, C. Flueraru, and J. Disano, “Stationary-fiber rotary probe with unobstructed 360° view for optical coherence tomography,” *Opt. Lett.*, vol. 36, no. 22, p. 4392, 2011.
- [22] J.-M. Yang *et al.*, “A 2.5-mm diameter probe for photoacoustic and ultrasonic endoscopy.,” *Opt. Express*, vol. 20, no. 21, pp. 23944–53, 2012.
- [23] J. M. Yang *et al.*, “Simultaneous functional photoacoustic and ultrasonic endoscopy of internal organs in vivo,” *Nat. Med.*, vol. 18, no. 8, pp. 1297–1302, 2012.
- [24] J.-M. Yang, K. Maslov, H.-C. Yang, Q. Zhou, K. K. Shung, and L. V. Wang, “Photoacoustic endoscopy,” *Opt. Lett.*, vol. 34, no. 10, p. 1591, 2009.
- [25] S. Coda, P. Siersema, G. Stamp, and A. Thillainayagam, “Biophotonic endoscopy: a review of clinical research techniques for optical imaging and sensing of early gastrointestinal cancer,” *Endosc. Int. Open*, vol. 03, no. 05, pp. E380–E392, 2015.
- [26] T.-H. Tsai *et al.*, “Ultrahigh speed endoscopic optical coherence tomography using micromotor imaging catheter and VCSEL technology,” *Biomed. Opt. Express*, vol. 4, no. 7, p. 1119, 2013.
- [27] D. C. Adams, Y. Wang, L. P. Hariri, and M. J. Suter, “Advances in endoscopic optical coherence tomography catheter designs,” *IEEE J. Sel. Top. Quantum Electron.*, vol. 22, no. 3, 2016.
- [28] W. A. Welge and J. K. Barton, “In vivo endoscopic Doppler optical coherence tomography imaging of the colon,” *Lasers Surg. Med.*, vol. 49, no. 3, pp. 249–257, 2017.
- [29] F. Feroldi *et al.*, “In vivo multifunctional optical coherence tomography at the periphery of the lungs,” *Biomed. Opt. Express*, vol. 10, no. 6, p. 3070, 2019.
- [30] K. Li *et al.*, “Super-achromatic optical coherence tomography capsule for ultrahigh-resolution imaging of esophagus,” *J. Biophotonics*, vol. 12, no. 3, pp. 1–8, 2019.
- [31] K. Liang *et al.*, “Cycloid scanning for wide field optical coherence tomography endomicroscopy and angiography in vivo,” *Optica*, vol. 5, no. 1, p. 36, 2018.
- [32] E. Garai *et al.*, “A real-time clinical endoscopic system for intraluminal, multiplexed imaging of surface-enhanced Raman scattering nanoparticles,” *PLoS One*, vol. 10, no. 4, pp. 1–16, 2015.
- [33] A. H. Chau, J. T. Motz, J. A. Gardecki, S. Waxman, B. E. Bouma, and G. J. Tearney, “Fingerprint and high-wavenumber Raman spectroscopy in a human-swine coronary xenograft in vivo,” *J. Biomed. Opt.*, vol. 13, no. 4, p. 040501, 2008.
- [34] U. Oltmanns *et al.*, “Optical coherence tomography detects structural abnormalities of the

- nasal mucosa in patients with cystic fibrosis,” *J. Cyst. Fibros.*, vol. 15, no. 2, pp. 216–222, 2016.
- [35] A. M. D. Lee, A. Manjarres, C. MacAulay, and P. Lane, “Dual-beam manually-actuated catheters for wide-field distortion-corrected optical imaging,” vol. 1107810, no. July, p. 35, 2019.
- [36] A. M. D. Lee, G. Hohert, P. T. Angkiriwang, C. MacAulay, and P. Lane, “Dual-beam manually-actuated distortion-corrected imaging (DMDI) with micromotor catheters,” *Opt. Express*, vol. 25, no. 18, p. 22164, Sep. 2017.
- [37] M. Harlow, C. MacAulay, P. Lane, and A. M. D. Lee, “Dual-beam manually actuated distortion-corrected imaging (DMDI): two dimensional scanning with a single-axis galvanometer,” *Opt. Express*, vol. 26, no. 14, p. 18758, 2018.
- [38] K. Liang *et al.*, “Ultrahigh speed en face OCT capsule for endoscopic imaging,” *Biomed. Opt. Express*, vol. 6, no. 4, p. 1146, 2015.
- [39] J. Peng, L. Ma, X. Li, H. Tang, Y. Li, and S. Chen, “A Novel Synchronous Micro Motor for Intravascular Ultrasound Imaging,” *IEEE Trans. Biomed. Eng.*, vol. 66, no. 3, pp. 802–809, 2019.
- [40] H.-C. Lee *et al.*, “Circumferential optical coherence tomography angiography imaging of the swine esophagus using a micromotor balloon catheter,” *Biomed. Opt. Express*, vol. 7, no. 8, p. 2927, 2016.
- [41] T. Wang *et al.*, “Development of a high-speed synchronous micro motor and its application in intravascular imaging,” *Sensors Actuators, A Phys.*, vol. 218, pp. 60–68, 2014.
- [42] T. Mashimo, “Micro ultrasonic motor using a one cubic millimeter stator,” *Sensors Actuators, A Phys.*, vol. 213, pp. 102–107, 2014.
- [43] S. Cagatay, B. Koc, and K. Uchino, “A 1.6-mm, Metal Tube Ultrasonic Motor,” *IEEE Trans. Ultrason. Ferroelectr. Freq. Control*, vol. 50, no. 7, pp. 782–786, 2003.
- [44] T. Kanda, A. Makino, T. Ono, K. Suzumori, T. Morita, and M. K. Kurosawa, “A micro ultrasonic motor using a micro-machined cylindrical bulk PZT transducer,” *Sensors Actuators, A Phys.*, vol. 127, no. 1, pp. 131–138, 2006.
- [45] J. Li *et al.*, “High speed miniature motorized endoscopic probe for optical frequency domain imaging,” *Opt. Express*, vol. 20, no. 22, p. 24132, 2012.
- [46] P. H. Tran, D. S. Mukai, M. Brenner, and Z. Chen, “In vivo endoscopic optical coherence tomography by use of a rotational microelectromechanical system probe,” *Opt. Lett.*, vol. 29, no. 11, p. 1236, 2004.
- [47] P. R. Herz *et al.*, “Micromotor endoscope catheter for in vivo, ultrahigh-resolution optical coherence tomography,” *Opt. Lett.*, vol. 29, no. 19, p. 2261, 2004.
- [48] W. Piyawattanametha *et al.*, “In vivo near-infrared dual-axis confocal microendoscopy in the human lower gastrointestinal tract,” *J. Biomed. Opt.*, vol. 17, no. 2, p. 021102, 2012.
- [49] H. Inoue, S. E. Kudo, and A. Shiokawa, “Technology insight: Laser-scanning confocal microscopy and endocytoscopy for cellular observation of the gastrointestinal tract,” *Nat. Clin. Pract. Gastroenterol. Hepatol.*, vol. 2, no. 1, pp. 31–37, 2005.
- [50] J. Yserbyt, C. Dooms, M. Decramer, and G. M. Verleden, “Acute lung allograft rejection:

- Diagnostic role of probe-based confocal laser endomicroscopy of the respiratory tract,” *J. Hear. Lung Transplant.*, vol. 33, no. 5, pp. 492–498, 2014.
- [51] A. Lopez and J. C. Liao, “Emerging endoscopic imaging technologies for bladder cancer detection,” *Curr. Urol. Rep.*, vol. 15, no. 5, 2014.
- [52] N. Hanna *et al.*, “Two-dimensional and 3-dimensional optical coherence tomographic imaging of the airway, lung, and pleura,” *J. Thorac. Cardiovasc. Surg.*, vol. 129, no. 3, pp. 615–622, 2005.
- [53] J. J. Armstrong, M. S. Leigh, D. D. Sampson, J. H. Walsh, D. R. Hillman, and P. R. Eastwood, “Quantitative upper airway imaging with anatomic optical coherence tomography,” *Am. J. Respir. Crit. Care Med.*, vol. 173, no. 2, pp. 226–233, 2006.
- [54] H. O. Coxson *et al.*, “Airway wall thickness assessed using computed tomography and optical coherence tomography,” *Am. J. Respir. Crit. Care Med.*, vol. 177, no. 11, pp. 1201–1206, 2008.
- [55] I. K. Jang *et al.*, “Visualization of coronary atherosclerotic plaques in patients using optical coherence tomography: Comparison with intravascular ultrasound,” *J. Am. Coll. Cardiol.*, vol. 39, no. 4, pp. 604–609, 2002.
- [56] X. Li, J. Yin, C. Hu, Q. Zhou, K. K. Shung, and Z. Chen, “High-resolution coregistered intravascular imaging with integrated ultrasound and optical coherence tomography probe,” *Appl. Phys. Lett.*, vol. 97, no. 13, pp. 13–15, 2010.
- [57] X. D. Li *et al.*, “Optical coherence tomography: Advanced technology for the endoscopic imaging of Barrett’s esophagus,” *Endoscopy*, vol. 32, no. 12, pp. 921–930, 2000.
- [58] J. M. Poneros, S. Brand, B. E. Bouma, G. J. Tearney, C. C. Compton, and N. S. Nishioka, “Diagnosis of specialized intestinal metaplasia by optical coherence tomography,” *Gastroenterology*, vol. 120, no. 1, pp. 7–12, 2001.
- [59] C. S. Kim, P. Wilder-Smith, Y.-C. Ahn, L.-H. L. Liaw, Z. Chen, and Y. J. Kwon, “Enhanced detection of early-stage oral cancer in vivo by optical coherence tomography using multimodal delivery of gold nanoparticles,” *J. Biomed. Opt.*, vol. 14, no. 3, p. 034008, 2009.
- [60] M. J. Levy, “Endoscopic Ultrasound: An Introductory Manual and Atlas, 2nd edition,” *Gastroenterology*, vol. 142, no. 2, p. 410, 2011.
- [61] V. Kaul *et al.*, “Interventional EUS,” *Gastrointest. Endosc.*, vol. 72, no. 1, pp. 1–4, 2010.
- [62] L. W. Kwak, M. J. Campbell, D. K. Czerwinski, S. Hart, R. A. Miller, and R. Levy, “The New England Journal of Medicine Downloaded from nejm.org at ALBERT EINSTEIN COLLEGE OF MEDICINE on September 1, 2013. For personal use only. No other uses without permission. Copyright © 1992 Massachusetts Medical Society. All rights reserved.” *N. Engl. J. Med.*, vol. 327, no. 17, pp. 1209–1215, 1992.
- [63] F. G. Gress, R. H. Hawes, T. J. Savides, S. O. Ikenberry, and G. A. Lehman, “Endoscopic ultrasound-guided fine-needle aspiration biopsy using linear array and radial scanning endosonography,” *Gastrointest. Endosc.*, vol. 45, no. 3, pp. 243–250, 1997.
- [64] K. J. Chang, P. Nguyen, R. A. Erickson, T. E. Durbin, and K. D. Katz, “The clinical utility of endoscopic ultrasound-guided fine-needle aspiration in the diagnosis and staging of pancreatic carcinoma,” *Gastrointest. Endosc.*, vol. 45, no. 5, pp. 387–393, 1997.

- [65] K. I. Fu *et al.*, “Staging of early colorectal cancers: Magnifying colonoscopy versus endoscopic ultrasonography for estimation of depth of invasion,” *Dig. Dis. Sci.*, vol. 53, no. 7, pp. 1886–1892, 2008.
- [66] G. A. Silvestri *et al.*, “Endoscopic ultrasound with fine-needle aspiration in the diagnosis and staging of lung cancer,” *Ann. Thorac. Surg.*, vol. 61, no. 5, pp. 1441–1446, 1996.
- [67] N. Navani and S. M. Janes, “UKPMC Funders Group Mediastinal staging of NSCLC with endoscopic and endobronchial ultrasound,” vol. 6, no. 5, pp. 278–286, 2012.
- [68] M. Jermyn *et al.*, “A review of Raman spectroscopy advances with an emphasis on clinical translation challenges in oncology,” *Phys. Med. Biol.*, vol. 61, no. 23, pp. R370–R400, 2016.
- [69] I. R. Lewis, *Handbook of Raman Spectroscopy*. CRC Press, 2001.
- [70] M. S. Feld, A. S. Haka, M. Fitzmaurice, R. R. Dasari, J. Crowe, and K. E. Shafer-Peltier, “Diagnosing breast cancer by using Raman spectroscopy,” *Proc. Natl. Acad. Sci.*, vol. 102, no. 35, pp. 12371–12376, 2005.
- [71] F. Leblond *et al.*, “Intraoperative brain cancer detection with Raman spectroscopy in humans,” *Sci. Transl. Med.*, vol. 7, no. 274, pp. 274ra19–274ra19, 2015.
- [72] S. Wang, J. Zhao, H. Lui, Q. He, J. Bai, and H. Zeng, “Monte Carlo simulation of in vivo Raman spectral measurements of human skin with a multi-layered tissue optical model,” *J. Biophotonics*, vol. 7, no. 9, pp. 703–712, 2014.
- [73] H. C. McGregor, M. A. Short, S. Lam, T. Shaipanich, E. L. Beaudoin, and H. Zeng, “Development and in vivo test of a miniature Raman probe for early cancer detection in the peripheral lung,” *J. Biophotonics*, vol. 11, no. 11, pp. 1–5, 2018.
- [74] M. P. Coleman *et al.*, “Cancer survival in Australia, Canada, Denmark, Norway, Sweden, and the UK, 1995-2007 (the international cancer benchmarking partnership): An analysis of population-based cancer registry data,” *Lancet*, vol. 377, no. 9760, pp. 127–138, 2011.
- [75] R. L. Siegel, K. D. Miller, and A. Jemal, “Cancer statistics, 2019.,” *CA. Cancer J. Clin.*, vol. 69, no. 1, pp. 7–34, 2019.
- [76] R. Rami-Porta *et al.*, “The IASLC lung cancer staging project: Proposals for the revision of the T descriptors in the forthcoming (seventh) edition of the TNM classification for lung cancer,” *J. Thorac. Oncol.*, vol. 2, no. 7, pp. 593–602, 2007.
- [77] H. C. McGregor *et al.*, “Real-time endoscopic Raman spectroscopy for in vivo early lung cancer detection,” *J. Biophotonics*, vol. 10, no. 1, pp. 98–110, 2017.
- [78] E. Tsuboi, S. Ikeda, M. Tajima, Y. Shimosato, and S. Ishikawa, “Transbronchial biopsy smear for diagnosis of peripheral pulmonary carcinomas,” *Cancer*, vol. 20, no. 5, pp. 687–698, 1967.
- [79] L. Qiu *et al.*, “Multispectral scanning during endoscopy guides biopsy of dysplasia in Barrett’s esophagus,” *Nat. Med.*, vol. 16, no. 5, pp. 603–606, May 2010.
- [80] A. Schade, J. Krug, A. Szöllösi, M. El Tarahony, and T. Deneke, “Pulmonary vein isolation with a novel endoscopic ablation system using laser energy,” *Expert Rev. Cardiovasc. Ther.*, vol. 10, no. 8, pp. 995–1000, Aug. 2012.
- [81] A. S. T. Boots, L. E. Krijgsman, B. J. M. De Ruyter, S. G. E. Lampaert, and J. W. Spronck, “Tribology International Increasing the load capacity of planar ferro fluid bearings by the

- addition of ferromagnetic material,” *Tribology Int.*, vol. 129, no. August 2018, pp. 46–54, 2019.
- [82] H. Cheng, S. Xu, Y. Liu, S. Levi, and S. Wu, “Adaptive mechanical-wetting lens actuated by ferro fluids,” vol. 284, pp. 2118–2121, 2011.
- [83] Y. Mitamura and S. Takahashi, “A magnetic fluid seal for rotary blood pumps : effects of seal structure on long-term performance in liquid,” pp. 23–30, 2011.
- [84] Q. Liu, S. F. Alazemi, M. F. Daqaq, and G. Li, “Journal of Magnetism and Magnetic Materials A ferrofluid based energy harvester : Computational modeling , analysis , and experimental validation,” *J. Magn. Magn. Mater.*, vol. 449, pp. 105–118, 2018.
- [85] S. Sudo and Y. Takaki, “Magnetic Fluid Devices for Driving Micro Machines *,” vol. 48, no. 3, pp. 464–470, 2005.
- [86] R. Yang, H. Hou, Y. Wang, and L. Fu, “Sensors and Actuators B : Chemical Micro-magnetofluidics in microfluidic systems : A review,” vol. 224, pp. 1–15, 2016.
- [87] R. Olaru, C. Petrescu, and R. Hertanu, “A novel double-action actuator based on ferrofluid and permanent magnets,” vol. 23, no. 14, pp. 1623–1630, 2012.
- [88] H. Urreta *et al.*, “Seals Based on Magnetic Fluids for High Precision Spindles of Machine Tools To cite this version : HAL Id : hal-01970786,” 2019.
- [89] B. Assadsangabi, M. H. Tee, and K. Takahata, “Electromagnetic microactuator realized by ferrofluid-assisted levitation mechanism,” *J. Microelectromechanical Syst.*, vol. 23, no. 5, pp. 1112–1120, 2014.
- [90] B. Assadsangabi, M. H. Tee, S. Wu, and K. Takahata, “Ferrofluid-assisted micro rotary motor for minimally invasive endoscopy applications,” *Proc. IEEE Int. Conf. Micro Electro Mech. Syst.*, pp. 200–203, 2014.
- [91] B. Assadsangabi, M. H. Tee, S. Wu, and K. Takahata, “Catheter-Based Microrotary Motor Enabled by Ferrofluid for Microendoscope Applications,” *J. Microelectromechanical Syst.*, vol. 25, no. 3, pp. 542–548, 2016.
- [92] M. A. Short, S. Lam, A. McWilliams, J. Zhao, H. Lui, and H. Zeng, “Development and preliminary results of an endoscopic Raman probe for potential in vivo diagnosis of lung cancers,” *Opt. Lett.*, vol. 33, no. 7, p. 711, 2008.
- [93] D. Lin *et al.*, “Autofluorescence and white light imaging-guided endoscopic Raman and diffuse reflectance spectroscopy for in vivo nasopharyngeal cancer detection,” no. September 2017, pp. 1–9, 2018.
- [94] B. Assadsangabi and K. Takahata, “Micro rotary-linear actuator assisted by ferrofluid levitation for 3-dimensional endoscopic imaging,” in *2015 Transducers - 2015 18th International Conference on Solid-State Sensors, Actuators and Microsystems (TRANSDUCERS)*, 2015, pp. 391–394.
- [95] R. P. Madding, “Emissivity measurement and temperature correction accuracy considerations.,” pp. 393–401, 1999.
- [96] S. D. M. Herron, Daniel M. MD; Grabowy, Richard MS; Connolly, Raymond PhD; Schwaitzberg, “The Limits of Bloodwarming : Maximally Heating Blood with an Inline Microwave Bloodwarmer,” vol. 43, no. August 1997, pp. 219–228, 1997.

- [97] N. Huang *et al.*, “Full range characterization of the Raman spectra of organs in a murine model,” vol. 19, no. 23, pp. 179–193, 2011.
- [98] M. Matsuo, K. Iijima, T. Matsunaga, and Y. Haga, “Development of hood with hydraulically variable tip diameter for endoscopic submucosal dissection,” *Sensors Actuators, A Phys.*, vol. 232, pp. 267–275, 2015.
- [99] Z. Yang *et al.*, “Fabrication of microcoil with large tilt-angle on polymer tube for electromagnetically-driven scanner in single fiber endoscope,” *2015 IEEE SENSORS - Proc.*, pp. 0–3, 2015.
- [100] C. Fei *et al.*, “Ultrahigh frequency (100 MHz-300 MHz) ultrasonic transducers for optical resolution medical imaging,” *Sci. Rep.*, vol. 6, no. May, pp. 1–8, 2016.
- [101] M. P. C. Sanchez, Julio, *Embedded systems circuits and programming*. 2012.
- [102] Y.-K. L. Yen-Shin Lai, “Assessment of Pulse-Width Modulation Techniques for Brushless DC Motor Drives,” vol. 00, no. c, pp. 1629–1636, 2006.
- [103] P. S. Yarmolenko *et al.*, “Thresholds for thermal damage to normal tissues: An update,” *Int. J. Hyperth.*, vol. 27, no. 4, pp. 320–343, 2011.
- [104] M. W. Dewhirst, B. L. Viglianti, M. Lora-Michiels, M. Hanson, and P. J. Hoopes, “Basic principles of thermal dosimetry and thermal thresholds for tissue damage from hyperthermia,” *Int. J. Hyperth.*, vol. 19, no. 3, pp. 267–294, 2003.
- [105] R. L. McCreery, *Raman spectroscopy for chemical analysis*. 2005.
- [106] C. Hassler, T. Boretius, and T. Stieglitz, “Polymers for neural implants,” *J. Polym. Sci. Part B Polym. Phys.*, vol. 49, no. 1, pp. 18–33, 2011.
- [107] J. F. Kauffman, L. M. Batykefer, and D. D. Tuschel, “Raman detected differential scanning calorimetry of polymorphic transformations in acetaminophen,” *J. Pharm. Biomed. Anal.*, vol. 48, no. 5, pp. 1310–1315, 2008.
- [108] R. Szostak and S. Mazurek, “Quantitative determination of acetylsalicylic acid and acetaminophen in tablets by FT-Raman spectroscopy,” *Analyst*, vol. 127, no. 1, pp. 144–148, 2002.
- [109] G. Matute-Bello, C. W. Frevert, and T. R. Martin, “Animal models of acute lung injury,” *Am. J. Physiol. Cell. Mol. Physiol.*, vol. 295, no. 3, pp. L379–L399, 2008.
- [110] E. N. Meeusen, K. J. Snibson, S. J. Hirst, and R. J. Bischof, “Sheep as a model species for the study and treatment of human asthma and other respiratory diseases,” *Drug Discov. Today Dis. Model.*, vol. 6, no. 4, pp. 101–106, 2009.
- [111] N. Huang *et al.*, “Full range characterization of the Raman spectra of organs in a murine model,” *Opt. Express*, vol. 19, no. 23, p. 22892, 2011.
- [112] M. S. Bergholt *et al.*, “Simultaneous fingerprint and high-wavenumber fiber-optic Raman spectroscopy enhances real-time in vivo diagnosis of adenomatous polyps during colonoscopy,” *J. Biophotonics*, vol. 9, no. 4, pp. 333–342, 2016.
- [113] M. A. Short, I. T. Tai, D. Owen, and H. Zeng, “Using high frequency Raman spectra for colonic neoplasia detection,” *Opt. Express*, vol. 21, no. 4, p. 5025, 2013.
- [114] T. Tanaka, “Colorectal carcinogenesis: Review of human and experimental animal

- studies.,” *J. Carcinog.*, vol. 8, p. 5, 2009.
- [115] A. Nijssen *et al.*, “Discriminating basal cell carcinoma from perilesional skin using high wave-number Raman spectroscopy,” *J. Biomed. Opt.*, vol. 12, no. 3, p. 034004, 2007.
- [116] and H. Z. Zhao, Jianhua, Harvey Lui, David I. McLean, “Real-Time Raman Spectroscopy for Noninvasive in vivo Skin Analysis and Diagnosis,” *New Dev. Biomed. Eng.*, vol. IntechOpen, no. tourism, p. 13, 2010.
- [117] E. Larrañeta, R. E. M. Lutton, A. D. Woolfson, and R. F. Donnelly, “Microneedle arrays as transdermal and intradermal drug delivery systems: Materials science, manufacture and commercial development,” *Mater. Sci. Eng. R Reports*, vol. 104, pp. 1–32, 2016.
- [118] M. S. Packianather, C. H. Le, D. T. Pham, and H. Q. Le, “6th International Conference on the Development of Biomedical Engineering in Vietnam (BME6),” vol. 63, no. June, 2018.
- [119] S. Indermun *et al.*, “Current advances in the fabrication of microneedles for transdermal delivery,” *J. Control. Release*, vol. 185, no. 1, pp. 130–138, 2014.
- [120] H. R. Nejad, A. Sadeqi, G. Kiaee, and S. Sonkusale, “Low-cost and cleanroom-free fabrication of microneedles,” *Microsystems Nanoeng.*, vol. 4, no. August 2017, p. 17073, 2018.
- [121] S. J. Moon, S. S. Lee, H. S. Lee, and T. H. Kwon, “Fabrication of microneedle array using LIGA and hot embossing process,” *Microsyst. Technol.*, vol. 11, no. 4–5, pp. 311–318, 2005.
- [122] S. P. Sullivan, N. Murthy, and M. R. Prausnitz, “Minimally invasive protein delivery with rapidly dissolving polymer microneedles,” *Adv. Mater.*, vol. 20, no. 5, pp. 933–938, 2008.
- [123] R. Lutge *et al.*, “Integrated lithographic molding for microneedle-based devices,” *J. Microelectromechanical Syst.*, vol. 16, no. 4, pp. 872–884, 2007.
- [124] E. Rosenswei, “Magnetic Fluids Blums.pdf,” no. Papell 1965, 1987.
- [125] W.-B. Song, H. Kim, C. Son, and B. Ziaie, “Fabrication of Polymeric 3-D Micro-Structures Using Ferrofluid Molds,” *19th IEEE Int. Conf. Micro Electro Mech. Syst.*, no. January, pp. 334–337, 2006.
- [126] T. Jamin, C. Py, and E. Falcon, “Instability of the origami of a ferrofluid drop in a magnetic field,” *Phys. Rev. Lett.*, vol. 107, no. 20, 2011.

Appendix: High-aspect-ratio needle-shaped mold fabrication using Rosensweig instability in ferrofluids

In this section, a simple cleanroom-free fabrication technique to create high-aspect-ratio needle-like solid mold microstructures using magnetic self-assembly of ferrofluids under the Rosensweig instability of the fluids. The presented fabrication method provides precise and programmable control over the height, aspect ratio, and spatial arrangement of well-aligned and sharp microneedle structures of solidified ferrofluid formed in array on the substrate. These microneedle structures are demonstrated to have heights and aspect ratios of up to ~1.5 mm and ~5, respectively. The developed process offers an attractive path to the application for microneedle device production.

A.1 Introduction

Minimally invasive transdermal delivery of drugs into the body has been actively sought through the development of microneedle-based devices. The needle structures of these devices are microfabricated with various geometries with the heights ranging from 50 μm up to nearly 1 mm formed using different materials such as metals, silicon, and polymers [117]. Micromolding process is a common method for microneedle production [118]. The molding approach offers a potential advantage of low cost production due to its up-scaling ability [119]. The molds here are composed of high-aspect-ratio conical microstructures [120]. Various complicated and costly microfabrication processes have been proposed to create those 3D structures. These processes include LIGA based on x-ray lithography [121], photopatterning of SU-8 [122], and deep-reactive-

ion etching [123] to create high- aspect-ratio needle-like mold structures. However, the abovementioned processes not only require access to advanced microfabrication systems in cleanroom environments but also involve many fabrication steps, making the processes expensive and time-consuming.

The ferrofluid, a colloidal dispersion of magnetic nanoparticles in a carrier fluid, belongs to a category of smart fluids that can be manipulated using magnetic fields [124]. In the presence of a magnetic field gradient, this type of fluids flows toward the location with the highest magnetic flux density. Various modes of instabilities can occur in the fluids as a result of balance between the fluid's surface tension and the forces applied to the fluid including magnetic and gravitational forces. One such instability mode with air interface is known as the Rosensweig instability that occurs with a normal magnetic field [124]. In the presence of a vertical field, the ferrofluid surfaces concentrate the magnetic flux. The resulting magnetic force tends to drive the perturbation further, while surface tension and gravitational forces have a stabilizing influence. When the magnetic force exceeds the stabilizing forces, the instability occurs in the shape of cone-like spikes. The spike shape depends on the characteristics of the particular ferrofluid, including the fluid's viscosity and saturation magnetization, in addition to the applied field's intensity and orientation. Controlling these parameters provides a number of degrees of freedom in defining the geometric profile of the spikes (e.g., aspect ratio – the ratio of the base diameter of the spike to its height, and tip sharpness) as well as the location of the spikes on the substrate. The 3D molds with ferrofluid spikes generated via the Rosensweig instability was reported [125]. This method used a micromachined silicon membrane with perforations as the mechanical template to define both the size and location of the spikes, reporting the spike's aspect ratio and maximum height of ~ 1 and 0.2 mm, respectively. The approach that requires lithographically patterned templates inherently

poses not only cost related issues but also a limited controllability in needle's geometry being formed.

The current work investigates a simple cleanroom-free method to create an arbitrary array of ferrofluid's needle-like structures with significantly higher aspect ratios while offering an ability to program their individual heights and locations in the array targeting at microneedle applications. The developed process involves dispensing controlled volume of a ferrofluid onto the laser-patterned substrate placed over a permanent magnet that provides a perpendicular magnetic flux (Figure A.1). This method offers advantages in terms of both process simplicity and controllability over the shape and spatial arrangement of the generated spikes. The application for mold fabrication justifies the use of a serial (non-planar) process as is the case for the proposed approach. This ferrofluid-based process could contribute to enabling a low-cost production of microneedle molds with high degree of design freedom.

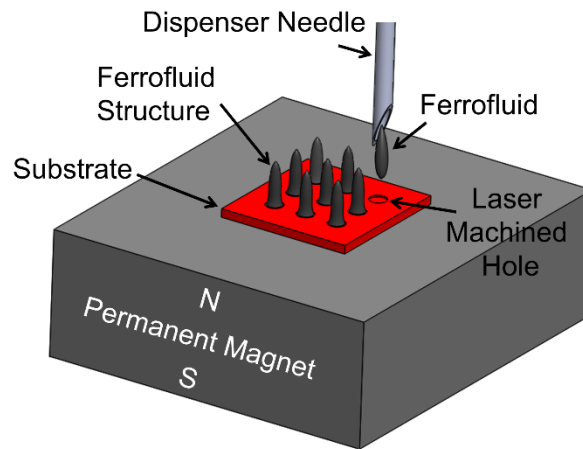


Figure A.1: Schematic view of the fabrication process for ferrofluid-based solid mold of microneedle array with individual needle's coordinate and geometric adjustability.

A.2 Fabrication

The developed process uses the normal-field (Rosensweig) instability in ferrofluids to create needle-shaped microstructures. As the intensity of the magnetic field applied perpendicular to a ferrofluid exceeds a certain threshold (which depends on the saturation magnetization and viscosity of the fluid), an instability of the ferrofluid is triggered to cause self-assembling of segregated spike structures of the fluid on the substrate. The formed ferrofluid spikes then move toward the location with the highest field intensity on the substrate (when there is a gradient of the intensity, a likely condition in a real set-up) due to magnetic attraction forces acting on the ferrofluid structures. In order to control/fix the position of the spikes while restraining their motions, an array of circular dimples (50- μm depth, 400- μm diameter) is pre-patterned on an acrylic substrate using a laser micromachining method (Step 1, Figure A.2). The substrate is placed on top of a NdFeB permanent magnet (K&J Magnetics, Inc, PA, USA; surface magnetization ~ 500 mT) with a size of $5 \times 5 \times 2.5$ cm³ at its center where the field vector is approximately perpendicular to the substrate plane. A selected ferrofluid is then injected into the dimples using a dispensing nozzle by positioning it above the location of each dimple. As the dispensing nozzle is lowered in a controlled manner using a micro-manipulator stage (SM 3.25, Marzhauser Wetzlar GmbH, Germany), the ferrofluid is pulled toward the substrate due to the magnetic attraction force exerted by the permanent magnet on the fluid, which is automatically deposited into the dimple. The deposited ferrofluid is then instantly self-assembled into a cone-shaped spike. The created spike will not move away from the dimple due to the surface force exerted by the dimple's side walls, which balances lateral magnetic forces acting on the ferrofluid spikes due to any field gradient present over the substrate. This process is repeated at all dimple locations to form an array of the ferrofluid spikes (Step 2, Figure A.2). The carrier fluid of the

liquid-phase spikes is then air-dried to solidify the ferrofluid, forming solid spikes that consist of tightly packed ferromagnetic nanoparticles (Step 3, Figure A.2). Finally, these solid spikes are conformally coated with Parylene C (8- μm thickness) to increase their mechanical stability (Step 4, Figure A.2).

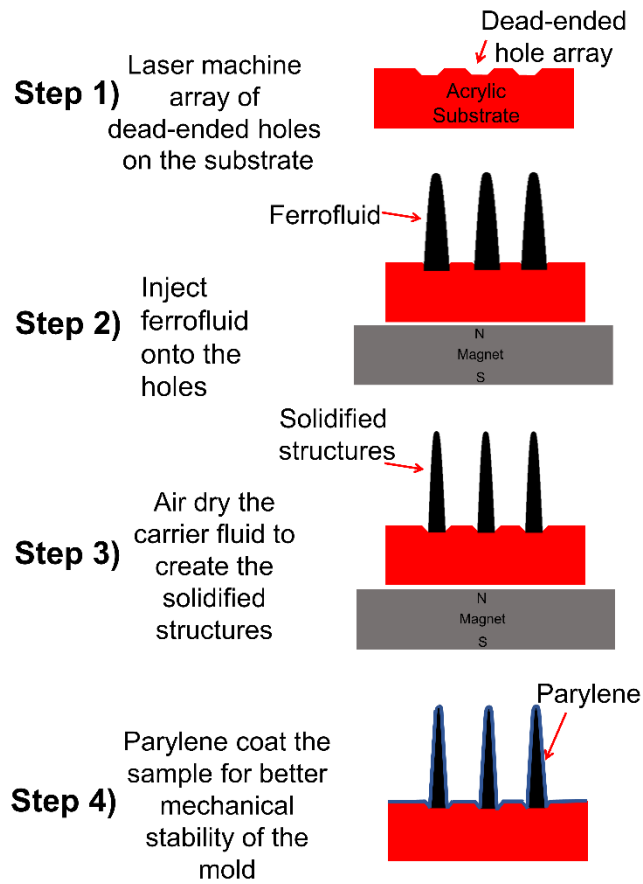


Figure A.2: Developed fabrication process.

A.3 Experimental results

To assess the performance of the proposed fabrication process in controlling geometric characteristics of the ferrofluid spikes, different sample arrays with varying shapes were fabricated. For this, two commercially available ferrofluids (EMG 901 and APG 513A, Ferrotec Co., NH, USA) with distinct properties in terms of the viscosity and the saturation magnetization were utilized to create the spike molds under controlled field intensities. Table 1 summarizes the physical properties of these ferrofluids used.

Table A.1: Physical properties of the two ferrofluids used.

Ferrofluid type	EMG 901	APG 513A
Saturation magnetization (mT)	66	40
Surface tension (mN/m)	25	33
Viscosity (mPa·s)	8	150
Density (g/m ³)	1.43	1.34
Particle diameter (nm)	10	10

As a preliminary test, each of these ferrofluids was characterized to evaluate the minimum magnetic field intensity that resulted in the normal-field instability with the fluid. A droplet of each ferrofluid was deposited onto a planar acrylic substrate (without the dimples), and then the substrate was lowered towards the permanent magnet from a distance (8 cm or more) at which the ferrofluid surface was still flat (i.e., at a stable state). While the substrate was made closer to the magnet, the magnetic flux density was measured at every 10-mm location using a Gauss meter

(Parker 5170S, F. W. Bell Inc., USA) attached on the surface of the substrate. The measured results (the average of three measurements) for each ferrofluid were plotted in Figure A.3. As can be seen, the normal-field instability in EMG 901 appeared to occur at a magnetic flux density of ~ 13 mT, which was found to be $>6\times$ lower than that of APG 513A. Another important observation in this experiment was that the aspect ratio of EMG 901 spikes was significantly higher as compared to the APG 513A case (~ 5 vs. <1). These results may be explained through the magnetic Bond number, a dimensionless parameter that indicates the ratio between magnetic and capillary energies counteracting from each other over the fluid [126]. The magnetic Bond number depends on both the applied magnetic flux density and the physical properties of a ferrofluid. The aspect ratio of a ferrofluid spike increases with the magnetic Bond number, which increases with the saturation magnetization but decreases with the surface tension. If an identical magnetic field is used for both the ferrofluids, the magnetic force generated in EMG 901 will be larger than that of APG 513A because the former has a larger saturation magnetization (which is an indicator of a larger magnetic particle concentration) as shown in Table

1. APG 513A can exhibit a larger resisting capillary forces due to its larger surface tension value compared with EMG 901 as also seen in Table 1. Thus, the magnetic Bond number of the EMG 901 should be larger than that of APG 513A at a given magnetic flux density, leading to the observed results.

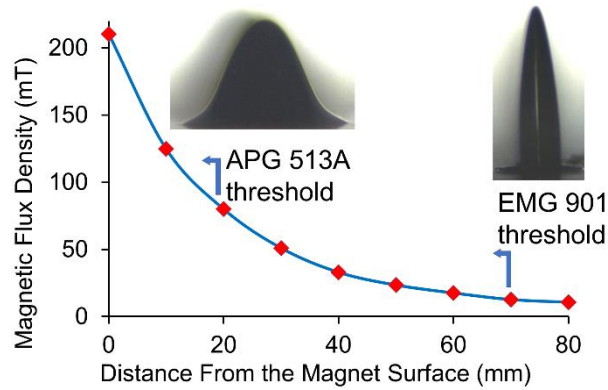


Figure A.3: Measured magnetic thresholds (as a function of magnet distance) for Rosensweig instability of the two ferrofluids used.

Another test was conducted to demonstrate the controllability for the heights of individual ferrofluid spikes. In order to accomplish this, the ferrofluid volume injected into a dimple of the substrate should be varied in a controlled manner. This test used EMG 901 ferrofluid given its higher aspect-ratio feature as verified in the previous test. A stainless-steel needle (gauge# 15, 1.37-mm inner diameter) was used as the ferrofluid dispenser nozzle. The tip of dispenser nozzle was dipped into a ferrofluid in its reservoir using the stage, with a controlled dipping/wetting depth so that when the nozzle was pulled up, a controlled amount of the ferrofluid was sustained in the nozzle tip, which was then transferred to each dimple on the substrate. Figure A.4 shows two samples fabricated through this method. In Figure A.4a, an array of ferrofluid spikes with a uniform height (of 1.4 mm) was created by keeping the dip depth constant, whereas for the array shown in Figure A.4b, the same process was performed by varying the dip depths (decreased from left to right of the displayed array in a consistent manner), resulting in corresponding changes in their structural heights. This experiment also indicated that at a given field intensity, there was a maximum threshold volume/height of the ferrofluid that produced a single spike, beyond which the deposited fluid split into two (or more) smaller spikes.

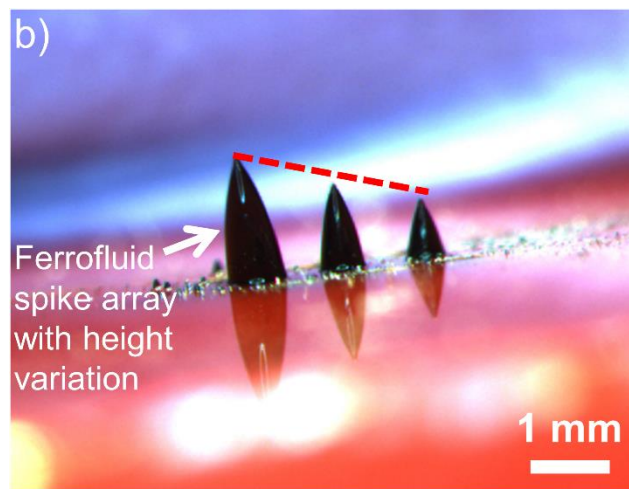
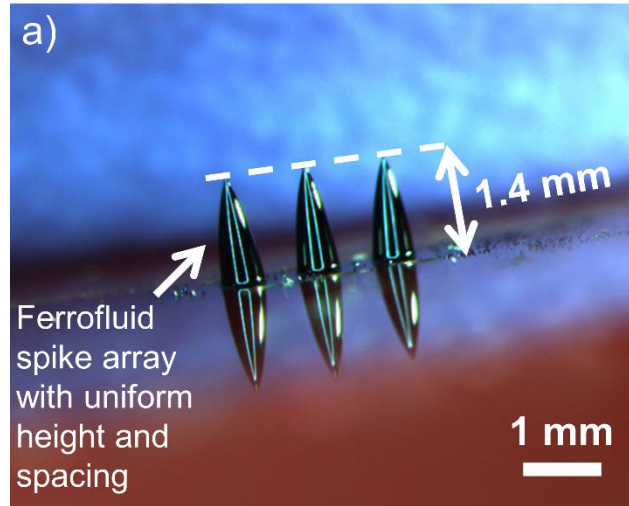


Figure A.4: Location and height control of ferrofluid spikes (before drying) on the substrate, achieved using EMG 901 ferrofluid with higher saturation magnetization (66 mT) and lower viscosity (8 mPa·s): a) 3×1 array with a uniform height; b) 3×1 array with varying heights.

In order to further demonstrate the developed process, 3×3 arrays of self-assembled spikes were fabricated by dispensing a uniform amount for each ferrofluids on the acrylic substrates with the corresponding arrays of the laser-patterned dimples under an identical magnetic field, after

which the array (together with the substrate) was coated with Parylene C as in the developed process (Figure A.2). Figure A.5 shows a sample array created using APG 513A. As can be seen, the formed structures in the array exhibited a relatively low aspect ratio, slightly less than 1, with a somewhat large radius ($\sim 65 \mu\text{m}$) at the tip of each structure. In contrast, the same array fabricated using EMG 901 (Figure A.6) shows needle-like tall spikes with a $>5\times$ greater aspect ratio and a $\sim 3\times$ smaller tip radius compared with the APG 513A case. The structural tendency including their aspect-ratio difference observed in these fabricated arrays of the two ferrofluids appear to be consistent with that from the earlier results (Figure A.3). This is an expected outcome, because under an identical magnetic field intensity, these two ferrofluids would have the same relationship in their magnetic Bond numbers and thus should exhibit a similar aspect-ratio relationship in their spikes created.

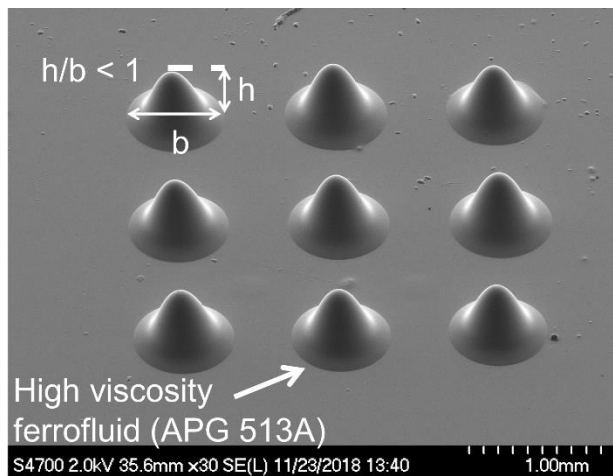


Figure A.5: Scanning electron microscope (SEM) image of the Parylene-coated mold fabricated using APG 513A ferrofluid with lower saturation magnetization (40 mT) and higher viscosity (150 mPa·s) showing relatively low aspect ratio and large tip radius.

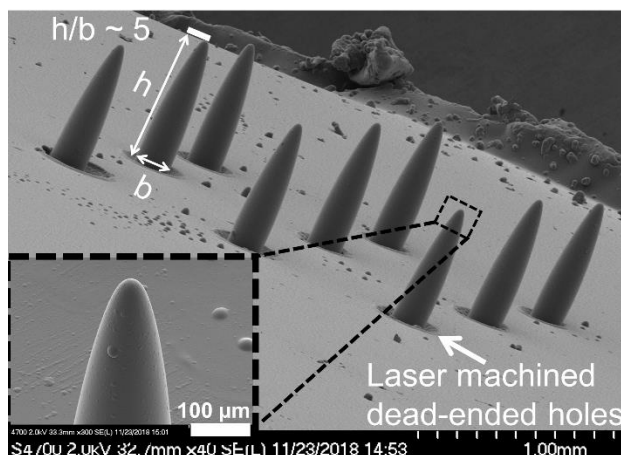


Figure A.6: SEM image of the Parylene-coated mold fabricated using EMG 901 ferrofluid showing high-aspect-ratio structures with sharper tips.

A.4 Conclusion

This work has developed a cleanroom-free fabrication technique to create high-aspect-ratio microneedle mold structures through magnetic self-assembly of ferrofluids under the Rosensweig instability of the fluids. The aspect ratio, height, tip sharpness, and spatial arrangement of individual needle structures were demonstrated to be controllable in fabrication of their arrays using two types of ferrofluids. The lateral locations of the ferrofluid spikes and their heights in an array were precisely determined by programming the coordinates and amounts of ferrofluid being deposited onto the dimple structures that were prepatterned on the substrate. The process showed its ability to form microneedle mold structures with aspect ratios up to 5 that were freely variable in them. The demonstrated micromold fabrication process could be a promising approach to the manufacturing application for microneedle devices through further process optimization, due to inherent low-cost and flexibility features that the approach offers.